

UNIVERSITÉ DE SHERBROOKE

Faculté des Lettres et de Sciences Humaines

Département de Géomatique Appliquée

Understanding Arctic aerosols : multi-station climatology of extensive- and intensive-parameter optical retrievals & evaluation of an advanced aerosol transport model versus the multi-station climatology

Yasmin AboEl-Fetouh

Thesis submitted in partial fulfillment of the requirements for the degree of Doctor of Philosophy (Ph.D.) in physics of remote sensing

April 2022

Sherbrooke, Québec, Canada

JURY

Supervisor: Prof. Norman T. O'Neill

Internal Member: Prof. Alain Royer

Internal Member: Adj. Prof. Martin Aubé

External Member: Prof. Victoria E. Cachorro

Abstract

Atmospheric aerosols play a crucial radiative forcing role in climate systems. They influence the radiative balance by either the direct effect of absorbing or scattering of radiation or the indirect affect associated with the impact of their physical and optical properties on cloud droplet or ice nucleation properties. Parameterizing their direct and indirect radiative forcing contributions represents a major challenge to climate modellers. Uncertainties arise in the representation of aerosol microphysics and optical properties: to strengthen the confidence in climate model simulations, aerosol opto-physical property interpretations of robust (climatological scale) measurements in parallel with the validation of aerosol-model simulations are essential.

It is accordingly important to understand the physical, chemical, and optical properties of aerosols as well as the processes that govern their formation and transportation mechanisms. Aerosol properties are characterized by their size, shape, chemical nature and concentration. From an optical (UV to near-IR) perspective, the fundamental form of the particle size distribution (PSD) that significantly affects optical measurements is largely represented by two modal components: a fine mode (FM) sub-micrometer (radius) component and a coarse mode (CM) super-micrometer component. Their optical impact is dependent on the PSD, the refractive index (which defines the scattering and absorption impact as a function of their size) and radiation wavelength.

In this research project, we focused on Arctic aerosols: this is especially relevant from a climate change perspective given that Arctic temperature changes are roughly twice those of the global average. Our objectives were broken into two phases (corresponding to two peer-reviewed papers). The first phase was an investigation of the seasonal variations of various microphysical and optical aerosol properties over the Arctic using ground-based retrievals of sunphotometer/sky radiometer measurements provided by AERONET/AEROCAN (AEROSol Robotic NETwork/Canadian AEROCAN subnetwork). The second was an investigation into the accuracy of spatio-temporal aerosol model simulations and their success in capturing the seasonal trends of Arctic aerosols. Given the daylight limitations of sunphotometry/sky radiometry, we were constrained to the spring to early fall seasons.

In Paper 1, we performed a climatological-scale (seasonal) multi-year study of key extensive (quantity dependent) and intensive (quantity independent) aerosol retrievals from six AERONET Arctic stations. An important original contribution of this paper was an analysis that went beyond

the traditional parameters of aerosol optical depth (AOD) and classical Angstrom exponent (spectral slope of the AOD in logarithmic space). The analysis parameters included the PSD, the radius of cardinal features of the PSD such as the peaks of the FM and CM components, the FM and CM AOD, the FM and CM effective radii, and the fine mode fraction (FMF). The originality of the monthly-binned results included robust FM and CM seasonal tendencies from spring to summer (notably a small but robust increase in the radius of the FM peak that was attributed to the influence of large particle summertime smoke and the demonstration of a pan-Arctic (even pan Canadian) springtime, small CM-particle-size ($\sim 1.3 \mu\text{m}$) peak that was attributed to springtime Asian dust.

In Paper 2, we compared the simulations of GCT (GEOS-Chem - TOMAS) to the seasonal results of Paper 1. The TOMAS (Two Moment Aerosol Sectional) aerosol microphysical model provides PSD number and mass concentrations spread across an Arctic domain that included the 6 AERONET stations. We investigated the same seasonal variations as those presented in Paper 1 by (offline) conversion TOMAS outputs to parameters that were analogous to the AERONET products. Specific Paper 1 tendencies such as the small CM-particle-size peak due to Asian dust and the robust spring to summer decrease of the CM AOD were successfully simulated. At the same time, GCT did not capture the spring to summer increase in radius of the FM peak and provided a FM effective radius that was significantly smaller than the values of Paper 1. This, we argued, was likely attributable to a GCT shortcoming in the modelling of small particle (coagulative) growth of smoke particles (problem associated with the coarse GCT lat/long spatial resolution of $4^\circ \times 5^\circ$).

Key Words: Arctic aerosols, Arctic-aerosol climatology, extensive and intensive microphysical and optical properties, coarse mode (CM) and fine mode (FM) aerosols, AERONET, GEOS-Chem TOMAS

Résumé

Les aérosols atmosphériques jouent un rôle crucial dans le forçage radiatif des systèmes climatiques. Ils influencent le bilan radiatif soit par l'effet direct d'absorption ou de diffusion du rayonnement, soit par l'effet indirect associé à l'impact de leurs propriétés physiques et optiques sur les propriétés de nucléation des gouttelettes nuageuses ou de la glace. Le paramétrage de leurs contributions directes et indirectes au forçage radiatif représente un défi majeur pour les modélisateurs climatiques. Des incertitudes surgissent dans la représentation des propriétés microphysiques et optiques des aérosols : pour renforcer la certitude dans les simulations des modèles climatiques, les interprétations des

propriétés opto-physiques des aérosols de mesures robustes (à l'échelle climatologique) parallèlement à la validation des simulations des modèles d'aérosols sont essentielles.

Il est donc important de comprendre les propriétés physiques, chimiques et optiques des aérosols ainsi que les processus qui régissent leurs mécanismes de formation et de transport. Les propriétés des aérosols sont caractérisées par leur taille, leur forme, leur nature chimique et leur concentration. D'un point de vue optique (UV à proche IR), ils sont effectivement bimodaux : leur distribution granulométrique (PSD) est largement représentée par deux composantes modales : une composante submicrométrique (rayon) de mode fin (FM) et une composante grossière (CM) qui est un composant super-micrométrique. Leur impact optique dépend de la PSD, de l'indice de réfraction (qui définit l'impact de diffusion et d'absorption en fonction de leur taille) et de la longueur d'onde du rayonnement.

Dans ce projet de recherche, nous nous sommes concentrés sur les aérosols arctiques : cela est particulièrement pertinent du point de vue du changement climatique étant donné que les changements de la température dans l'Arctique sont environ le double de la moyenne mondiale. Nos objectifs ont été divisés sur deux phases (correspondant à deux articles évalués par des pairs). La première phase consistait en une analyse des variations saisonnières de diverses propriétés microphysiques et optiques des aérosols au-dessus de l'Arctique à l'aide d'extractions au sol de mesures de photomètres solaires/radiomètres célestes fournies par AERONET/AEROCAN (AEROSol Robotic NETwork/sous-réseau canadien AEROCAN). La seconde était analyse sur l'exactitude des simulations de modèles d'aérosols spatio-temporels et leur succès dans la capture des tendances saisonnières des aérosols arctiques. Étant donné les limites de la lumière du jour de la photométrie solaire/radiométrie du ciel, nous étions limités aux saisons du printemps et au début de l'automne.

Dans le premier l'article, nous avons effectué une étude pluriannuelle à l'échelle climatologique (saisonnière) des principales caractéristiques d'aérosols extensives (dépendantes de la quantité) et intensives (indépendantes de la quantité) de six stations d'AERONET dans de l'Arctique. Une contribution originale importante de cet article était une analyse qui allait au-delà des paramètres traditionnels de la profondeur optique des aérosols (AOD) et de l'exposant d'Angstrom classique (pente spectrale de l'AOD). Les paramètres d'analyse comprenaient la PSD, le rayon des caractéristiques cardinales de la PSD telles que les pics des composantes FM et CM, les AOD FM et CM, les rayons effectifs FM et CM et la fraction de mode fin (FMF). L'originalité des résultats

mensuels incluait des tendances saisonnières FM et CM robustes du printemps à l'été (notamment une augmentation faible mais robuste du rayon du pic FM qui a été attribuée à l'influence de la fumée estivale à grosses particules et à la démonstration d'un pan -Printemps arctique (même pan canadien), petit pic de taille de particules CM (~ 1,3 μ m) attribué à la poussière asiatique printanière.

Dans le deuxième l'article, nous avons comparé les simulations de GCT (GEOS-Chem - TOMAS) aux résultats saisonniers du premier article 1. Le modèle microphysique d'aérosol TOMAS (Two Moment Aerosol Sectional) fournit les densités numériques et les concentrations en masse réparties dans un domaine Arctique qui comprenait les six stations d'AERONET. Nous avons étudié les mêmes variations saisonnières que celles présentées dans le premier article par conversion (hors ligne) des sorties TOMAS en paramètres analogues aux produits AERONET. Les tendances spécifiques du premier article 1 telles que le petit pic de taille de particule CM dû à la poussière asiatique et la forte diminution du printemps à l'été de l'AOD CM ont été simulées avec succès. Au même temps, GCT n'a pas capturé l'augmentation du printemps à l'été du rayon du pic FM et a fourni un rayon effectif FM qui était significativement plus petit que les valeurs de la première recherche. Ceci était probablement attribuable à une lacune de GCT dans la modélisation de la croissance de petites particules (coagulantes) de particules de fumée (problème associé à la résolution spatiale lat/long GCT grossière de $4^\circ \times 5^\circ$).

Mots clés : Aérosols arctiques, climatologie des aérosols arctiques, propriétés microphysiques et optiques extensives et intensives, aérosols en mode grossier (CM) et en mode fin (FM), AERONET, GEOS-Chem TOMAS

Acknowledgments

I will forever be grateful to my PhD supervisor and mentor Dr. Norman T. O'Neill for his endless support on both a professional and personal level. I am extremely thankful for his consistent guidance, invaluable advice, contribution, and effort at every stage of this project. I truly appreciate his generosity, enthusiasm towards my ideas and achievements, and his motivation. Norm's door was always open for any discussions, and I really cannot thank him enough on the support he provided. His patience and dedication are an example of an excellent mentor and scientist. He is a wonderful role model and I count myself lucky to have had such a dedicated supervisor.

The completion of this research would not have been possible without all our collaborators that have contributed to the success of the work. I especially extend my appreciation to Dr. Jeffrey R. Pierce and Dr. Jack Kodros, at Colorado State University, for their collaboration and providing us with the GEOS-Chem TOMAS simulations. Their comments, insights, and many discussions were valuable to this research. Special thanks to Dr. Jack Kodros for his patience with my never-ending questions and for his consistent support on the coding work. This work would have been incomplete without them. Also, many thanks to Hui Zhong Lu at UdeS for his technical support in dealing with Calcul Quebec / Compute Canada's supercomputer clusters, in addition to his expertise in everything to do with Python and high-performance computing!

I would also like to thank the Faculté des Lettres et de Sciences Humaines for their wonderful administrative support. I especially thank them for providing me with the necessary resources in my final year and standing by me during hard times.

My PhD journey wouldn't have existed without the insistence and motivation of Dr. Mohamed El-Raey and the support of Dr. Mohamed Shokr. I also would like to thank Dr. Alaa Ibrahim for his constant motivation. I am deeply grateful for them because this step has completely changed my life!

I will cherish many memories I made with all my colleagues and the new friends I made, especially those who passed by the PhD room from 2015 to 2020: my comrades whom I have shared many discussions and laughs with! I especially thank my dear friends and supporters Hajar Saikouk for her revision of my French abstract and Shridevi Sandiramourty of revising the Sommaire en Français.

Life would have been intolerable without my supportive family and friends; they really kept me going all the way to the finish line. Special thanks to my mother and my dear sister, Timona, for keeping me strong, for having my back, and for their endless advice! Earning a PhD was my late father's dream as he was a man who highly valued science and scientists. If he was here, he would have been beaming with pride and his eyes would have been filled with tears of joy. I am glad I accomplished this for him.

*To my mother, Afaf Hindawi
Who taught me courage and made me the person I am today.*

Table of Contents

Abstract	i
Résumé	ii
<i>Acknowledgments</i>	v
Sommaire en Français	viii
1.Introduction	1
1.1 Arctic aerosols.	2
1.2 Investigating Arctic Aerosols.....	3
1.3 Objectives.....	4
1.4 Hypotheses	5
1.5 Articles and article originality.....	5
1.51 Article 1: Climatological-scale study of aerosol properties	5
1.52 Article 2: Evaluation of GCT simulations with AERONET retrievals	6
2.Paper 1 : Climatological-Scale Analysis of Intensive and semi-intensive aerosol parameters derived from AERONET retrievals over the Arctic.....	8
3.Paper 2: Seasonal comparisons of GEOS-Chem TOMAS simulations with AERONET-inversion products over the Arctic	44
4.Conclusions	71
4.1 Challenges and limitations	71
4.2 Recommendations and future work	72
Appendix A: Equations	73
Basic Aerosol Physics.....	73
GCT equations – Technical Memo	79
Appendix B: GCT AOD Code	88
Appendix C: Flowchart of thesis project.....	97
References	98

Sommaire en Français

Selon Hinds (1999), les aérosols peuvent être définis comme « une suspension de particules solides ou liquides dans un gaz ». Ils peuvent être d'origine naturelle comme le sel marin et les poussières du désert ou d'origine anthropique comme la pollution particulaire des émissions industrielles. La plupart de ces particules sont connues pour avoir un effet de refroidissement (direct) (par rapport au réchauffement causé par les gaz à effet de serre) car elles rétrodiffusent principalement le rayonnement solaire entrant (Boucher et al., 2013). Les aérosols fortement absorbants tels que les aérosols de carbone noir (“black carbon” aerosols) peuvent avoir un effet de réchauffement moindre mais significatif (voir la figure emblématique « estimations du forçage radiatif » de Boucher et al., 2013). La deuxième manière (indirecte) dont les aérosols influencent le climat sont les interactions aérosol-nuage ; les aérosols agissant comme des noyaux de condensation des gouttelettes de nuages ou de nuages de glace ont un impact sur les propriétés microphysiques et optiques des nuages (Boucher et al., 2013).

La taille des aérosols varie en fonction de leur composition et de leur mode de génération. Leurs propriétés microphysiques et optiques associées peuvent être divisées en deux catégories. Les propriétés « extensives » dépendent de la quantité : dans la recherche sur la télédétection des aérosols, le paramètre de propriété extensive le plus largement utilisé est la profondeur optique des aérosols (AOD). L'AOD est avant tout un indicateur de la densité numérique d'aérosols dans une colonne atmosphérique : leur impact de concentration en nombre se manifeste par leurs propriétés intrinsèques d'absorption et de diffusion. La deuxième catégorie concerne les « propriétés intensives » (par particule ou non dépendantes de la quantité) telles que la taille, la forme et la composition : ces types de paramètres variants lentement fournissent des indications sur l'origine des aérosols. Ils peuvent également être sensibles aux paramètres météorologiques, tels que l'influence croissante de la taille de l'humidité relative (croissance hygrométrique). Le rayon effectif ainsi que d'autres marqueurs de rayon des caractéristiques clés de la distribution granulométrique volumique (PSD) sont d'importants exemples de paramètres intensifs dans notre travail de recherche. Enfin, une sous-catégorie de propriétés peut être qualifiée de « semi-intensive » ou de « semi-extensive » : celles-ci, comme le suggère cet étiquetage, sont une combinaison de paramètres extensifs et intensifs. Un exemple important de paramètre semi-intensif est la fraction de mode fin (FMF) qui est le rapport de l'AOD en mode fin à l'AOD totale à une longueur d'onde de référence. Un deuxième exemple classique de paramètre semi-intensif est l'exposant générique d'Angstrom (souvent appelé α ou \AA). Cet exposant

(dérivé de l'approximation du premier ordre selon laquelle l'AOD varie comme $\lambda^{-\alpha}$) est un indicateur robuste mais primitif de la taille des particules d'aérosol (O'Neill et al., 2001).

Un concept important dans notre recherche (au cœur de la stratégie d'analyse de l'article 1 et de l'article 2) est la caractéristique de bimodalité du PSD : pour la plupart des applications optiques, le PSD peut être divisé en une composante submicronique (mode fin ou FM) et une composante supermicronique (mode grossier ou CM) (voir l'article 1 pour plus de détails). L'utilisation de ce concept robuste permet de mieux comprendre l'analyse des tendances des propriétés des aérosols, leurs sources possibles et les processus dynamiques qui contrôlent leur évolution. Pour plus de détails sur les équations des propriétés microphysiques et optiques utilisées dans ce travail, veuillez vous référer à l'article 1 et l'annexe A.

L'Arctique est une région importante et sensible qui subit les impacts les plus graves du changement climatique. Le dernier rapport du Programme de surveillance et d'évaluation de l'Arctique (AMAP) indique que la température moyenne de l'Arctique a augmenté trois fois plus rapidement que la moyenne mondiale au cours des 49 dernières années (AMAP, 2021). Le 6e rapport d'évaluation du IPCC indique que la température de l'Arctique continuera d'augmenter à un rythme plus de deux fois supérieur à celui du réchauffement climatique (IPCC, 2021). Ce phénomène surnommé « l'amplification de l'Arctique » a déclenché un changement rapide dans l'environnement de l'Arctique qui, à son tour, contribue aux préoccupations locales et mondiales. Les réductions de l'étendue de la glace de mer et de la couverture neigeuse ont, par exemple, contribué à l'élévation du niveau de la mer à l'échelle mondiale (Slater et al., 2020) ainsi qu'à l'augmentation de la teneur en poussière locale (voir par exemple Udisti et al., 2020 sur l'Arctique général).

Divers types d'aérosols provenant de sources locales ou éloignées peuvent être trouvés dans l'atmosphère arctique tout au long de l'année. À la fin de l'hiver et au printemps, des aérosols provenant des latitudes moyennes, des sources anthropiques sont transportés dans l'Arctique. Cela se traduit par la « brume arctique » récurrente, dont le principal composant est les sulfates FM, en plus des aérosols de carbone noir ('black carbon' ou BC) (Abbatt et al., 2019). Alors que la composante sulfate est en grande partie une contribution au refroidissement due à la rétrodiffusion solaire, la composante BC joue un rôle unique dans le réchauffement de l'Arctique par sa capacité d'absorption dans l'atmosphère et par dépôt direct sur la neige et la glace : ce dernier effet provoque une diminution de la réflectance de la surface (Abbatt et al., 2019), et favorise ainsi la fusion. La poussière CM a un effet de réduction de la réflectance similaire : la poussière d'origine asiatique et locale (voir, par

exemple, Groot Zwaaftink et al., 2016) a également un impact de dépôt pendant le printemps arctique (pour plus d'informations sur la poussière dans l'Arctique, voir Bullard et al. (2016)). Le sel de mer CM contribue également à la brume en raison de la présence supplémentaire de vents plus forts en hiver et au printemps (voir par exemple Abbatt et al., 2019, et Huang & Jaeglé, 2017). À la fin du printemps et au début de l'été, la brume arctique commence à diminuer tout en laissant place à une augmentation des événements de fumée (CB naturels et carbone organique) dont les origines sont attribuables à la combustion de la biomasse des feux de forêt boréale et/ou des feux agricoles de différentes régions continentales (Canada, Alaska, Europe et Asie de l'Est : voir par exemple Eck et al., 2009). Les éruptions volcaniques peuvent également contribuer aux aérosols estivaux (voir par exemple Breider et al., 2014).

Un concept critique dans la dynamique arctique saisonnière est le dôme polaire (surfaces concentriques en forme de dôme qui définissent les voies privilégiées pour le transport des particules dans l'Arctique) et son influence fondamentale sur la brume arctique (Law & Stohl, 2007). À mesure que l'été émerge, le dôme polaire rétracté et les conditions météorologiques variées entraînent des temps de séjour plus longs des aérosols naturels qui sont confinés à des altitudes plus basses (Abbatt et al., 2019). Au même moment, la pollution due au transport à longue distance existe à des altitudes plus élevées (Law & Stohl, 2007, Schmale et al., 2021). Des détails sur les voies de transport typiques des aérosols dans l'Arctique se trouvent au chapitre 4 d'Udisti et al. (2020). De plus amples détails sur les aérosols arctiques peuvent être trouvés dans Abbatt et al. (2019).

La télédétection au sol et par satellite sont des outils essentiels pour surveiller et étudier les paramètres optiques et microphysiques des aérosols. Nous avons utilisé les inversions d'AERONET disponibles à diverses stations de l'Arctique dans nos recherches. AERONET (Aerosol Robotic Network) est un réseau de photomètres solaires/radiomètres du ciel qui permet de récupérer les propriétés microphysiques et optiques des aérosols. Les inversions d'AERONET ont été essentielles afin de réaliser une analyse climatologique des aérosols arctiques (malgré les défis évidents de fournir des mesures à long terme de haute qualité dans l'Arctique).

Les algorithmes chimiques et microphysiques intégrés aux modèles de dynamique météorologique pour réaliser des simulations spatio-temporelles de l'évolution des gaz et des particules sont un outil essentiel pour interpoler, extrapoler et, surtout, mieux comprendre la physique de ce qui est généralement des mesures ponctuelles et irrégulières d'aérosols (en particulier dans l'Arctique). Les modèles de transport chimique (CTM) sont des modèles spatio-temporels qui simulent la chimie

atmosphérique ainsi que le transport mécanique et peuvent représenter l'évolution de différentes espèces chimiques. Ils sont utilisés, avec des modules microphysiques d'aérosols spécifiques, pour mieux comprendre les processus qui contrôlent les distributions spatiales et temporelles des aérosols ainsi que leurs transformations chimiques et leur élimination (voir, par exemple, Chin et al., 2019). Des inversions d'AERONET ont été largement utilisées dans les études d'évaluation de modèles. Ces études ont cependant été largement limitées aux paramètres génériques du premier ordre de l'AOD à une seule longueur d'onde et à l'exposant d'Angstrom. L'une des innovations de notre recherche est de comparer les simulations du modèle avec les paramètres essentiellement du second ordre associé à la division FM et CM de la PSD (où les composantes FM et CM sont essentiellement des paramètres intensifs tels que le rayon effectif FM ou CM ou des paramètres extensifs tels que les AODs FM CM). En général, la pratique consistant à utiliser des mesures de télédétection (colonnes) pour l'évaluation de modèles est une première étape importante pour augmenter la précision des simulations de modèles en tout point de l'atmosphère (voir également la discussion dans l'introduction de l'article 2).

Le modèle que nous avons utilisé pour les comparaisons avec les produits FM et CM d'AERONET était GCT (GEOS-Chem TOMAS). GEOS-Chem est un CTM mondial basé sur les observations météorologiques du système d'observation de la Terre Goddard (GEOS) du Bureau mondial de modélisation et d'assimilation de la NASA (Bey et al., 2001). Le package microphysique TOMAS (« Two Moment Aerosol Sectional ») est intégré à GEOS-Chem (GC). « Sectionnel » fait référence à la capacité de TOMAS à traiter les sections (bacs) d'un PSD tandis que « Two Moment » fait référence au fait qu'il existe deux quantités physiques calculées pour chaque bac et chaque cellule du domaine 3D GCT : la masse et nombre d'aérosols (plus de détails peuvent être trouvés dans l'article 2).

Dans cette thèse, nous avons cherché à mieux comprendre les tendances saisonnières microphysiques et optiques des aérosols dans l'Arctique et dans quelle mesure un modèle sectionnel comme TOMAS peut simuler les processus détectables à l'aide de l'optique de télédétection (colonne). Plus précisément nous avons cherché à :

- 1) Étudier les paramètres FM et CM intensifs et extensifs des aérosols arctiques à l'échelle climatologique à l'aide des inversions d'AERONET du photomètre solaire/radiomètre du ciel. L'un de nos principaux objectifs était de mieux comprendre ces paramètres de 1er et 2ème ordre afin d'évaluer les performances des simulations de modèles sectionnels.

2) Évaluer les paramètres optiques et microphysiques de GEOS-Chem TOMAS. L'objectif vise à mieux connaître et comprendre la façon dont le modèle capture les propriétés et la dynamique des aérosols arctiques. La comparaison du modèle avec les observations a permis d'estimer la précision du paramétrage du modèle. Le processus d'évaluation a donné un aperçu des performances du modèle et a mis en lumière les domaines de développement possibles.

La 1^{ère} hypothèse de cette étude (associée à l'article 1) était qu'une variation saisonnière significative des paramètres clés de récupération FM et CM (une climatologie) pourrait être établie sur une série de stations AERONET de l'Arctique. Le moyen de valider cette hypothèse était de montrer que la variation saisonnière était significativement plus importante que les écarts-types pluriannuels et mensuels de ces paramètres et que des tendances saisonnières cohérentes étaient évidentes dans le réseau de stations de l'AERONET de l'Arctique.

La 2^{ème} hypothèse de cette étude (associée à l'article 2) était que le modèle prédit de manière adéquate les paramètres à forte intensité d'aérosols dans la région arctique avec divers degrés de corrélation et de précision selon le modèle et les limites de récupération. La validation de l'hypothèse a été réalisée en comparant des mesures au sol et des moyennes climatologiques avec des paramètres analogues simulés par un modèle. Le succès a été défini en obtenant des erreurs de biais du modèle rms inférieures aux écarts types de la climatologie de l'AERONET.

Nos résultats de recherche ont été diffusés dans deux articles évalués par des pairs. Le premier article a déjà été publié dans le Journal of Geophysical Research: Atmospheres en avril 2020. Le second a été soumis à Atmospheric Environment en septembre 2021.

Le premier article (article 1, chapitre 2 ci-dessous) décrit une étude saisonnière à l'échelle climatologique des aérosols au-dessus de l'Arctique à l'aide de mesure au sol pluriannuelles de six stations AERONET (allant de Barrow en Alaska à Hornsund au Svalbard. Nous avons étudié divers paramètres microphysiques et optiques : les distributions granulométriques volumique (PSD), FM et CM AOD, FMF, et les rayons effectifs FM et CM. Ces paramètres ont été acquis sur une période de 7 à 20 ans en fonction de la disponibilité les données à chaque station.

Mis à part l'approche FM et CM, nous avons rapporté nos AOD moyennes mensuelles en termes de statistiques géométriques (sur la base de l'hypothèse, comme, par exemple, résumée dans l'article 1 que les histogrammes totaux, FM et CM AOD sont normalement distribués dans un espace logarithmique). Cette représentation peut, selon nous, être importante pour la paramétrisation précise

de l'impact des aérosols de modèles climatiques. Une distribution lognormale apparaît comme une distribution asymétrique positivement asymétrique dans l'espace AOD linéaire : cela signifie que les statistiques arithmétiques traditionnelles peuvent être assez sensibles aux valeurs aberrantes et que des mesures omniprésentes telles que la moyenne arithmétique peuvent surestimer de manière significative les AOD (et donc, par exemple, surestimer l'impact de la nucléation des nuages des aérosols associés).

Les résultats ont démontré l'existence de tendances saisonnières robustes du printemps à l'automne ainsi que des caractéristiques spécifiques de PSD au printemps et en été. L'exemple le plus notable du premier était une augmentation faible mais robuste de la position du rayon du pic de mode fin pour presque toutes les stations : une augmentation que nous avons attribuée à l'influence progressivement décroissante des particules de brume arctique FM de petite taille et à l'influence croissante des plus grandes particules de fumée FM de taille réduite. L'exemple le plus remarquable d'une caractéristique robuste était un pic de PSD panarctique (et pancanadien), printanier d'environ 1,3 μm que nous avons attribué à la poussière asiatique. La diminution du printemps à l'automne de l'amplitude du pic printanier a entraîné une diminution progressive de l'AOD CM dans toutes les stations. Le message principal de ce document, et un élément essentiel de son originalité, était la robustesse de ces tendances et fonctionnalités à travers le réseau de 6 stations.

Le deuxième article (Article 2, Chapitre 3 ci-dessous) est une comparaison des simulations saisonnières GCT de l'Article 1 pour l'année 2015. La comparaison a été réalisée au niveau climatologique (saisonnier) et au niveau annuel : 1) dans un premier temps nous avons cherché à étudier comment GCT a capturé des tendances saisonnières robustes malgré le fait qu'il soit limité à un an de simulations et 2) dans le deuxième cas, nous avons cherché à comprendre à quel point les simulations de GCT étaient sensibles aux événements en 2015 (comment se comparent-elles aux inversions d'AERONET limitées à 2015?) : des différences significatives étaient inévitablement liées à la survenue d'événements AOD (fumée) extrêmes au cours de cette année.

Les découvertes notables et originales étaient que le GCT PSD a capturé (à toutes les stations) le pic de CM de petite taille au printemps (le pic de 1,3 μm qui a été attribué à la poussière asiatique dans le papier 1) ainsi que la diminution du printemps à l'automne de l'AOD CM et l'augmentation concomitante du FMF. D'un autre côté, il n'a pas réussi à capturer l'augmentation de la taille des particules FM pendant la transition du printemps à l'été. Cela a été attribué à la sous-estimation probable de la taille des particules de fumée par GCT : son incapacité à simuler la coagulation sous-

grille (taille de cellule GCT inférieure à $4^\circ \times 5^\circ$) des particules de fumée a conduit à une sous-estimation (toutes les stations) du rayon effectif FM par rapport aux inversions d'AERONET. Pour tester cette affirmation, nous avons montré qu'un changement du rayon effectif FM des sous-estimations du GCT aux valeurs AERONET (pour le mois de fumée extrême de juillet 2015) entraînait des AOD FM GCT de l'ordre des valeurs AERONET. Une augmentation faible mais robuste du PSD CM GCT à la fin de l'été et à l'automne a suggéré un lien avec le sel de mer CM et/ou la poussière locale. En fin de compte, nous avons constaté que GCT avait largement capturé toutes les tendances et caractéristiques observées dans l'article 1. Les limites de cette affirmation étaient attribuées à sa résolution spatiale grossière, le plus petit rayon supérieur de son PSD et les défauts de son package de coagulation. Ce dernier ayant été corrigé depuis lors avec un correctif qui tient compte de la physique "sub-grid" de coagulation (sous la taille des cellules de $4^\circ \times 5^\circ$).

1. Introduction

In recent decades, aerosols have progressively gained a new level of interest from the research community in terms of the radiative forcing role they play in climate change. According to Hinds (1999) aerosols can be defined as “a suspension of solid or liquid particles in a gas”. They can be of a natural origin, such as sea-salt and desert dust, or of an anthropogenic origin such as particulate pollution from industrial emissions. Most of these particles are known to have a (direct) cooling effect (relative to the warming caused by greenhouse gases) because they mostly backscatter incoming solar radiation (Boucher et al., 2013). Strongly absorbing aerosols such as black carbons can have a lesser but significant warming effect (see the iconic “radiative forcing estimates” figure of Boucher et al., 2013). The second (indirect) way in which aerosols influence climate is through the agency of aerosol-cloud interactions; aerosols acting as cloud-droplet or ice-cloud nuclei impact cloud microphysical and optical properties (ibid).

Aerosols sizes vary according to their composition and method of generation. Their associated microphysical and optical properties can be divided into two categories. “Extensive” properties are quantity dependent: in aerosol remote sensing research the most widely used extensive property parameters is the aerosol optical depth (AOD). The AOD is primarily an indicator of the number concentration of aerosols in an atmospheric column: their number concentration impact is manifested by their intrinsic absorption and scattering properties. The second category relates to “intensive properties” (per-particle or non-quantity dependent) such as size, shape, and composition: these types of slowly varying parameters provide indications of the origins of the aerosols. They also can be sensitive to meteorological parameters, such as the size increasing influence of relative humidity (see, for example, Tang, 1996). The effective radius as well as other radius markers of key features of the particle-volume size distribution (PSD¹) are important intensive parameter examples in our research work. Finally, a property subcategory can be referred to as “semi-intensive” or “semi-extensive”: these, as such labelling suggests, are a combination of extensive and intensive parameters. An important example of a semi-intensive parameter is the fine mode fraction (FMF) which is the ratio of fine mode AOD to total AOD at a reference wavelength. A second, classical example of a semi-intensive parameter is the generic Angstrom exponent (often labelled as α). This exponent (derived

¹ The volume of all particles per unit increment in the logarithm of the radius per unit area (see Appendix A for details)

from the first order approximation that the AOD varies as $\lambda^{-\hat{\alpha}}$) is a robust, if primitive, indicator of aerosol particle size (Power, 2003).

An important concept in our research (central to the analysis strategy of Paper 1 and Paper 2) is the bimodality feature of the PSD: for most optical purposes the PSD can be divided into a submicron (fine mode or FM) component and a supermicron (coarse mode or CM) component (see Paper 1 for details). The employment of this robust concept enables deeper insights into the analysis of aerosol property trends, their possible sources, and the dynamical processes that control their evolution. For further details on the equations of our microphysical and optical properties utilized in this work please see Paper 1 and Appendix A.

1.1 Arctic aerosols.

The Arctic is an important and sensitive region that experiences the most severe impacts of climate change. The latest Arctic Monitoring and Assessment Programme (AMAP) report states that the average Arctic temperature has increased three times faster than the global average in the last 49 years (AMAP, 2021). The 6th IPCC assessment report states that the Arctic temperature will continue to rise at a rate more than twice that of the global warming (IPCC, 2021). This phenomenon dubbed “Arctic amplification” has triggered a rapid change in the Arctic’s environment which, in turn, contributes to local and global concerns. Reductions in sea ice extent and snow cover have, for example, contributed to the global sea level rise (Slater et al., 2020) as well as increases in the local dust content (see for example Udisti et al., 2020 on general Arctic impacts).

Various types of aerosols from local or distant sources can be found in the Arctic atmosphere throughout the year. During the late-winter and spring seasons aerosols from mid-latitude, anthropogenic sources are transported into the Arctic. This results in the recurring ‘Arctic haze’, whose principal component is [FM]² sulphates, in addition to black carbon (BC) (Abbatt et al., 2019). While the sulphate component is largely a cooling contribution due to solar backscattering, the BC component plays a unique role in warming the Arctic by its absorption capacity in the atmosphere and by direct deposition on snow and ice: this latter effect causes a decrease in the surface reflectance (Abbatt et al., 2019), and thus enhances melting. CM dust has a similar reflectance reduction effect: dust of Asian and local origin (see, for example, Groot Zwaafink et al., 2016) also have a deposition impact during the Arctic spring (for more on dust in the Arctic see Bullard et al. (2016)). CM sea-

² Expressions in [] in any affirmation is not attributed to the referenced citation and is solely the author’s opinion.

salt is also a contributor to the haze due to the additional presence of stronger winds in the winter and spring (see for example Abbatt et al., 2019, and Huang & Jaeglé, 2017). During the late spring and early summer, the Arctic haze starts to decline while making way for increased smoke (natural BCs and organic carbons) events whose origins are attributable to biomass burning from boreal forest fires and/or agricultural fires from different continental regions (Canada, Alaska, Europe, and East Asia: see for example Eck et al., 2009). Volcanic eruptions can also contribute to summer aerosols (see for example Breider et al., 2014).

A critical concept in seasonal Arctic dynamics is the polar dome (concentric dome-shaped surfaces that define preferred pathways for the transport of particles into the Arctic) and its fundamental influence on the Arctic haze (Law & Stohl, 2007). As the summer emerges, the retracted polar dome and the varied weather conditions result in longer residence times of natural aerosols that are confined to lower altitudes (Abbatt et al., 2019). At the same time pollution from long-range transport exists at higher altitudes (Law & Stohl, 2007, Schmale et al., 2021). Details on typical aerosol transport pathways into the Arctic can be found in Chapter 4 of Udisti et al.(2020). Further details on Arctic aerosols can be found in Abbatt et al. (2019).

1.2 Investigating Arctic Aerosols

Ground- and satellite-based remote sensing are critical tools for monitoring and studying optical and microphysical aerosol parameters. We made use of the renowned and widely used AERONET retrievals available at various Arctic stations in our research. AERONET (Aerosol Robotic Network) is a network of sun photometers/sky radiometers that provide retrievals of aerosol microphysical and optical properties. AERONET retrievals have been extremely useful for Arctic aerosol studies (despite the obvious challenges of providing high-quality, long-term measurements in the Arctic).

Chemical and microphysical algorithms built into meteorological dynamics models to achieve spatio-temporal simulations of gas and particle evolution are an essential tool for interpolating, extrapolating and, more importantly, better understanding the physics of what are generally spotty and irregular measurements of aerosols (especially in the Arctic). Chemical Transport Models (CTMs) are spatio-temporal models that simulate atmospheric chemistry and can represent the evolution of different chemical species. They are used, along with specific aerosol microphysical packages, to better understand the processes that control the spatial and temporal distributions of aerosols as well as their chemical transformations and removal (see, for example, Chin et al., 2019). AERONET retrievals have been extensively used in model evaluation studies. These studies have, however, been largely

limited to the generic first order parameters of AOD at a single wavelength and the Angstrom exponent. One of the innovations of our research is to compare model simulations with the essentially second order parameters associated with the FM and CM division of the PSD (where the FM and CM components are essentially intensive parameters such as the FM or CM effective radius or extensive parameters such as the FM or CM AOD). In general, the practice of utilizing remote sensing (columnar) measurements for model evaluation is a robust first step to increasing the accuracy of model simulations at any point in the atmosphere (see also the discussion in the introduction of Paper 2).

The model that we employed for comparisons with our FM and CM AERONET retrievals was GCT (GEOS-Chem TOMAS). GEOS-Chem is a global CTM that is driven by the meteorological observations from the Goddard Earth Observing System (GEOS) of the NASA Global Modeling and Assimilation Office (Bey et al., 2001). The TOMAS (“Two Moment Aerosol Sectional”) microphysical package is integrated into GEOS-Chem (GC). “Sectional” refers to the capacity of TOMAS to deal with sections (bins) of a PSD while “Two Moment” refers to the fact that there are two physical quantities computed for every bin and every single cell in the 3D GCT domain: mass and number of aerosols (more details can be found in Paper 2).

1.3 Objectives

In this thesis, we sought to better understand microphysical and optical seasonal trends of aerosols across the Arctic and the extent to which a sectional model like TOMAS can simulate those processes which are detectable using remote sensing (columnar) optics. More specifically we sought to:

- 1) Study intensive and extensive, FM and CM parameters of Arctic aerosols on a climatological-scale using sun-photometer/sky radiometer AERONET retrievals. One of our principal aims was to better understand these 1st and 2nd order parameters in order to evaluate the performance of sectional model simulations.
- 2) Evaluate optical and microphysical parameters of GEOS-Chem TOMAS. The aim was to facilitate a better understanding of how well the model captures Arctic aerosol properties and dynamics. The comparison of the model with observations enabled an estimation of model parameterization accuracy. The evaluation process gave insight into model performance and shed light on possible areas of development.

1.4 Hypotheses

The 1st hypothesis of this study (associated with Paper 1) was that a significant seasonal variation of key FM and CM retrieval parameters (a climatology) could be established over a series of Arctic AERONET stations. The means of validating this hypothesis was to show that the seasonal variation was significantly larger than the multi-year, monthly-binned standard deviations of those parameters and that coherent seasonal trends were evident across the network of Arctic AERONET stations

The 2nd hypothesis of this study (associated with Paper 2) was that the model adequately predicts aerosol intensive parameters over the Arctic region with varying degrees of correlation and accuracy depending on model and retrieval limitations. The validation of the hypothesis was achieved by comparing ground-based, climatologically averaged retrievals with analogous, model simulated parameters. Success was defined by achieving rms model bias errors that were less than the standard deviations of the AERONET climatology.

1.5 Articles and article originality

Our research results have been disseminated into two peer-reviewed articles. The first paper has already been published in the Journal of Geophysical Research: Atmospheres in April 2020. The second was submitted to Atmospheric Environment in September 2021.

1.51 Article 1: Climatological-scale study of aerosol properties

The first article (Paper 1, Chapter 2 below) describes a climatological-scale, seasonal study of aerosols over the Arctic using multi-year, ground-based retrievals of six AERONET stations (stretching from Barrow in Alaska to Hornsund in Svalbard). We investigated various microphysical and optical parameters: the particle-volume size distributions (PSDs), FM and CM AOD, FMF, and FM and CM effective radii. These parameters were acquired over a period of 7-20 years depending on the availability of retrievals at each station.

Aside from the FM and CM approach we reported our monthly averaged AODs in terms of geometric statistics (based the assumption, as, for example, summarized in Paper 1 that the total, FM, and CM AOD histograms are normally distributed in logarithmic space). This representation can, we would argue, be important to the accurate parameterization of climate-model aerosol packages. A lognormal distribution appears as a positively skewed, asymmetric distribution in linear AOD space: this means that traditional arithmetic statistics can be quite sensitive to outliers and that ubiquitous measures such as the arithmetic mean can significantly overestimate AODs (and thus, for example, overestimate the cloud nucleation impact of the associated aerosols).

The results demonstrated the existence of robust spring-to-fall seasonal trends as well as specific PSD features in the spring and summer. The most notable instance of the former was a weak but robust increase in the radius position of fine mode peak for nearly all stations: an increase that we attributed to the progressively waning influence of small-sized FM Arctic haze particles and the increasing influence of larger-sized FM smoke particles. The most remarkable instance of a robust feature was a pan-Arctic (and pan Canadian), springtime, PSD peak of $\sim 1.3 \mu\text{m}$ that we attributed to Asian dust. The spring to fall decrease in the amplitude of the springtime peak incited a progressive decrease in the CM AOD across all stations. The overarching message from that paper, and a critical element of its originality, was the robustness of those trends and features across the network of 6 stations.

1.52 Article 2: Evaluation of GCT simulations with AERONET retrievals

The second article (Paper 2, Chapter 3 below) is a comparison of the Paper 1 seasonal GCT simulations for the year of 2015. The comparison was carried out at the climatological (seasonal) level and the yearly level: 1) in the first instance we sought to investigate how GCT captured robust seasonal trends in spite of it being limited to one year of simulations, and 2) in the second instance we sought to understand how sensitive the GCT simulations were to events in 2015 (how they responded to AERONET retrievals confined to 2015): significant differences were inevitably related to the occurrence of extreme AOD (smoke) events during that year.

Notable and original findings were that the GCT PSD captured (at all stations) the springtime, small-sized CM peak (the $1.3 \mu\text{m}$ peak that was attributed to Asian dust in Paper 1) as well as the spring to fall decrease of the CM AOD and the attendant increase of FMF. On the other hand, it failed to capture the increase in size of the FM particles during the spring to summer transition. This was attributed to GCT likely underestimating smoke particle size: its failure to simulate sub-grid (sub $4^\circ \times 5^\circ$ GCT cell-size) coagulation of smoke particles led to an (all station) underestimation of FM effective radius relative to AERONET retrievals. To test this affirmation, we showed that a change in FM effective radius from the GCT underestimates to the AERONET values (for the extreme smoke month of July 2015) resulted in GCT FM AODs that were of the order of the AERONET values. The details on how we related this affirmation to the original paper describing the failure of GCT in properly accounting for smoke particle coagulation (Ramnarine et al., 2019) are described in Paper 2. In terms of the CM PSD, we noted a weak but robust increase in the GCT CM PSD during the late summer and fall: this suggested a link with CM sea salt and / or local dust.

In the end we found that GCT had largely captured all the trends and features observed in Paper 1: limitations to this affirmation were ascribed to its coarse spatial resolution, its smaller radius upper limit and shortcomings of its coagulation package (the latter having been since corrected with a sub-grid fix that did not require a change in nominal resolution).

2. Paper 1 : Climatological-Scale Analysis of Intensive and semi-intensive aerosol parameters derived from AERONET retrievals over the Arctic



Supporting information for this article can be found [here](#).

JGR Atmospheres

AGU ADVANCING EARTH AND SPACE SCIENCE

Research Article: <https://doi.org/10.1029/2019JD031569>

Climatological-Scale Analysis of Intensive and Semi-intensive Aerosol Parameters Derived from AERONET Retrievals Over the Arctic

Y. AboEl-Fetouh¹ , N. T. O'Neill¹, K. Ranjbar¹ , S. Hesaraki¹, I. Abboud², and P. S. Sobolewski³

¹CARTEL, Université de Sherbrooke, Sherbrooke, Quebec, Canada, ²Air Quality Research Division, Environment and Climate Change Canada (ECCC), Toronto, Ontario, Canada, ³Institute of Geophysics Polish Academy of Sciences, Warsaw, Poland

Corresponding author: Yasmin AboEl-Fetouh (yasmin.ahmed.samy@usherbrooke.ca)

Key Points:

- Spring to summer increase in fine mode (FM) particle size. Likely associated with waning Arctic haze and waxing smoke presence.
- Springtime, coarse mode (CM) feature, of small CM particle radius in the particle size distribution. Likely associated with Asian dust.
- Behavior of FM and CM (intensive, semi-intensive and extensive) properties were largely a function of the first two observations.

Abstract We investigated the climatological-scale, monthly binned, seasonal variation of AERONET/Dubovik retrievals across six stations in the North American and European Arctic (multiyear sampling periods ranging from 8 to 17 years). A robust, spring-to-summer (StoS) increase in the radius of the peak of the fine mode (FM) component of the particle size distribution (PSD) was observed for five of the six stations. The FM aerosol optical depth (AOD) and the FM effective radius at the individual stations showed, respectively, a negligible to moderate StoS decrease and a significant increase. This was interpreted as a trade-off between the waning influence of smaller FM Arctic haze aerosols and the increasing influence

of large FM smoke particles. A springtime, pan-Arctic PSD peak in the 1.3 μm coarse mode (CM)bin was attributed to Asian dust. It was suggested that the increase in amplitude of a second (4–7 μm) CM peak from July to August at the low-elevation coastal sites was influenced by wind-induced sea salt. The CM AOD went through a StoS decrease attributed to the decreasing amplitude of the 1.3 μm peak. A significant StoS CM effective radius increase was ascribed to the decreasing influence of the 1.3 μm peak. StoS FM fraction increases were largely due to the decrease of the CM AOD (decreasing influence of springtime Asian dust). This extensive and intensive climatology of remotely sensed, bimodal properties will, we believe, provide an important reference for future measurements and modeling of Arctic aerosols.

1 Introduction

The dynamics of the Arctic environment has a direct impact on global climate and weather, sea level rise, and in turn commerce (AMAP, 2017). Its impact, therefore, extends much beyond the Arctic Circle. According to AMAP (2017), the Arctic's average temperature has risen twice that of the global average in the past five decades. This phenomenon is known as Arctic amplification. This rise in temperature is mainly attributed to the heating influence induced by absorption of thermal radiation by greenhouse gases (GHGs) (AMAP, 2017). At the same time, it is well established that the greatest uncertainty in the radiative forcing budget is attributed to aerosols via the direct and indirect effect (Boucher et al., 2013). A study by Najafi et al. (2015) sheds light on the additional impact made by aerosols. In the models used to study the influences of GHGs and aerosols on Arctic temperature, they state that 60% of the GHG-induced warming has been offset by the combined response to other anthropogenic forcings and that these forcings were mostly dominated by aerosols (Najafi et al., 2015). It is generally accepted that aerosols mask a fraction of the warming effect caused by increasing GHGs (Boucher, et al., 2015). The uneven distribution of aerosols in the atmosphere results in both warming and cooling of the climate system in a way that impacts the weather (Boucher et al., 2013).

A variety of aerosols, from both anthropogenic and natural sources, can be found in the Arctic atmosphere. In general, they are transported from lower latitudes along isentropic pathways to the mid or upper Arctic troposphere. They can also originate locally from erosive and water-surface interactions over the land and ocean (see Tomasi et al., 2015 for a detailed overview of the sources

of Arctic aerosols). There are two main formation mechanisms for aerosols: primary aerosols that are injected directly into the atmosphere and secondary aerosols formed from gas-to-particle conversion processes (Seinfeld & Pandis, 2006). The formation mechanisms result in different types of aerosols having different microphysical properties. In general, the sizes of an ensemble of aerosols can be characterized by their particle size distribution (PSD; see, e.g., Hinds, 1999). The PSD is partitioned into modes that occupy different size regimes. The particle sizes range from radii of about 1 to 10 nm for ultrafine particles to 100 μm for larger particles such as dust and pollen. Generally, 1 μm is the cut-off between submicrometer (submicron) and supermicrometer (supermicron) particles. From the standpoint of optical properties (the properties that one can hope to detect using visible and near-infrared remote sensing), aerosols are largely bi-modal: their PSD is effectively represented by a sub-micron or fine mode (FM) component and a super-micron or coarse mode (CM) component. This bimodality feature is largely a consequence of the differing formation and transportation mechanisms that generate different species of aerosols. It informs the manner in which we present the climatological-scale trends in this paper.

Aerosol properties can be divided into two categories: extensive and intensive. The extensive category deals with the quantity of aerosols (the number or total projected area or total volume of all aerosols in a unit volume of air or per unit area for a column measurement). The intensive category refers to per particle properties that vary with aerosol particle size, shape, and nature. We will refer to “semi-intensive” parameters as any parameter that is some constrained combination of intensive and extensive parameters.

The passive remote sensing measurements that we employ to investigate aerosol columnar properties are acquired using the CIMEL instruments of AEROCAN and AERONET (AEROCAN is a federated subnetwork of AERONET). AERONET is a worldwide network of ground-based, automated sun and sky scanning radiometers (further information is given in section 2.1). The ground-based CIMEL instruments are used to retrieve various aerosol parameters by exploiting the spectral dimension of atmospheric solar extinction measurements and the angular dimension of sky radiance measurements. The outputs of the AERONET (Dubovik) retrieval scheme are PSD and refractive index as well as total, FM, and CM aerosol optical depth (AOD).

Tomasi et al. (2015) presented the climatological-scale, optical characteristics of Arctic atmospheric aerosols for a 20-year sampling period. Their results showed a seasonality of columnar aerosol extinction parameters (the total AOD at 500 nm and the total Angstrom exponent derived from a

multi-wavelength regression). This seasonality was (for a variety of sites in the American, Canadian European and Russian Arctic) characterized by small total Angstrom exponents and large AODs in the winter-spring season transforming to large total Angstrom exponents and small AODs in the summer-autumn season (c.f. their Figure 8). Stone et al. (2014) analyzed 10 years of spectral AOD measurements over Barrow, Alert and Ny Alesund: they roughly found the same type of spring to summer AOD versus total Angstrom exponent inversion reported by Tomasi et al.(2015). von Hardenburg et al. (2012) carried out a 6-year, six station seasonal analysis of AERONET AODs and total Angstrom exponent within a model and satellite AOD comparison context. They found higher springtime versus summer AOD values for the high latitude sites and more mixed results at lower latitudes (with summer AOD values being comparable or larger than the springtime values) while Angstrom exponents roughly peaked in the summer. All of these authors indicate that late winter and early springtime episodes over the Arctic are mainly connected by the seasonal phenomenon known as the Arctic haze; a mixture of gases such as ozone precursors and aerosols such as sulfates, black carbon and pollution-entrained dust (Law & Stohl, 2007). Hesaraki et al., (2017) looked at 4 years of sun photometer/sky radiometer AERONET retrievals from a number of Arctic research stations in or near to the Canadian Arctic. Their analysis focused on FM AOD and CM AOD trends between April to September. They noted, for example, a weak multi-station springtime peak in CM AOD, which they ascribed to the influence of springtime Asian dust. They also noted that the OPAL and PEARL AODs as well as the Thule AODs were representative of less turbid conditions with significantly smaller AOD variances than Barrow and Resolute Bay.

The papers described in the previous paragraph deal with climatological-scale analyses of the extensive AOD parameter (or the FM and CM sub-division of the AOD in the case of Hesaraki et al., 2017). With the exception of the generalized Angstrom exponent (effectively a semi-intensive parameter related to average particle size over the total PSD), there has been little investigation of intensive or semi-intensive parameters. These parameters, because they represent types and sizes of particles (each type being associated with its own particular emissions source), tend to be regional and daily in their spatial and temporal range. Intensive parameters include the average size and width of the total, FM and CM PSDs (such as effective radius and width as defined by Hansen and Travis, (1974) and the refractive index. Semi-intensive parameters include the normalized PSD (the PSD normalized by its integral over particle size), the fine mode fraction (FMF; see below) and the above-mentioned total Angstrom exponent.

This paper is a comprehensive continuation of the extensive FM and CM AOD analysis carried out by Hesaraki et al., (2017). In addition to the present focus on the behavior of Arctic PSDs as well as the associated intensive and semi-intensive FM and CM parameters we have extended the MYSP (multi-year sampling period) of the Arctic stations to durations that range from 8 to 17 years. To the best of our knowledge, this is the first publication that deals with a station-by-station climatological-scale, seasonal analysis of Arctic PSDs and the interpretation of these PSDs in terms of the seasonal variation of intensive and semi-intensive FM and CM parameters (as well as extensive FM and CM parameters). Xie et al. (2018) carried out a multi-year investigation (for an Arctic to high-Arctic ensemble of eight sites) of the FMF and its relation to total AOD at 500 nm. They also performed a somewhat limited seasonal analysis of the two variables (limited in the sense that they did not quantify the seasonal FM and CM AOD variations in their analysis of the FMF and AOD variations). They additionally carried out a validation of absorption AOD (but over a very small fraction of events satisfying the very turbid AERONET threshold of AOD (440 nm) being > 0.4 for the retrieval of refractive index). Sioris et al. (2017) carried out a multi-year climatological-scale study of 20 AEROCAN sites (including three of the Arctic sites employed in this study). They characterized the seasonal and spatial variations of AOD and its FM and CM components, PM_{2.5} (particulate matter with a 2.5 μm cutoff in diameter) as well as the diurnal and weekly variability and dependence on wind direction across a subsample of sites.

1.1 AOD speciation and its seasonal variation

Aerosol speciation can often be deduced or narrowed down given estimates of the average refractive index. However, AERONET retrieval outputs in the Arctic generate little or no direct aerosol species information given the prohibitively restrictive “turbid-AOD” threshold for refractive index retrieval (as per the previous section). Hence, we turn to model simulations to better understand the general aerosol speciation trends in the Arctic: GEOS-Chem-simulated seasonality of the main aerosol constituents that contribute significantly to the FM and CM AOD in the Arctic region are shown in Figure 1 (4-year averages over five of the six stations employed in this paper; however, the speciation results are generally not very sensitive to the choice of stations nor the choice of sampling period). CM as well as FM Asian dust is a recurring springtime event, as is the Arctic haze (see, respectively, the dust CM and FM AOD and the sulphate (SO_4) FM AOD in Figure 1). Biomass burning is both a springtime and summertime event (see the AOD associated with organic carbon (OC) in Figure 1 with a relatively small peak in the spring and a dominant peak in the summer). Figure 1 also indicates

that CM sea-salt is expected to peak in the late winter and mid-summer when cyclonic depressions generate greater wind speeds over the Arctic and Atlantic oceans. While BC AOD is an important absorptive product of smoke (see, for example the AAOD species plot in Figure 9(b) of Breider et al., 2014), its weak springtime contribution to the extinction AODs of Figure 1 is masked by the dominating FM SO₄ AOD component, the principle component of Arctic haze. The general transport pathways that eventually lead to such patterns of AOD speciation are discussed, for example in Stone et al. (2014) and Tomasi et al. (2015). A discussion of the Arctic dome and lower tropospheric Arctic haze as well as isentropic lift of southerly aerosol sources to the mid and upper Arctic troposphere can be found in Law & Stohl (2007).

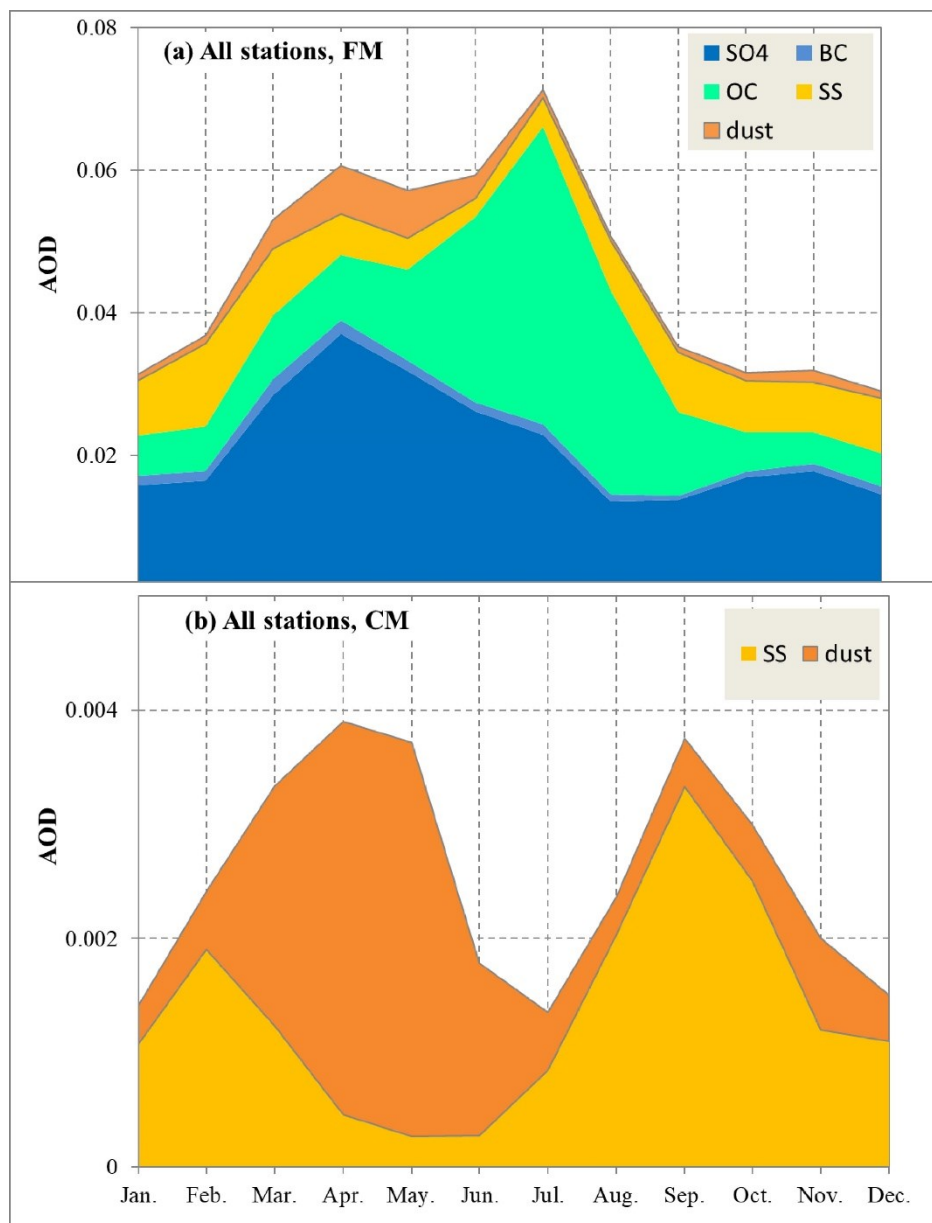


Figure 1 Monthly AOD (arithmetic) averages for different aerosol species as generated by the GEOS-Chem model at a wavelength of 550 nm (Hesaraki et al., (2017)). The native resolution of the simulations was 6 hours. The monthly averaged AODs were themselves arithmetically averaged across 5 Arctic stations: OPAL and PEARL, Resolute Bay, Barrow, and Thule over the 2009 – 2012 period. (a) FM AOD seasonal variation, (b) CM AOD seasonal variation. Acronyms: OC = organic carbon, BC = black carbon, SS = sea salt, SO4 = sulphates.

2 Instrumentation and Research Sites

2.1 Instrumentation

For the purposes of this study, we chose stations spread across the North American and European Arctic. We employed retrievals from six AERONET sites of which four were part of the AEROCAN network (c.f. Figure 2). Holben et al., (1998) give an overview of the AERONET network along with

methodological descriptions of the instruments, the optical background and the processing standards to achieve the output products. Ground-based AERONET/AEROCAN data are of two sorts: high frequency (typical three-minute sampling time) AODs and low-frequency almucantar radiance scans (nominally once per hour). The data derived from these instruments has been an essential source of column integrated and averaged information for aerosol researchers. The higher frequency AOD data is used to investigate event-level phenomena while the lower frequency but more optically diverse AOD and almucantar scans are employed in climatological scale analyses (see, for example, Hesaraki et al., 2017).

2.2 Research Sites

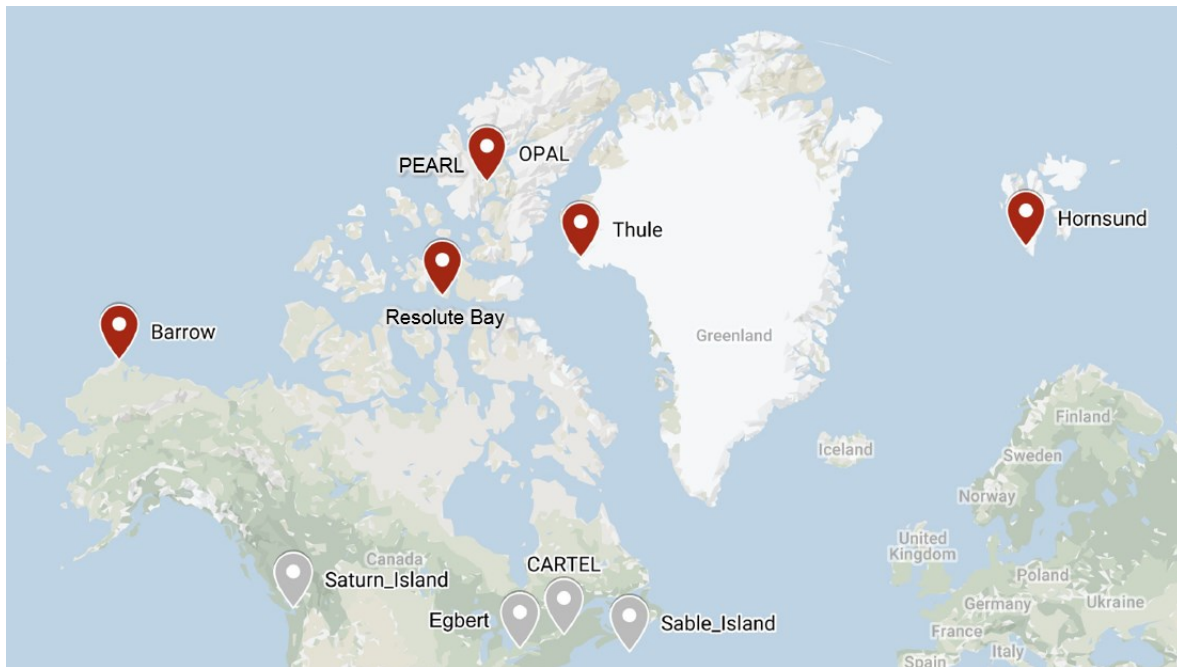


Figure 2 A map showing the research sites whose data was employed in this study. The five Arctic stations covering the North American Arctic and the single station representing the western part of the Euro-Asian Arctic (Hornsund) are shown in red. Four Southern stations, shown in gray, were considered for comparative purposes.

Table 1 Coordinates and MYSP of the Arctic and southern stations whose retrievals were employed in this study.

Station	Latitude	Longitude	Elevation (m)	Time Period (MYSP)
Arctic Stations				
PEARL- Eureka, Nunavut, Canada	80.05° N	86.42° W	615	2007 – 2018
OPAL-Eureka, Nunavut, Canada	79.99° N	85.94° W	5	2008 – 2018

Thule, Denmark	76.52° N	68.77° W	225	2007 - 2018
Hornsund, Norway	77.00° N	15.56° E	12.44	2005 – 2015
Barrow, Alaska, USA	71.31° N	156.67° W	8	1999 – 2018
Resolute Bay, Nunavut, Canada	74.73° N	94.90° W	35	2004 – 2017
Southern Stations				
Egbert, Ontario, Canada	44.23° N	79.75° W	264	1997 – 2018
Sable Island, Halifax - Nova Scotia, Canada	43.93° N	60.01° W	3	2010 – 2014
Saturna Island, British Columbia, Canada	48.78° N	123.13° W	193	1998 - 2018
CARTEL, Sherbrooke, Canada	45.38° N	71.93° W	251	1995 - 2018

The Arctic stations listed in Table 1 include, for comparative reasons, the five stations (Barrow, Resolute Bay, OPAL, PEARL, and Thule) whose data was employed in Hesaraki *et al.* (2017). To these stations, we added the high-Arctic AERONET station of Hornsund. This addition was made so that we could compare the similarities and differences between our high Arctic: North American stations of OPAL, PEARL and Thule with a high-Arctic station in the European Arctic. Barrow, representing the low Arctic in the west of the North American Arctic is located on the north coast of Alaska. This site provides AOD information on trans-Pacific dust aerosols during the spring and smoke aerosols during the summer (Stone et al., 2007, 2014) as well as information on marine aerosols from onshore breezes during the summer and autumn period when the ocean is ice free (Stone et al., 2014). Resolute Bay, representing a higher latitude site in the western North American Arctic (south coast of Cornwallis Island) is subject to AOD influences that are generally similar to Barrow (Hesaraki et al., 2017).

The PEARL (Polar Environment Atmospheric Research Laboratory) complex at Eureka, NV on Ellesmere Island, consists of two CIMEL sites: the PEARL Ridge Lab (referred to as PEARL on the AERONET web site) and the Zero elevation Polar Atmospheric Lab (OPAL). OPAL and PEARL are about 15 km apart and are at different elevations (Table 1). This offers an important degree of redundancy that allow us to confirm the robustness of interesting features that we find in the optical retrievals. They can underscore similar and sometimes quite weak trends while consistent differences may be indicative of (typically weak) local or elevation-related phenomena.

3 Processing methodology

3.1 Fundamental optical and microphysical parameters

The general relationship between the combination of PSD and refractive index and derived optical parameters are discussed, for example, in Hansen and Travis (1974). The relationship between the PSD and the types of optical parameters that we employ in this paper are discussed, in O’Neill et

al. (2001). Aerosol optics tend to be more closely aligned with the volume PSD (the volume of all particles per unit volume of air for “point-volume” parameters or the volume of all particles per unit surface area for columnar parameters): the volume PSD (and, for that matter, the surface PSD) is a better representation of the strength of scattering and absorption contributions across all particle sizes (the multiplicative integrand that converts the PSD to an optical parameter is more balanced across the radius spectrum in the case of the volume and surface PSDs) .

The aerosol volume PSD, in terms of optical impact, can be divided into FM and CM PSDs (O’Neill et al., 2001) that are typically associated with different aerosol types and origins. If one accepts the premise that aerosols are essentially bimodal (at least as far as their visible and near infrared optical effects are concerned), then the total AOD at a reference wavelength can be written (O’Neill et al., 2001);

$$\tau_a = \tau_f + \tau_c \quad (1)$$

where τ_f and τ_c represent the (extensive parameter) FM and CM AODs respectively.

The semi-intensive FMF parameter is defined by:

$$FMF = \frac{\tau_f}{\tau_f + \tau_c} \quad (2)$$

Its limitation to values between 0 and 1, while being subject to the extensive parameter variations of τ_f and τ_c , is the most common example of a semi-intensive parameter. It indicates the relative FM optical strength while its coarse mode fraction complement (CMF = 1 - FMF) measures the relative CM optical strength.

Hansen and Travis (1974) define the effective radius, which itself is an approximation to an optically effective radius, as the mean radius, weighted by the (projected) surface PSD across a radius integration-interval. The FM and CM effective radii ($r_{eff,f}$ and $r_{eff,c}$) are defined by radius integration-intervals that straddle the FM and CM radius intervals (how those intervals are defined is described in the next section). They represent nominally intensive parameters that, in fact, represent a weighted mean of all $r_{eff,f}$ and $r_{eff,c}$ values in a given atmospheric column (i.e an altitude mean of their weighted radius mean).

3.2 AERONET retrievals

A long-term and continuous database of aerosol optical, microphysical, and radiative properties is readily accessible on the AERONET website. The Dubovik algorithm (Dubovik & King, 2000) is used to invert the combination of the AOD spectra and the almucantar radiances at the frequency of the latter. The data derived from these instruments has been an important source of column averaged aerosol information for applications ranging from satellite AOD validation to the evaluation of aerosol transport models. The fundamental Dubovik inversion product is the columnar-averaged PSD across 22 logarithmically spaced points (bin centers) from 0.05 to 15 μm (see Table S1 in the supporting information) and columnar-averaged refractive index (assumed constant across all size bins). These, in turn, can be transformed into the fundamental optical parameters of column-averaged aerosol scattering phase function, extinction and absorption AOD. The separation into FM and CM AOD is effected by finding the minimum of the retrieved PSD (limited in the AERONET retrievals to a choice of four bin centers: 0.439, 0.576, 0.756 or 0.992 μm). The physical FM/CM cut off point is then taken as one of those four values, The FM and CM AOD, the FMF, as well as $r_{eff,f}$ and $r_{eff,c}$ can then be derived from optical (generally Mie) calculations applied to the retrieved PSD and refractive index (the same optical calculations that are part of the AERONET radiative transfer retrieval process). This microphysical separation into two modes is not quite the same thing as the spectral separation discussed in O'Neill et al. (2001). This issue is discussed, for example, in Anderson et al., (2005).

We used the recently released Version 3, Level 1.5 retrievals (AERONET, 2019a) for our analysis. The statistical differences between Level 1.5 and Level 2.0 AODs for a given MYSP month were negligible unless the number of Level 2.0 retrievals for that month were very small (as per Hesaraki et al., 2017). The same affirmation applies to the $r_{eff,f}$ and $r_{eff,c}$ retrievals.

3.3 Retrieval errors

Hesaraki et al. (2017) noted that τ_f and τ_c retrieval (residual) errors were significantly less than the amplitudes of the MYSP variability for a given month. The same type of comment, based on estimates of retrieval uncertainty, can be made for the Level 2.0 U27 volume median radius (AERONET, 2019b) and by inference, the retrieval uncertainty in $r_{eff,f}$ and $r_{eff,c}$. From those uncertainty results, and the lack of significant difference between Level 1.5 and numerically significant (having an efficient number of retrievals per month) Level 2.0 products (see the previous section) we can affirm that $r_{eff,f}$ and $r_{eff,c}$ retrieval errors $< \sim 0.02$ and $0.5 \mu\text{m}$ respectively. These

values are typically insignificant relative to the natural MYSP variation during a given month, but they do have some influence on statements made below in the PSD statistics section on the spring to summer movement of the fine mode peak.

3.4 Statistical approach

We interpolated the Dubovik retrieval products (computed at 440, 670, 879 and 1020 nm) to 550 nm. This is the standard wavelength used by aerosol modelers (see, e.g., Brieder et al., 2014) and for certain satellite aerosol products (e.g., MODIS AOD).

The temporal bin sizes for all statistical computations (averages and standard deviations) are months. The statistics we employed for AODs were the geometric mean and geometric standard deviation ($\tau_{x,g}$ and μ_x as per the symbol and acronym glossary). For all other parameters, we employed the arithmetic mean and standard deviation (y and $\sigma(y)$ for parameter “ y ”). In general, AODs are better represented by geometric statistics (O'Neill et al., 2000, Sayer & Knobelspiesse, 2019). The arithmetic and geometric statistics can be related by simple approximate expressions (Hesaraki et al., 2017), and because most researchers tend to employ arithmetic AOD statistics, we generally follow suit. However, in this case, we chose to present the (appropriate) geometric statistics and let the arithmetic statistics users estimate the arithmetic mean and standard deviation analogues from the same simple expressions.

Although, the AERONET (Dubovik retrieval) products undergo a cloud screening and radiance QA process, an additional 3σ outlier exclusion filter was applied to the CM AOD retrievals. This was to lessen artifacts due to contamination by temporally or spatially homogenous clouds (Hesaraki et al., 2017). Other filters included removing any months with 10 or fewer retrievals in order to ensure an acceptable degree of statistical significance. Additionally, months repeated less than three times over the MYSP were excluded from the ensemble MYSP statistics. However, when performing sensitivity robustness tests in comparison with a shorter MYSP, the latter filter was not used (more details in section 4.3).

The comparison of 3σ CM AOD (outlier) filtering versus no filtering generally had little AOD impact with the exception of the month of April at Barrow, Resolute Bay and OPAL, where the $\Delta\tau_{r,g}$ and $\Delta\tau_{c,g}$ differences were as large as 0.004 and 0.002 respectively (c.f. Table S2 in the supporting information). We should add the following caveat however : our experience with co-located lidar measurements suggests that the possibility of CM results being influenced by residual cloud (residual

cloud that might have slipped through the standard cloud screening process for Dubovik retrievals and our 3σ filter mentioned above) cannot, in general, be excluded (at least at the event level). Cloud optical depths that escaped filtering can still be significantly greater than CM AODs, and this can thus unduly influence the amplitude of the CM AODs and the associated PSDs.

4 Results

4.1 PSD statistics

Figure 3 shows the retrieved, monthly averaged PSDs for all six stations across the total MYSP of each station (color coded for the different months of the season). The persistency of certain features across a wide geographic swath of measuring stations suggests the influence of regional, pan-Arctic phenomena. Discussions of the station-by-station FM and CM parameter tendencies associated with the PSD variations of Figure 3 are left to the dedicated FM and CM sections that follow this PSD overview. Important features of the Figure 3 PSDs include a FM peak with a peak radius $\sim 0.15 \mu\text{m}$ and two CM peaks with peak radii $\sim 1 \mu\text{m}$ in the spring and 4 to 7 μm in the late summer and early fall, respectively.

The first CM peak, largely associated with the 1.3 μm bin (c.f. the bin definitions of Table S1 in the supporting information) can be observed for all the Arctic stations for the spring months of April and May (accompanied by a weaker amplitude peak in June). Indeed, this observation has continental scale implications since the same type of springtime peak was observed for all southern stations with the exception of the easternmost Sable Island site. The correlation between the amplitude variation of the 1.3- μm PSD feature in Figure 3 and the $\tau_{c,g}$ variation presented below (Figure 6) strongly suggests that the springtime peak is responsible for most of the τ_c seasonal variation ($R^2 = 0.93$ for the monthly binned ensemble of all stations and MYSPs). The PSD amplitude of those small-radius CM features is larger for the western stations of Barrow and Resolute Bay. Hesaraki et al., (2017) reported a weak springtime, pan-Arctic $\langle \tau_c \rangle$ peak (monthly-binned arithmetic averages) but did not extend their analysis to the actual size of the associated CM particles (and did not include the easternmost station of Hornsund which clearly also shows a springtime peak).

The second CM peak of ~ 4 to 7 μm radius can be seen in the case of the late summer and early fall PSDs. One can observe a systematic increase in the amplitude of this second peak from June to July for all stations and a systematic increase from July to August for the coastal, low elevation sites of Barrow, Resolute Bay and Hornsund (the most notable being that of Resolute Bay).

This case of low-elevation sites may, at least in part, be attributed to wind-induced sea-salt spray aerosol generation that, as suggested by Figure 1, would generally begin to increase in July. Barrow, for example, becomes progressively more influenced by large, lower-atmosphere, sea-salt aerosols as summer progresses (Stone et al., 2014). However, that hypothesis is somewhat tempered by the knowledge that the 2nd CM peaks are nearly all at 4 and 5 μm while most, but not all, sea-salt peaks, at least for southern sites, are located between 2 and 4 μm (see the array of 4 to 8 μm VMD entries in Table 1 of Reid et al., 2006). Some of the increase might, however be attributed to locally, wind-eroded and wind-transported dust as exemplified by Figure 11 of the 15-year Alert climatology reported by Sirois and Barrie (1999) and recently contextualized by Bullard et al., (2016) as the source of a pervasive high latitude phenomenon. Depending on the distance from the source and the type of dust particle, these generally larger particles could push a peak due to both sea-salt and dust to radius values of 4 μm or greater (see, for example, Bullard et al., 2016 who remark on the general confounding optical depth influence of sea-salt and dust).

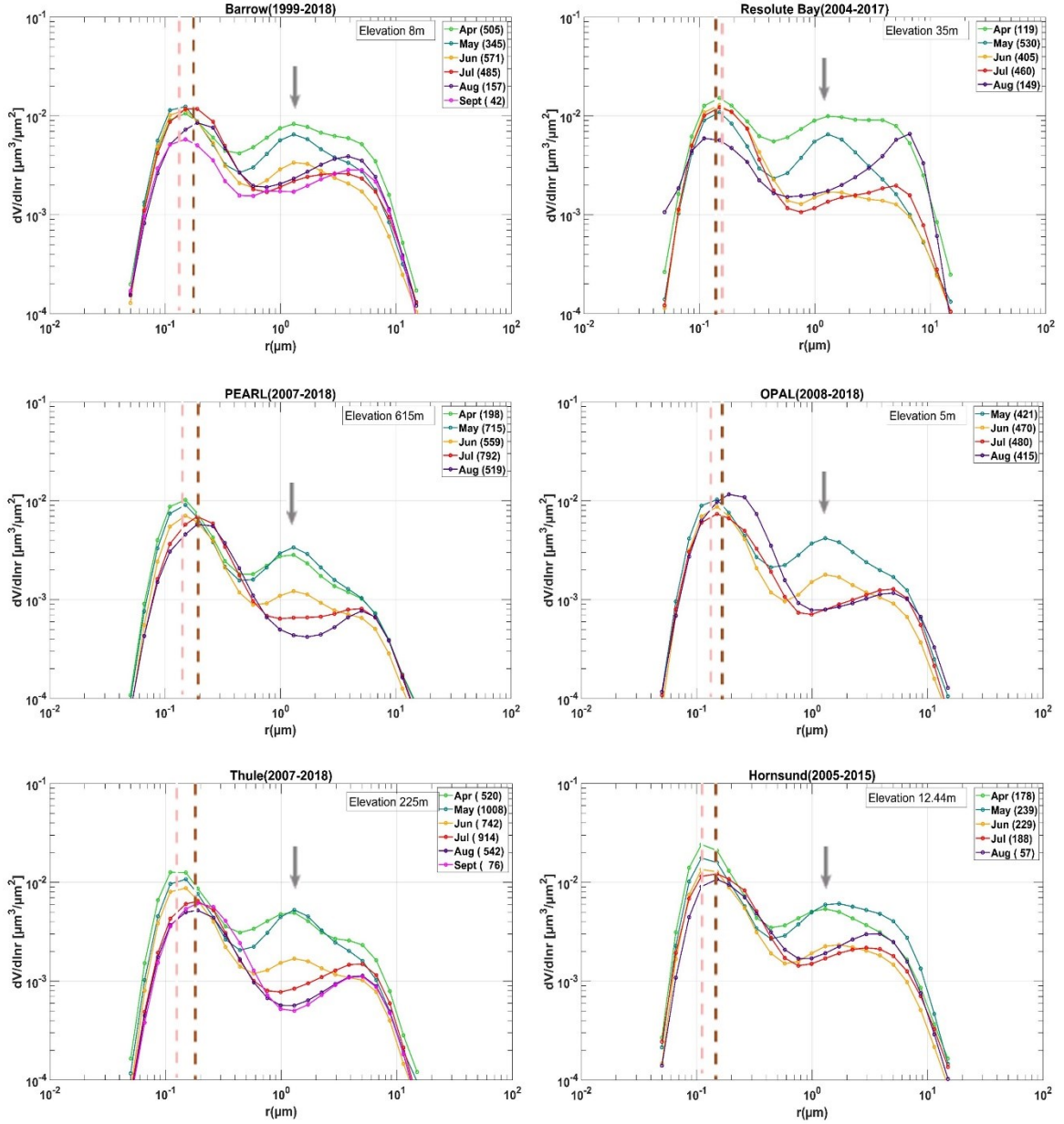


Figure 3 Monthly (arithmetic) averaged volume PSDs across the MYSP for each of the 6 Arctic stations as a function of particle radius (μm). The curves are colored with respect to months; blue/green represents the spring months, orange/red the summer months, and the purple/bright pink curves the fall months. The total number of retrievals for each month over the whole MYSP are indicated in the legend (in parentheses). Both the PSD axes and the radius axes are logarithmic: the left, center and right bin radius coordinates for the 22 PSD bins whose center-point PSD values are seen on each graph are defined in Table S1 in the Supplementary Material. The gray arrows indicate the position of the $1.3 \mu\text{m}$ springtime peak while the dashed vertical lines show the range of movement of the fine mode peak between spring (pink dashed line) and summer (brown line). In two cases (May and June at the western most station of Hornsund) the springtime peak appears at $1.71 \mu\text{m}$.

A more subtle but still robust feature, represented by dashed vertical lines (pink for spring and brown for summer), is the generally increasing size of the FM aerosols from spring to summer : a one-bin increase from 0.15 to $0.19 \mu\text{m}$ for Barrow, OPAL and PEARL, 0.11 to $0.15 \mu\text{m}$ for Hornsund, a two-bin increase for Thule (0.15 to $0.26 \mu\text{m}$) and a one bin decrease for Resolute Bay (0.15 to $0.11 \mu\text{m}$). These changes just exceed the FM peak position retrieval uncertainty of $0.03 \mu\text{m}$

quoted above : our “robust” characterization is more an attribution associated with the common spring to summer peak-position behavior across the Arctic sites. In stark contrast to this result, Croft et al. (2015) observed that $r_{eff,f}$ values derived from surface measurements at Alert (350 km north of Eureka) were $\sim 0.13 \mu\text{m}$ during the Arctic haze springtime period and actually decreased by $\sim 40\%$ during the summer. This apparent incoherency can be hypothesized to be due to the increasing columnar dominance of smoke aerosols relative to Arctic haze as the summer progresses. The latter’s decrease in size and decrease in τ_f accentuates the contribution of what would appear to be larger-sized smoke particles to columnar-averaged $r_{eff,f}$ values and the steady if not increasing contribution of the FM smoke to τ_f (the latter affirmation is generally supported by the FM SO_4 and FM OC AOD simulations of Figure 1).

That the surface measurements are typically not strongly responsive to smoke contributions is likely attributable to the fact that the smoke is typically concentrated in plumes well above the surface. This results from general arguments of the isentropic lift of smoke particles from southern (Boreal forest) fires coupled with a considerable accumulation of smoke plume observations over the Arctic (c.f., e.g., O’Neill et al., 2008 and Saha et al., 2010). To add quantitative support to this qualitative argument, Ranjbar et al. (2019) employed (2005 to 2010) AHSRL (Arctic High Spectral Resolution Lidar) profiles over Eureka and 1 year of KARL (Kodeway Aerosol Raman Lidar) profiles over Ny Alesund to compute optically averaged smoke plume heights that were $\sim 3 \text{ km}$ at both sites.

4.2 AOD and effective radius histograms

Figure 4 shows AOD histograms in log (base 10) space (left-hand graphs) and effective radius histograms in linear space (right-hand graphs) for the entire ensemble of stations and their associated MYSPs (using our standard colors of gray, blue and red for total, CM and FM AOD or effective radius). We also subclassified the histograms into spring (lighter shade) and summer (darker shade) components (represented by stacked histograms and not superimposed histograms). The subclassified histograms display a degree of separability that is coherent with the separability of the different PSD modes discussed in the previous section.

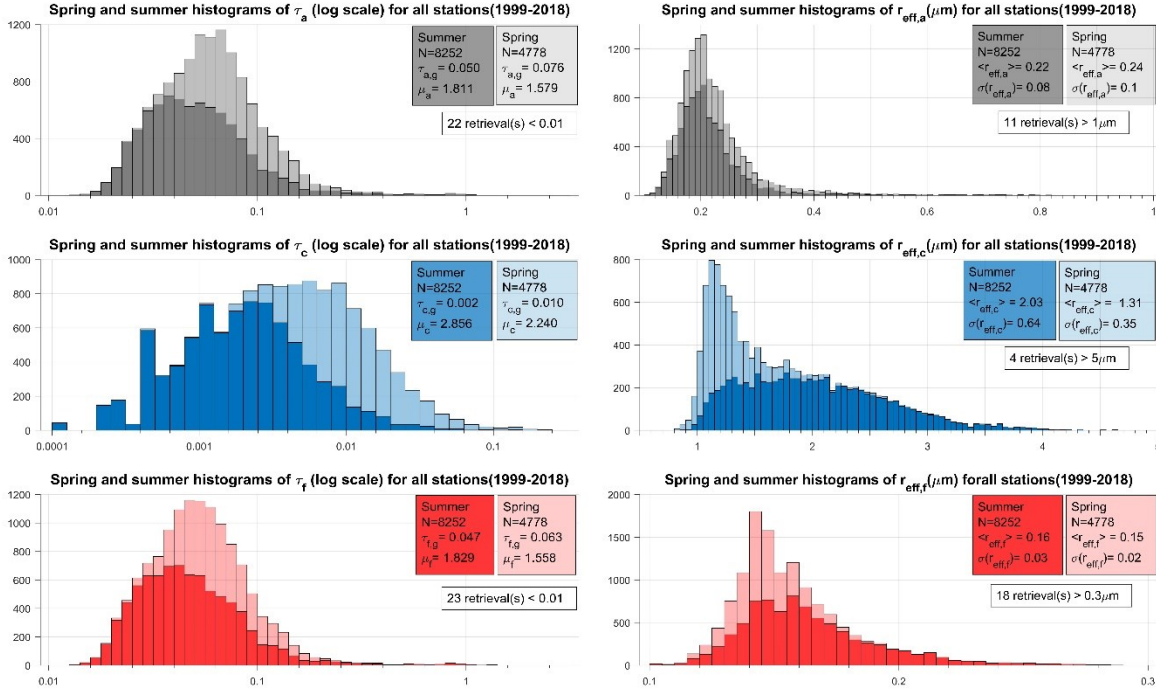


Figure 4 Left-hand graphs - histograms of τ_a , τ_c and τ_f in log (base 10) space for the total data ensemble (all stations encompassed by all their respective MYSPs). Right-hand graphs - linear histograms of $r_{eff,a}$, $r_{eff,c}$, and $r_{eff,f}$ for the same data ensemble as the left-hand graphs. The first, second and third rows show histograms of, respectively; τ_a and $r_{eff,a}$, τ_c and $r_{eff,c}$, and τ_f and $r_{eff,f}$. Light and dark color shades indicate respectively, spring (April and May) and summer (June to September). It is important to note that the spring and summer histograms are stacked and not superimposed histograms. N represents the total number of observations. The average and standard deviation (which in the case of the $\log(\tau_f)$ histogram is $\sigma(\log \tau_f) = \mu_f$) are also listed together with, if any, the number of retrievals that are located beyond or below the chosen x-axis limits. The appropriate fashion for reporting the geometric statistics is $(\log(\tau_x) \pm \sigma(\log \tau_x))$ or hence $\tau_{g,x} \times \mu_x^{\pm 1}$. Site specific figures analogous to this ensemble figure are presented in the supplementary material.

The 1.3- μm , springtime Asian dust mode of Figure 3 can be associated with light blue springtime τ_c histogram (which is complemented by a dark blue histogram of weaker summertime values). The $\tau_{c,g}$ spring to summer decrease from $(\tau_{c,g} \times \mu_c^{\pm 1}) 0.010 \times \div 2.24$ to $0.002 \times \div 2.89$ is at the margins of significance but that marginal significance is systematic across all stations (see the station-by-station histograms Figures S1 to S6 in the supporting information). The springtime $r_{eff,c}$ histogram clearly shows a smaller set of values (relative to the summer histogram), with an arithmetic mean $\langle r_{eff,c} \rangle$ of $1.31 \pm 0.35 \mu m$ (compared with a summertime value of $2.03 \pm 0.64 \mu m$). Accordingly, the above mentioned, relatively large-amplitude springtime peak at 1.3 μm acts to generate a systematically lower value of $\langle r_{eff,c} \rangle$ over the ensemble of stations and their associated MYSPs (that the peak radius and $\langle r_{eff,c} \rangle$ are nearly equal is of no particular significance, since $r_{eff,c}$ is computed over the entire CM range of the PSD).

The interpretation of the spring to summer shift of the FM peak to larger particle sizes in Figure 3 (as the Arctic haze succumbs to a more smoke dominated atmosphere) is more complex

given the opposing spring to summer shifts of the τ_f and $r_{eff,f}$ ensemble histograms of Figure 4. The springtime τ_f amplitudes are moderately large (values of $\tau_{f,g} \times \mu_f^{\pm 1} = 0.063 \times \div 1.56$ versus $0.047 \times \div 1.83$ in the summer) while the systematic, spring to summer (Figure 3) displacement of the FM peak translates into a small $\langle r_{eff,f} \rangle$ increase (0.15 ± 0.02 to $0.16 \pm 0.03 \mu\text{m}$). We also note that the τ_f histogram is characterized by larger summer width (μ_f factors of 1.83 in the summer versus 1.56 in the spring). This latter result is coherent with AOD standard deviation increase reported by Hesaraki et al. (2017) who attributed it to the relatively high variability of FM summertime smoke AODs.

4.3 Robustness of seasonal results

In order to test the robustness of the seasonal MYSP statistics for a given station (monthly binned results that are averaged across the total MYSP to be precise), we performed comparisons between those statistics and the station statistics of a 4-year period (2009-2012). Note that we tested various minimal-data-requirement filters for those monthly results (none of which significantly changed the comparison statistics; for example, the elimination of months that included fewer than 10 retrievals did not significantly change seasonal results). The 2009-2012 versus MYSP comparative results show, as will be appreciated below, that the amplitudes of the all-station $\tau_{f,g}$, $\tau_{c,g}$, $\langle r_{eff,f} \rangle$ and $\langle r_{eff,c} \rangle$ differences (≤ 0.01 , 0.005 , 0.007 , and 0.06 , respectively) are small relative to the standard deviations associated with the natural variation of those parameters.

We found (as did Hesaraki et al., 2017) a notable extreme-event sensitivity that was dependent on the strength of the event and the MYSP. An extreme event (e.g., a τ_f spike over the course of a few hours), can have a significant impact on a given multi-year average. Figure 5a shows seasonal variation of $\langle \tau_a \rangle$ in black (the arithmetic mean being chosen, along with the $\langle \tau_a \rangle$ results in green of Tomasi et al., 2015, to make the link with an analogous set of plots shown in Figure 4 of Hesaraki et al., 2017) and $\langle \tau_f \rangle$ in red. The large, June and July $\sigma(\tau_a)$ error bars for Barrow and Resolute Bay, and OPAL in August are reminiscent of analogous $\sigma(\tau_a)$ behavior that was attributed to the variability of smoke AODs (Hesaraki et al., 2017). This variability inspired us to investigate the impact of removing extreme τ_f values (defined as $\tau_f \geq 0.4$) on the robustness of seasonal means (Figure 5b). The specific value of the threshold was considered of secondary importance since, as will become evident immediately below, our underlying motivation in this section was to investigate

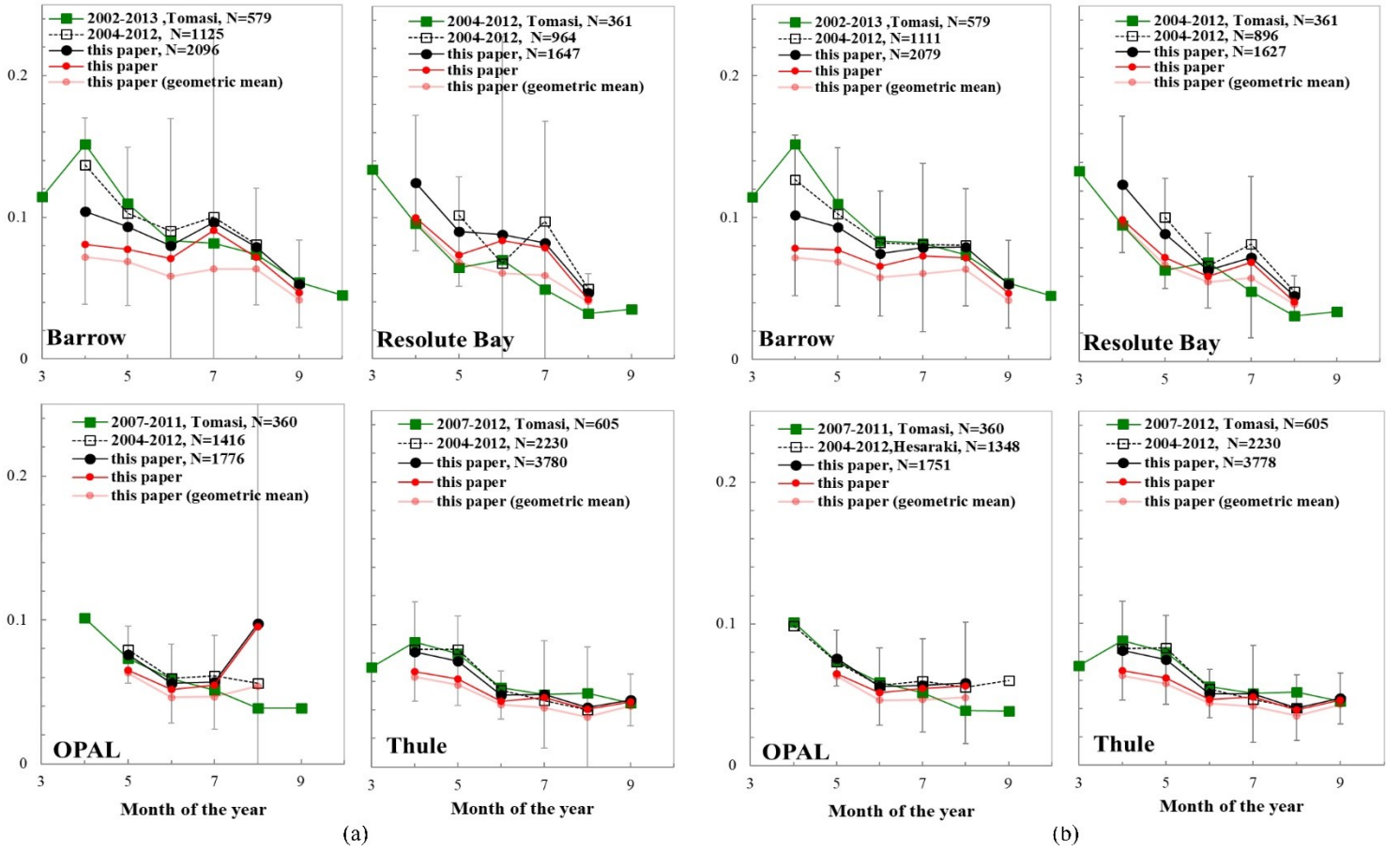


Figure 5(a) $\langle \tau_a \rangle$ comparison between 550 nm, Version 2, Level 2.0 (extinction) AODs of Tomasi et al. (2015), and our 550 nm arithmetic averages as defined in Section 3.2 (green squares and solid black circles respectively). The grey error bars show the $\pm \sigma(\tau_a)$ extension about the black $\langle \tau_a \rangle$ circles while the pink and red curves represent $\langle \tau_f \rangle$ and $\tau_{f,g}$ respectively. All monthly averages, except those of Tomasi, were calculated from individual retrievals (see Sections 3.2 and 3.3 for details on the retrieval processing employed in this study). Tomasi's monthly averages were calculated from daily averaged data. The original climatologically averaged, Tomasi AODs were reported at 500 nm: we employed their climatologically averaged Angstrom exponents to estimate the slightly lower values of climatologically averaged AODs at our wavelength standard of 550 nm (reduction by ~ 0.01). 5(b) shows plots after applying a threshold filter of $\tau_f \geq 0.4$ to remove fine mode events.

the impact of extreme events with an eventual focus on the robustness of geometric statistics. The extreme τ_f values were typically high frequency excursions of 1 to 3 days duration (the most extreme of which was the Eureka, August 2017 event with τ_f spiking to values of 1.6 as per Ranjbar et al., 2019). The results of Figure 5b show a significant $\sigma(\tau_a)$ reduction. At the same time, we note that $\tau_{f,g}$ values (pink circles) show relatively little sensitivity to the presence or absence of the extreme smoke events. This relative insensitivity is coherent with general knowledge on the damping behavior of geometric means versus arithmetic means in the presence of outliers and strengthens our confidence in the appropriateness of employing geometric means when analyzing long-term AOD trends.

4.4 Seasonal statistics of FM and CM AOD, FMF, and effective radii

In this section, we investigate the seasonal variation of the monthly binned, geometric means and geometric standard deviations of FM and CM AODs, the arithmetic means and standard deviations of FM and CM effective radii and the FMF for the total MYSP of each station. Our goal here is twofold: to better understand the seasonal behavior of these key parameters and to provide an optophysical link to the PSD and histogram discussions presented in the previous two sections.

4.4.1 FM AOD

Figure 6 shows the seasonal variation of $\tau_{f,g}$ (red geometric mean curves and pink, geometric standard deviation envelopes about the red curves) for each of the six stations across their individual MYSPs (c.f. Table 1). In general, an argument for a significant spring to summer decreasing trend is marginal at some stations (Barrow, Resolute Bay and Thule) and virtually non-existent for the other stations (the changes in $\tau_{f,g}$ are relatively small compared to the pink geometric standard deviation envelopes). However, even in the case of Barrow and Resolute Bay, the trends are likely sensitive to issues of non representivity associated, respectively, with the relatively sparsely populated or “low-N” months of September and August and with the month of April at Resolute Bay. The decreasing trend is strongest for Thule if one discounts the low-N month of September. In fact, Thule is the greatest influence on the decreasing ensemble trend noted in the discussion of Figure 4 (the decrease of $\tau_{f,g}$ from 0.063 to 0.047). The variation of the amplitudes of the pink envelopes are in keeping with the discussion above concerning the larger summertime ensemble values of the τ_f histogram width.

4.4.2 CM AOD

In agreement with the light- and dark blue-shaded τ_c histograms of Figure 4, we found that $\tau_{c,g}$ goes through a significant decrease during the spring to summer transition and that this decrease was largely the result of the decrease in amplitude of the 1.3- μm PSD peak of Figure 3. This is, again, a result that has a continent-wide context with the same type of trend being observed for all southern stations (with the exception of Sable Island). We would also point out that the robustness of this general behavior is notable since the peak $\tau_{c,g}$ value of ~ 0.01 in Figure 7 is \sim the typical uncertainty associated with CIMEL field instruments (0.01– 0.02 as per Eck et al., 2009). As per Hesaraki et al., (2017), we attributed this decrease to the decreasing influence of Asian dust. The

$\tau_{c,g}$ amplitudes are also seen to be larger for Barrow and Resolute Bay (as was noted above for the amplitudes of the 1.3 μm CM peak).

Barrow, Resolute Bay, and Hornsund show a spring to summer $\tau_{c,g}$ decay, which is less rapid than the other sites (with attendant larger $\tau_{c,g}$ values in July and August but with only Resolute Bay showing any kind of increase in going from July to August). This is qualitatively coherent with the arguments above concerning a summertime July to August (5-7 μm) PSD-peak increase that was speculated to be due to wind-induced sea salt aerosols at those same three stations. However, further investigations into the correlative links between local wind speeds and retrieved values of τ_c would be necessary to better characterize those links.

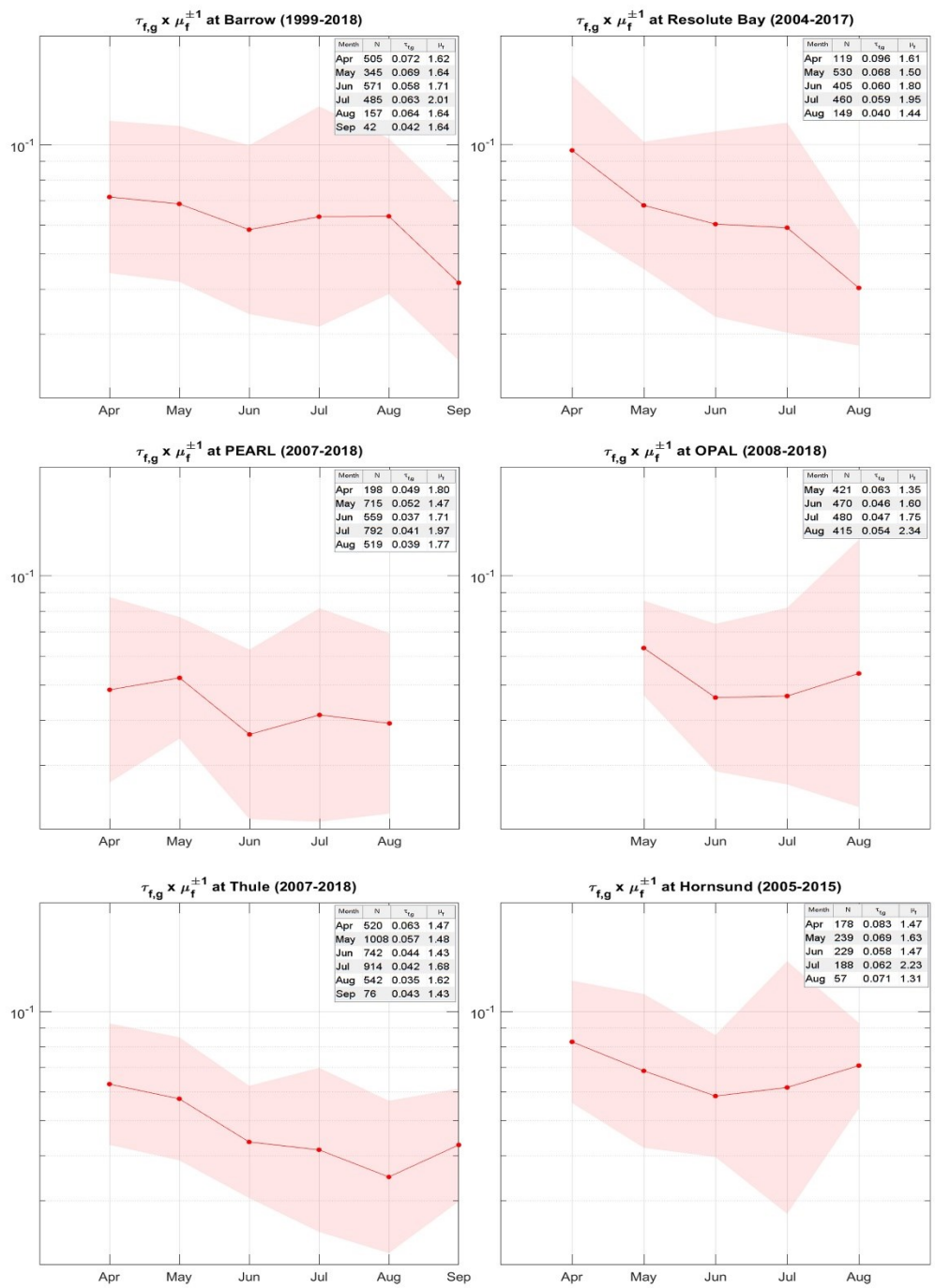


Figure 6 Seasonal τ_f variation for all 6 stations. The plots show the month to month variation of $\tau_{f,g}$ (monthly binned geometric averages) across the MYSP of each station (MYSPs are defined in Table 1). The shading represents the extent of the geometric mean ($\tau_{f,g} \times \mu_f^{\pm 1}$ about $\tau_{f,g}$). "N" represents the number of retrievals over the total MYSP.

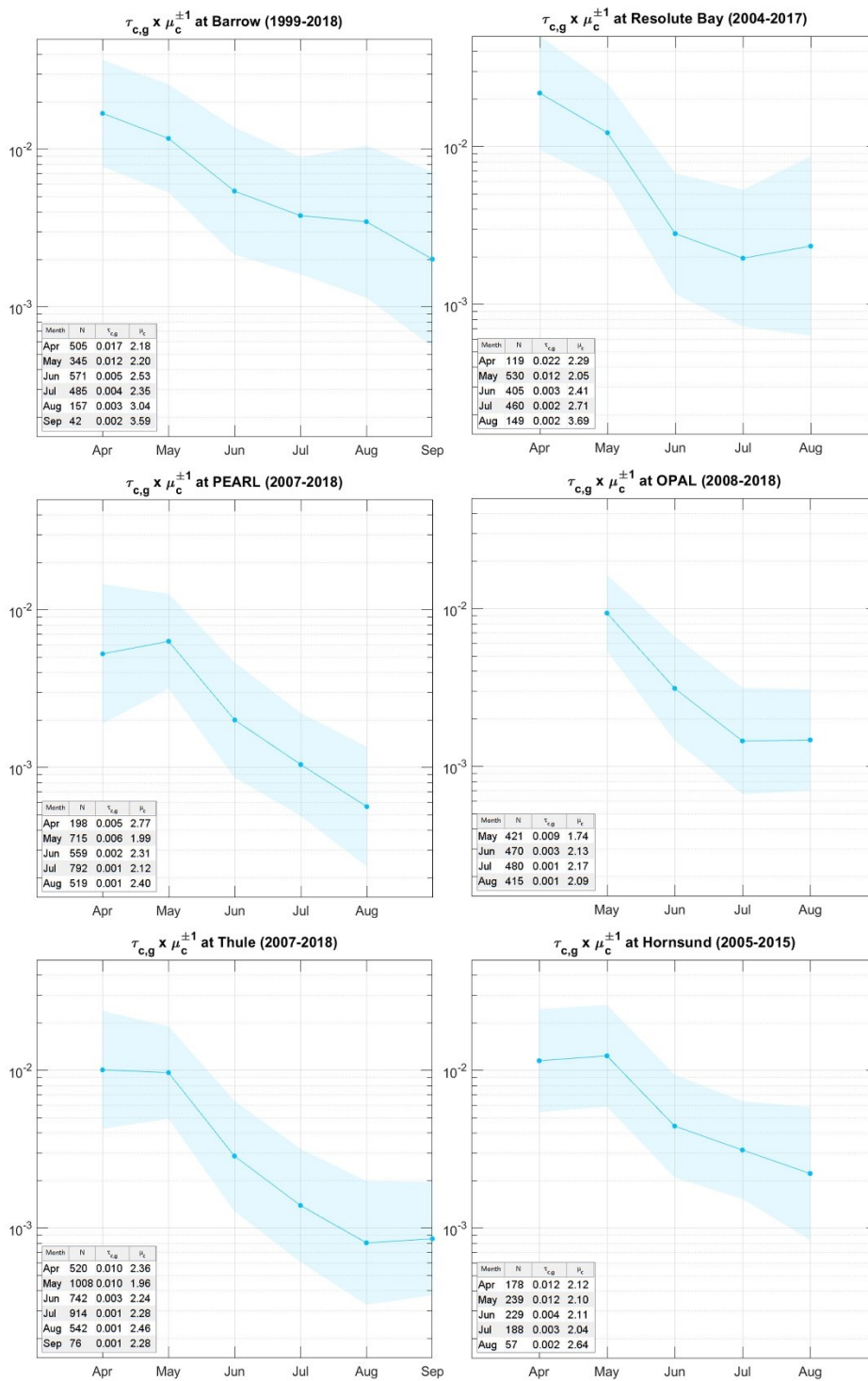


Figure 7 Seasonal τ_c variation for all 6 stations. Same caption as Figure 5 (with “c” replacing “f”).

4.4.3 Fine mode fraction

The previous results showed that the change in $\tau_{f,g}$ tends to be insignificant (roughly flat) during the spring to summer transition period over half the stations (while the western stations and Thule, whose spring to summer decrease appears to be at least marginally significant, are likely sensitive to low retrieval numbers in the early spring and late summer). As noted above, the $\tau_{c,g}$ values appear to show a systematic decrease but with amplitudes that are at the margins of nominal instrument uncertainty. The results of Figure 8 largely indicate a spring to summer increase in $\langle FMF \rangle$: this means that, because τ_f variation is roughly flat or decreasing, the small amplitude τ_c decrease is the driver of the $\langle FMF \rangle$ increase (put another way, the spring to summer reduction in Asian dust is largely responsible for the attendant increase in FMF).

4.4.4 FM effective radius

While the systematic spring to summer transitional shift shown in the Figure 3 PSDs (for all stations except Resolute Bay) was only marginally evident in the ensemble histograms of Figure 4 ($\langle r_{eff,f} \rangle$ increase of $0.01 \mu\text{m}$ from 0.15 ± 0.02 to $0.16 \pm 0.03 \mu\text{m}$), the Figure 9 $\langle r_{eff,f} \rangle$ values of each station (again, except for Resolute Bay) also show a systematic, if marginally significant, spring to summer increase of $\sim 0.02 \mu\text{m}$ (roughly between a spring maximum of $0.15 \mu\text{m}$ and a summer minimum $0.17 \mu\text{m}$, excluding the low-N month of September for Barrow and Thule). As pointed out above, the increase in $\langle r_{eff,f} \rangle$ is likely associated with the increasing influence of FM smoke particles from biomass burning fires in the south and the decreasing influence of FM Arctic haze particles.

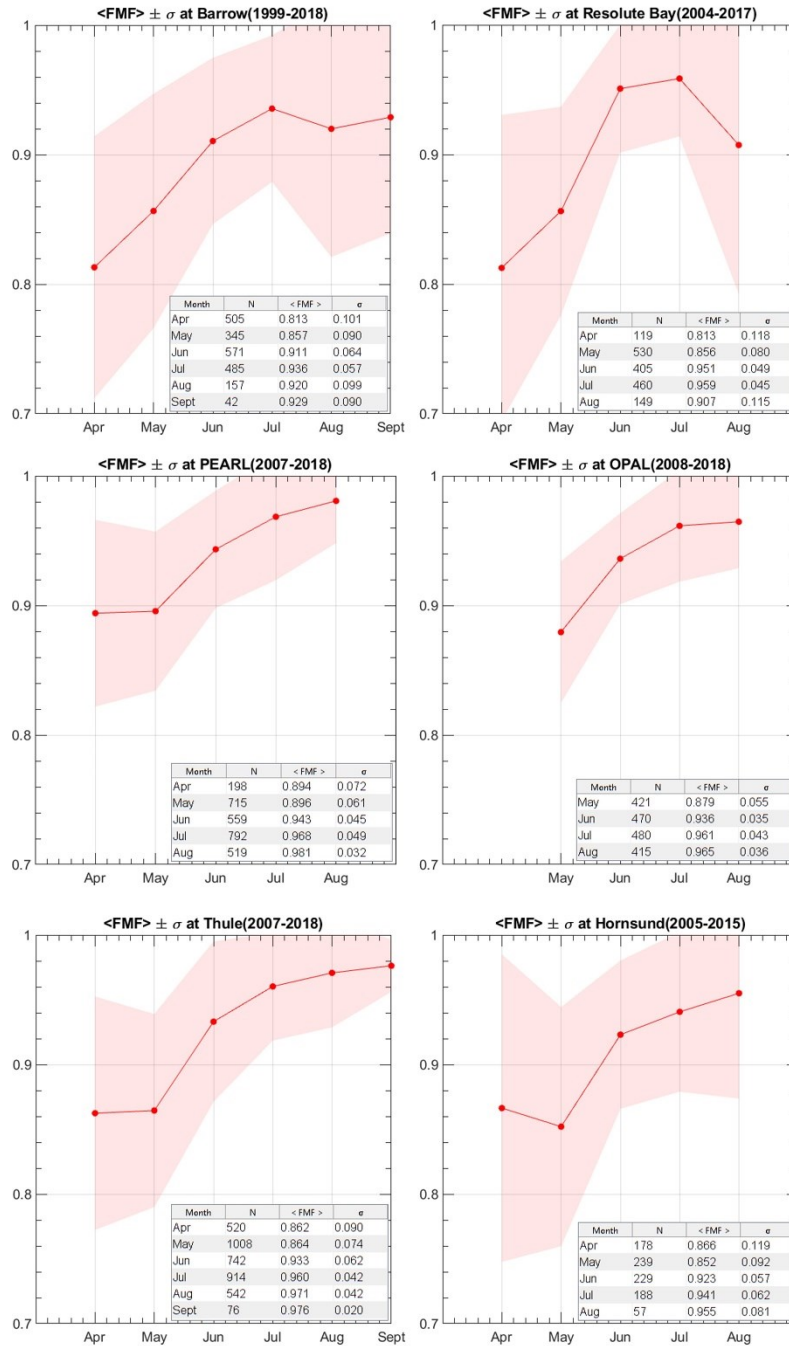


Figure 8 Seasonal variation of the fine mode fraction (FMF). Same caption as Figure 6 (with appropriate changes made for the arithmetic means and standard deviations of the FMF).

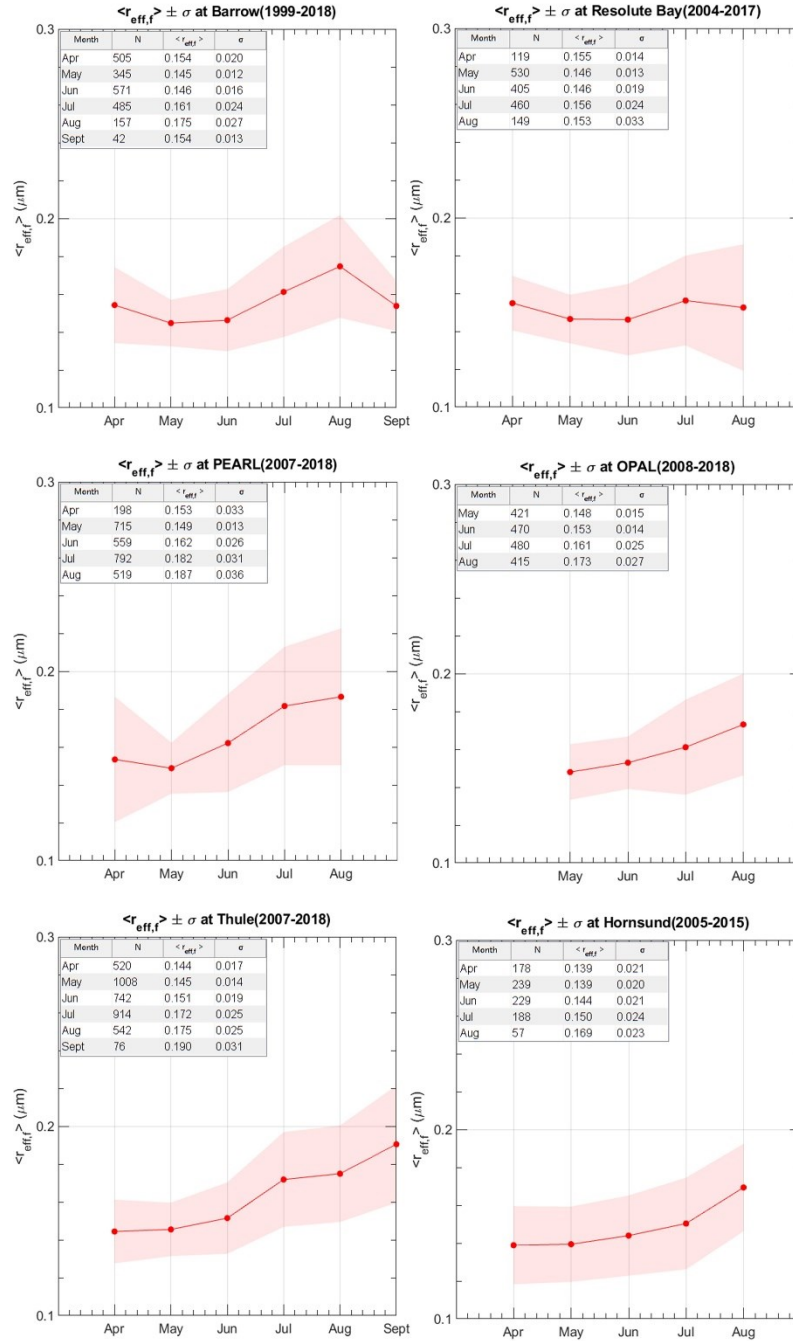


Figure 9 Seasonal $\langle r_{eff,f} \rangle$ variation for all 6 stations. Same caption as Figure 6 (with appropriate changes made for the arithmetic means and standard deviations of $r_{eff,f}$).

4.4.5 CM effective radius

Figure 10 shows that the spring to summer transition results in a largely significant $r_{eff,c}$ increase for all stations. This result is clearly subject to the same type of dynamic as Figure 7: the decreasing influence of the 1.3- μm PSD peak of Figure 3 and the attendant increasing influence

of the larger-radius (5-7 μm) peak. In this case, however, there is no evidence of significantly different $\langle r_{eff,c} \rangle$ values at the coastal sites of Barrow, Resolute Bay and Hornsund relative to the other sites in July and August. We attribute this to the general insensitivity of $\langle r_{eff,c} \rangle$ to the weak differences in the (5-7 μm) PSD peak positions seen in Figure 3 coupled with the relatively weak positive bias of the coastal $\tau_{c,g}$ values relative to the other sites during those 2 months.

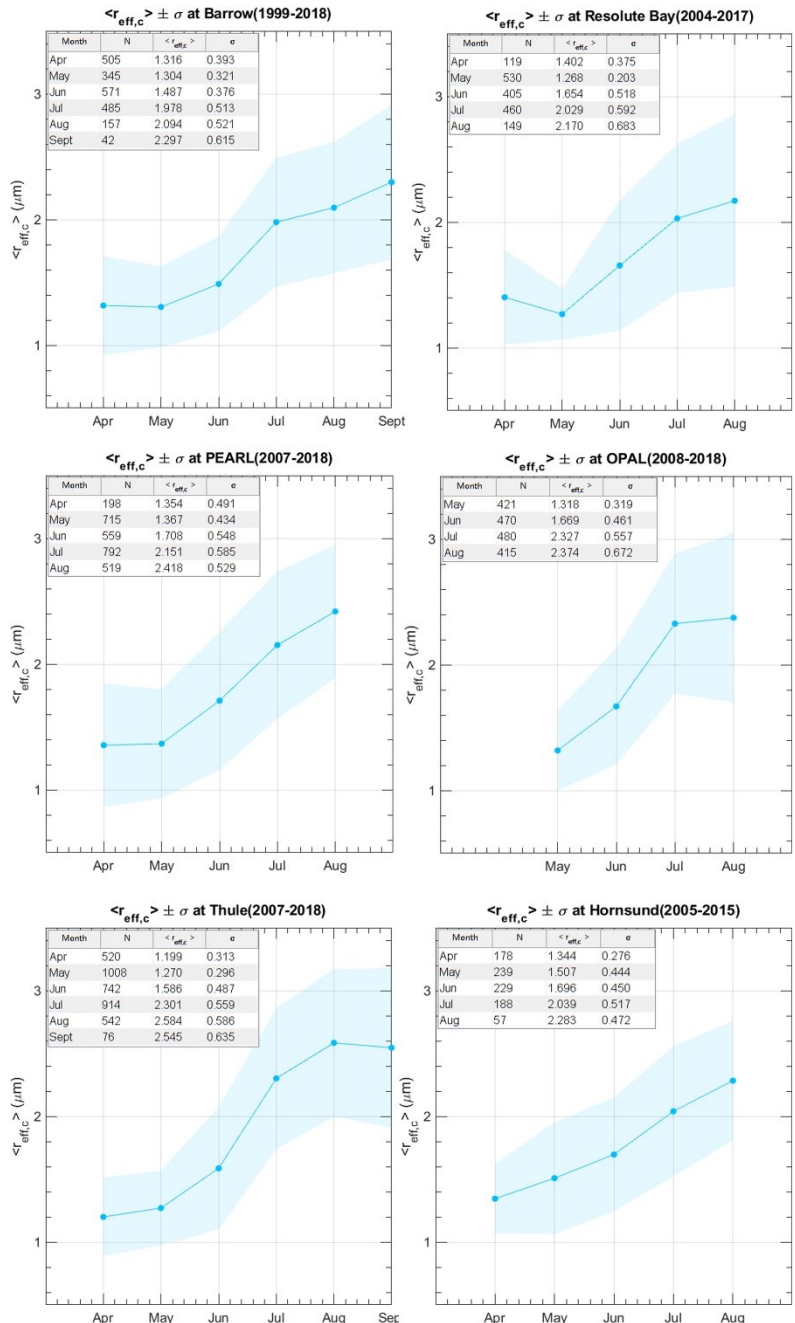


Figure 10 Seasonal $\langle r_{eff,c} \rangle$ variation for all 6 stations. Same caption as Figure 6 (with appropriate changes made for the arithmetic means and standard deviations of $r_{eff,c}$).

5 Conclusion

We investigated the climatological-scale variation of the Dubovik retrieval products from six AERONET stations in the North American and European Arctic. Monthly binned averages for aerosol microphysical and optical properties across MYSPs ranging from 8 to 17 years were analyzed. Distinct spring to summer trends, indicative of robust, Pan-Arctic phenomena, were observed over all these stations (where “Pan-Arctic” is limited to the North American and European Arctic).

The monthly averaged PSDs, with the exception of Resolute Bay, showed a moderate but robust spring to summer increase of one to two bins in the position of the FM PSD peak (the majority of stations showed a one bin increase from the $0.11 \mu\text{m}$ to the $0.15 \mu\text{m}$ bin). The opposing spring to summer tendencies of $\tau_{f,g}$ and $\langle r_{eff,f} \rangle$ for the retrieval ensemble (all-stations and all MYSPs) translated into a moderate decrease in the former and a small increase in the latter (both at the margins of significance). Seasonal $\langle r_{eff,f} \rangle$ plots for each station indicated that the ensemble trend was largely associated with similar trends at each station (again with the exception of Resolute Bay). The seasonal $\tau_{f,g}$ trends for each station varied from insignificant to a substantial decrease at Thule. Both spring to summer trends (the increase in $\langle r_{eff,f} \rangle$ and the negligible to substantial decrease in $\tau_{f,g}$), were interpreted as a tradeoff between the increasing $\tau_{f,smoke}$ influence of larger-sized smoke particles and the waning $\tau_{f,haze}$ influence of smaller-sized Arctic haze aerosols.

We observed a robust, pan-Arctic springtime PSD peak in the $1.3 \mu\text{m}$ bin at all six Arctic stations (a continent-scale phenomenon for which the same type of peak was observed at three southern stations) with the amplitude of that peak being larger for the western Arctic stations of Barrow and Resolute Bay. The MYSP-averaged $\tau_{c,g}$ spring to summer decrease was at the margins of significance but that marginal significance was systematic across individual stations. It was suggested that a July to August PSD-peak increase for the low-elevation coastal sites (Barrow, Resolute Bay and Hornsund) was due to wind-spray-induced sea-salt possibly tempered by larger local dust particles (a finding whose $\tau_{c,g}$ influence appeared to be a lesser rate of spring to summer $\tau_{c,g}$ decrease). We found that $\tau_{c,g}$ goes through a significant decrease (both for the ensemble and individual station retrievals) during the spring to summer transition and that this decrease was largely the result of the decrease in amplitude of the springtime $1.3 \mu\text{m}$ PSD peak. The spring to summer transition results in a largely significant $\langle r_{eff,c} \rangle$ increase for all stations. This is simply the result of

a decreasing influence of the 1.3- μm PSD peak and the attendant increasing influence of the larger-radius (5 - 7 μm) peak. Spring to summer $\langle FMF \rangle$ increases were attributed to the relatively stable or even increasing values of $\tau_{f,g}$ in the presence of a decreasing $\tau_{c,g}$ trend associated with the decrease in springtime Asian dust.

Our robustness analysis included an AOD sensitivity study where we compared our MYSP statistics with those of a shorter 4-year MYSP, comparisons with previous AOD seasonal climatologies as well as an attempt to demonstrate the climatological-scale impact of extreme events. The single most determining factor in degrading the robustness (precision) of the (arithmetic mean) seasonal results was the presence of extreme FM events (defined as $\tau_f \geq 0.4$). Geometric means (versus arithmetic means) were, not surprisingly, found to represent more robust indicators of climatological-scale tendencies.

Appendix A: Symbol and acronym glossary

AEROCAN	Federated Canadian subnetwork of AERONET run by Environment and Climate Change Canada (ECCC)
AERONET	Aerosol Robotic Network: World-wide NASA network of combined sunphotometer / sky-scanning radiometers manufactured by CIMEL Électronique. See http://aeronet.gsfc.nasa.gov/ for documentation and data downloads
AHSRL	Arctic High Spectral Resolution Lidar
AOD	Aerosol optical depth: The community uses "AOD" to represent anything from nominal aerosol optical depth which hasn't been cloud-screened to the conceptual (theoretical) interpretation of aerosol optical depth. In this paper we use it in the latter sense and apply adjectives as required.
CCAR	Climate Change and Atmospheric Research
CM	coarse mode (supermicron particle radius)
ECCC	Environment and Climate Change Canada
FM	fine mode (submicron particle radius)
FMF	fine mode fraction
GHG	Greenhouse gas
MYSP	Multi-year sampling Period (different for each station) for which we acquired AERONET/Dubovik retrieval products.
NASA	National Aeronautics and Space Administration
NETCARE	Network on Climate and Aerosols: Addressing key uncertainties in Remote Canadian Environments
NSERC	Natural Sciences and Engineering Research Council of Canada
KARL	Kodeway Aerosol Raman Lidar
OPAL	Zero elevation Polar Atmospheric Lab
PEARL	Polar Environmental Atmospheric Research Laboratory
PSD	particle size distribution (precisely, the volume particle size distribution)

x	x = a, f, or c (total, fine mode or coarse mode)
$\langle \tau_x \rangle$	Arithmetic mean of AOD for monthly averaging bins
$\langle r_{eff,x} \rangle$	Arithmetic mean of the effective radii for monthly averaging bins
$\sigma(\tau_x)$	Arithmetic standard deviation for monthly averaging bins for AODs
$\sigma(r_{eff,x})$	Arithmetic standard deviation for monthly averaging bins for effective radii
$\tau_{x,g}$	Geometric mean for monthly averaging bins. $\tau_{x,g} = 10^{\langle \log \tau_x \rangle}$ (see Table 1 of O'Neill et al., 2000).
μ_x	Geometric standard deviation for monthly averaging bins. $\mu_x = 10^{\sigma(\log \tau_x)}$ (see Table 1 of O'Neill et al., 2000).

Acknowledgments and Data

We would like to acknowledge our gratitude to NSERC for CCAR funding via the NETCARE and PAHA projects as well as NSERC DG funding of O'Neill. The support of AEROCAN (Environment Change and Climate Change Canada), AERONET (NASA/GSFC), and the operation staff at the six sites whose retrievals we employed are gratefully acknowledged. We thank the PIs for their effort in establishing and maintaining the sites: Brent Holben for Thule and Hornsund, Grzegorz Karasinski and Piotr Glowacki for Hornsund, and Rick Wagener, Laurie Gregory and Lynn Ma for Barrow, and Vitali Fioletov for Resolute Bay, Eureka, Ebgert, Saturna and Sable Island. Finally, special thanks to Charlotte Crevier (undergraduate summer intern-2017- at the Université de Sherbrooke), for her significant programming help. Data used in this study is available at the AERONET website. The following is the main page with the list of all stations: https://aeronet.gsfc.nasa.gov/cgi-bin/webtool_inv_v3. In our study, we utilized 'All Points' of Level 1.5 (All products except the phase function and U27).

References

- Abbatt, J. P. D., Leaitch, W. R., Aliabadi, A. A., Bertram, A. K., Boivin-rioux, A., Bozem, H., et al. (2018). New insights into aerosol and climate in the Arctic, (October), 1–60.
- AboEl-Fetouh, Y., O'Neill, N. T., Ranjbar, K., Hesarakı, S., Abboud, I., & Sobolewski, P. S. (2020). Climatological-Scale Analysis of Intensive and Semi-intensive Aerosol Parameters Derived From AERONET Retrievals Over the Arctic. *Journal of Geophysical Research: Atmospheres*, 125(10), 1–19. <https://doi.org/10.1029/2019JD031569>
- Adams, P. J., & Seinfeld, J. H. (2002). Predicting global aerosol size distributions in general circulation models. *Journal of Geophysical Research Atmospheres*, 107(19), 1–23. <https://doi.org/10.1029/2001JD001010>
- AMAP. (2017). *Snow, Water, Ice and Permafrost. Summary for Policy-makers. Arctic Monitoring and Assessment Programme (AMAP)*. Oslo, Norway. <https://doi.org/10.1029/2002WR001512>
- AMAP. (2021). Arctic Climate Change Update 2021: Key Trends and Impacts. Summary for Policy-makers. *Arctic Monitoring and Assessment Programme (AMAP)*. Tromsø, Norway: Arctic Monitoring and Assessment Programme (AMAP).

- Anderson, T. L., Wu, Y., Chu, D. A., Schmid, B., Redemann, J., & Dubovik, O. (2005). Testing the MODIS satellite retrieval of aerosol fine-mode fraction. *J. Geophys. Res.*, *110*(March), D18204. <https://doi.org/10.1029/2005JD005978>
- Bergstrom, R. W., Pilewskie, P., Russell, P. B., Redemann, J., Bond, T. C., Quinn, P. K., & Sierau, B. (2007). Spectral absorption properties of atmospheric aerosols. *Atmospheric Chemistry and Physics*, *7*, 5937–5943. <https://doi.org/10.5194/acp-7-5937-2007>
- Bey, I., Jacob, D. J., Yantosca, R. M., Logan, J. A., Field, B. D., Fiore, A. M., et al. (2001). Global modeling of tropospheric chemistry with assimilated meteorology: Model description and evaluation. *Journal of Geophysical Research Atmospheres*, *106*(D19), 23073–23095. <https://doi.org/10.1029/2001JD000807>
- Bohren, C. F., & Huffman, D. R. (2004). *Absorption and Scattering of Light by Small Particles* (First publ). Weinheim: WILEY-VCH Verlag GmbH & Co. KGaA. <https://doi.org/10.1002/9783527618156>
- Bond, T. C., & Bergstrom, R. W. (2006). Aerosol Science and Technology Light Absorption by Carbonaceous Particles: An Investigative Review Light Absorption by Carbonaceous Particles: An Investigative Review. *Aerosol Science and Technology*, *40*(1), 27–67. <https://doi.org/10.1080/02786820500421521>
- Boucher, O., Randall, D., Artaxo, P., Bretherton, C., Feingold, G., Forster, P., et al. (2013a). *Clouds and Aerosols. In: Climate Change 2013: The Physical Science Basis. Contribution of Working Group I to the Fifth Assessment Report of the Intergovernmental Panel on Climate Change [Stocker, T.F., D. Qin, G.-K. Plattner, M. Tignor, S.K. Allen, J. Bos. Cambridge University Press, Cambridge, United Kingdom and New York, NY, USA. Retrieved from https://www.ipcc.ch/pdf/assessment-report/ar5/wg1/WG1AR5_Chapter07_FINAL.pdf*
- Boucher, O., Randall, D., Artaxo, P., Bretherton, C., Feingold, G., Forster, P., et al. (2013b). Clouds and aerosols. In T. F. Stocker, D. Qin, G.-K. Plattner, M. Tignor, S. K. Allen, J. Boschung, et al. (Eds.), *Climate Change 2013 the Physical Science Basis: Working Group I Contribution to the Fifth Assessment Report of the Intergovernmental Panel on Climate Change* (Vol. 9781107057, pp. 571–658). Cambridge, United Kingdom and New York, NY, USA: Cambridge University Press. <https://doi.org/10.1017/CBO9781107415324.016>
- Boucher, Olivier. (2015). *Atmospheric Aerosols: Properties and Climate Impacts*. Springer Netherlands. <https://doi.org/10.1007/978-94-017-9649-1>
- Breider, T. J., Mickley, L. J., Jacob, D. J., Wang, Q., Fisher, J. a., Chang, R. Y.-W., & Alexander, B. (2014). Annual distributions and sources of Arctic aerosol components, aerosol optical depth, and aerosol absorption. *Journal of Geophysical Research: Atmospheres*, *119*(7), 4107–4124. <https://doi.org/10.1002/2013JD020996>
- Bullard, J. E., Matthew, B., Tom, B., John, C., Eleanor, D., Diego, G., et al. (2016). High latitude dust in the Earth system. *Reviews of Geophysics*, *54*, 447–485. <https://doi.org/10.1002/2016RG000518>.Received
- Chin, M., Diehl, T., Tan, Q., Prospero, J. M., Kahn, R. A., Remer, L. A., et al. (2019). Multi-decadal aerosol variations from 1980 to 2009 : a perspective from observations and a global model, 3657–3690. <https://doi.org/10.5194/acp-14-3657-2014>
- Croft, B., Wentworth, G. R., Martin, R. V., Leaitch, W. R., Murphy, J. G., Murphy, B. N., et al.

- (2016). Contribution of Arctic seabird-colony ammonia to atmospheric particles and cloud-albedo radiative effect. *Nature Communications*, 7, 1–10. <https://doi.org/10.1038/ncomms13444>
- Croft, Betty, Martin, R. V., Leaitch, W. R., Tunved, P., Breider, T. J., D'andrea, S. D., & Pierce, J. R. (2016). Processes controlling the annual cycle of Arctic aerosol number and size distributions. *Atmos. Chem. Phys*, 16, 3665–3682. <https://doi.org/10.5194/acp-16-3665-2016>
- Croft, Betty, Martin, R. V., Richard Leaitch, W., Burkart, J., Chang, R. Y. W., Collins, D. B., et al. (2019). Arctic marine secondary organic aerosol contributes significantly to summertime particle size distributions in the Canadian Arctic Archipelago. *Atmospheric Chemistry and Physics*, 19(5), 2787–2812. <https://doi.org/10.5194/acp-19-2787-2019>
- Curci, G., Hogrefe, C., Bianconi, R., Im, U., Balzarini, A., Baró, R., et al. (2015). Uncertainties of simulated aerosol optical properties induced by assumptions on aerosol physical and chemical properties: An AQMEII-2 perspective. *Atmospheric Environment*, 115, 541–552. <https://doi.org/10.1016/j.atmosenv.2014.09.009>
- Dick, W. D., Saxena, P., & McMurry, P. H. (2000). Estimation of water uptake by organic compounds in submicron aerosols measured during the Southeastern Aerosol and Visibility Study. *Journal of Geophysical Research*, 105(D1), 1471–1479. <https://doi.org/10.1029/1999JD901001>
- Dubovik, O., & King, M. D. (2000). A flexible inversion algorithm for retrieval of aerosol optical properties from Sun and sky radiance measurements. *Journal of Geophysical Research: Atmospheres*, 105(D16), 20673–20696. <https://doi.org/10.1029/2000JD900282>
- Dubovik, O., Holben, B., Eck, T. F., Smirnov, A., Kaufman, Y. J., King, M. D., et al. (2002). Variability of Absorption and Optical Properties of Key Aerosol Types Observed in Worldwide Locations. *Journal of the Atmospheric Sciences*, 59(3), 590–608. [https://doi.org/10.1175/1520-0469\(2002\)059<0590:VOAAOP>2.0.CO;2](https://doi.org/10.1175/1520-0469(2002)059<0590:VOAAOP>2.0.CO;2)
- Eck, T. F., Holben, B. N., Reid, J. S., Sinyuk, a., Hyer, E. J., O'Neill, N. T., et al. (2009). Optical properties of boreal region biomass burning aerosols in central Alaska and seasonal variation of aerosol optical depth at an Arctic coastal site. *Journal of Geophysical Research: Atmospheres*, 114(11), 1–14. <https://doi.org/10.1029/2008JD010870>
- Gelaro, R., McCarty, W., Suárez, M. J., Todling, R., Molod, A., Takacs, L., et al. (2017). The modern-era retrospective analysis for research and applications, version 2 (MERRA-2). *Journal of Climate*, 30(14), 5419–5454. <https://doi.org/10.1175/JCLI-D-16-0758.1>
- Gong, S. L. (2003). A parameterization of sea-salt aerosol source function for sub- and super-micron particles, 17(4), 1–7. <https://doi.org/10.1029/2003GB002079>
- Groot Zwaafink, C. D., Grythe, H., Skov, H., & Stohl, A. (2016). Substantial contribution of northern high-latitude sources to mineral dust in the Arctic. *Journal of Geophysical Research*, 121(22), 13,678–13,697. <https://doi.org/10.1002/2016JD025482>
- Hansen, James E. and Travis, L. D. (1974). Light Scattering in Planetary Atmospheres. *Space Science Reviews*, 16, 527–610. <https://doi.org/10.1007/BF00168069>
- Hesaraki, S., Neill, N. T. O., Lesins, G., Saha, A., Randall, V., Fioletov, V. E., et al. (2017). Comparisons of a Chemical Transport Model with a Four-Year (April to September)

- Analysis of Fine- and Coarse-Mode Aerosol Optical Depth Retrievals Over the Canadian Arctic. *Atmosphere-Ocean*, 55(4–5), 213–229.
<https://doi.org/10.1080/07055900.2017.1356263>
- Hesarakis, S., O’Neill, N. T., Lesins, G., Saha, A., Randall, M., Fioletov, V. E., et al. (2017). Polar summer comparisons of a chemical transport model with a 4-year analysis of fine and coarse mode aerosol optical depth retrievals over the Canadian Arctic, (In press).
- Hinds, W. C. (1999). *Aerosol Technology: Properties, Behavior, and Measurement of Airborne Particles* (2nd Editio). John Wiley & Sons, Inc.
- Hirdman, D., Burkhardt, J. F., Sodemann, H., Eckhardt, S., Jefferson, A., Quinn, P. K., et al. (2010). Long-term trends of black carbon and sulphate aerosol in the Arctic: Changes in atmospheric transport and source region emissions. *Atmospheric Chemistry and Physics*, 10(19), 9351–9368. <https://doi.org/10.5194/acp-10-9351-2010>
- Holben, B. N., Eck, T. F., Slutsker, I., Tanré, D., Buis, J. P., Setzer, a., et al. (1998). AERONET - A federated instrument network and data archive for aerosol characterization. *Remote Sensing of Environment*, 66(1), 1–16. [https://doi.org/10.1016/S0034-4257\(98\)00031-5](https://doi.org/10.1016/S0034-4257(98)00031-5)
- Huang, J., & Jaeglé, L. (2017). Wintertime enhancements of sea salt aerosol in polar regions consistent with a sea ice source from blowing snow. *Atmospheric Chemistry and Physics*, 17(5), 3699–3712. <https://doi.org/10.5194/acp-17-3699-2017>
- IPCC. (2021). Summary for Policymakers. In: Climate Change 2021: The Physical Science Basis. Contribution of Working Group I to the Sixth Assessment Report of the Intergovernmental Panel on Climate Change. In V. Masson-Delmotte, P. Zhai, A. Pirani, S. L. Connors, C. Pean, S. Berger, et al. (Eds.). Cambridge University Press. In Press.
<https://doi.org/10.1080/03736245.2010.480842>
- Kodros, J. K., & Pierce, J. R. (2017). Important global and regional differences in aerosol cloud-albedo effect estimates between simulations with and without prognostic aerosol microphysics. *Journal of Geophysical Research: Atmospheres*, 122(7), 4003–4018.
<https://doi.org/10.1002/2016JD025886>
- Kodros, J. K., Hanna, S. J., Bertram, A. K., Leaitch, W. R., Schulz, H., Herber, A. B., et al. (2018). Size-resolved mixing state of black carbon in the Canadian high Arctic and implications for simulated direct radiative effect. *Atmospheric Chemistry and Physics*, 18(15), 11345–11361.
<https://doi.org/10.5194/acp-18-11345-2018>
- Law, K. S., & Stohl, a. (2007). Arctic Air Pollution: Origins and Impacts. *Science*, 315(5818), 1537–1540. <https://doi.org/10.1126/science.1137695>
- Leaitch, R. R., Kodros, J. K., Willis, M. D., Hanna, S., Schulz, H., Andrews, E., et al. (2020). Vertical profiles of light absorption and scattering associated with black carbon particle fractions in the springtime Arctic above 79°N. *Atmospheric Chemistry and Physics*, 20(17), 10545–10563. <https://doi.org/10.5194/acp-20-10545-2020>
- Lesins, G., Chylek, P., & Lohmann, U. (2002). A study of internal and external mixing scenarios and its effect on aerosol optical properties and direct radiative forcing, 107.
- Najafi, M. R., Zwiers, F. W., & Gillett, N. P. (2015). Attribution of Arctic temperature change to greenhouse-gas and aerosol influences. *Nature Climate Change*, 5(3), 246–249.

<https://doi.org/10.1038/nclimate2524>

- O'Neill, N. T., Eck, T.F., Smirnov, A., Holben, B.N., and Thulasiraman, S. (2003). Spectral discrimination of coarse and fine mode optical depth. *Journal of Geophysical Research*, 108(D17), 1–15. <https://doi.org/10.1029/2002JD002975>
- O'Neill, N. T., Ignatov, A., Holben, B. N., & Eck, T. F. (2000). The lognormal distribution as a reference for reporting aerosol optical depth statistics; Empirical tests using multi-year, multi-site AERONET Sunphotometer data. *Geophysical Research Letters*, 27(20), 3333–3336. <https://doi.org/10.1029/2000gl011581>
- O'Neill, N. T., Eck, T. F., Holben, B. N., Smirnov, A., Dubovik, O., & Royer, A. (2001). Bimodal size distribution influences on the variation of Angstrom derivatives in spectral and optical depth space. *Journal of Geophysical Research: Atmospheres*, 106(D9), 9787–9806. <https://doi.org/10.1029/2000JD900245>
- O'Neill, N T, Eck, T. F., Holben, B. N., Smirnov, A., & Dubovik, O. (2001). Bimodal size distribution influences on the variation of Angstrom derivatives in spectral and optical depth space. *Journal of Geophysical Research*, 106(D9), 9787–9806. <https://doi.org/10.1029/2000JD900245>
- O'Neill, Norm T., Thulasiraman, S., Eck, T. F., & Reid, J. S. (2005). Robust optical features of fine mode size distributions: Application to the Qu??bec smoke event of 2002. *Journal of Geophysical Research D: Atmospheres*, 110(11), 1–16. <https://doi.org/10.1029/2004JD005157>
- O'Neill, Norm T., Pancrati, O., Baibakov, K., Eloranta, E., Batchelor, R. L., Freemantle, J., et al. (2008). Occurrence of weak, sub-micron, tropospheric aerosol events at high Arctic latitudes. *Geophysical Research Letters*, 35(14). <https://doi.org/10.1029/2008GL033733>
- Ramnarine, E., Kodros, J. K., Hodshire, A. L., Lonsdale, C. R., Alvarado, M. J., & Pierce, J. R. (2019). Effects of near-source coagulation of biomass burning aerosols on global predictions of aerosol size distributions and implications for aerosol radiative effects. *Atmospheric Chemistry and Physics*, 19(9), 6561–6577. <https://doi.org/10.5194/acp-19-6561-2019>
- Ranjbar, K., O'Neill, N. T., AboEl-fetouh, Y., Lutsch, E., Lesins, G., McCullough, E., et al. (2019). Extreme smoke event over the high Arctic. *Submitted to Atmospheric Environment*.
- Saha, A., O'Neill, N. T., Eloranta, E., Stone, R. S., Eck, T. F., Zidane, S., et al. (2010). Pan-Arctic sunphotometry during the ARCTAS-A campaign of April 2008. *Geophysical Research Letters*, 37(5), 1–7. <https://doi.org/10.1029/2009GL041375>
- Sayer, A. M., & Knobelspiesse, K. D. (2019). How should we aggregate data ? Methods accounting for the numerical distributions , with an assessment of aerosol optical depth. *Atmospheric Chemistry and Physics, Discussions*, (July), 1–36.
- Schmale, J., Zieger, P., & Ekman, A. M. L. (2021). Aerosols in current and future Arctic climate. *Nature Climate Change*, 11(February). <https://doi.org/10.1038/s41558-020-00969-5>
- Seinfeld, J. H., & Pandis, S. N. (2006). *Atmospheric Chemistry and Physics: From Air Pollution to Climate Change* (2nd editio). John Wiley & Sons, Inc.
- Sinyuk, A., Holben, B. N., Eck, T. F., Giles, D. M., Slutsker, I., Korkin, S., et al. (2020). The AERONET Version 3 aerosol retrieval algorithm, associated uncertainties and comparisons to Version 2. *Atmos. Meas. Tech*, 13, 3375–3411. <https://doi.org/10.5194/amt-13-3375-2020>

- Sioris, C. E., Abboud, I., Fioletov, V. E., & McLinden, C. A. (2017). AEROCAN, the Canadian sub-network of AERONET: Aerosol monitoring and air quality applications. *Atmospheric Environment*, *167*, 444–457. <https://doi.org/10.1016/j.atmosenv.2017.08.044>
- Sirois, A., & Barrie, L. A. (1999). Arctic lower tropospheric aerosol trends and composition at Alert, Canada: 1980-1995. *Journal of Geophysical Research*, *104*(D9), 11599–11618. <https://doi.org/https://doi.org/10.1029/1999JD900077>
- Slater, T., Hogg, A. E., & Mottram, R. (2020). Ice-sheet losses track high-end sea-level rise projections. *Nature Climate Change*, *10*(10), 879–881. <https://doi.org/10.1038/s41558-020-0893-y>
- Stone, R. S., Anderson, G. P., Andrews, E., Dutton, E. G., Shettle, E. P., & Berk, A. (2007). Incursions and radiative impact of Asian dust in northern Alaska, *34*(March), 1–5. <https://doi.org/10.1029/2007GL029878>
- Stone, R. S., Sharma, S., Herber, A., Eleftheriadis, K., & Nelson, D. W. (2014). A characterization of Arctic aerosols on the basis of aerosol optical depth and black carbon measurements. *Elementa: Science of the Anthropocene*, *2*, 1–22. <https://doi.org/10.12952/journal.elementa.000027>
- Tang, I. N. (1996). Chemical and size effects of hygroscopic aerosols on light scattering coefficients. *Journal of Geophysical Research*, *101*(D14), 19245. <https://doi.org/10.1029/96JD03003>
- Tegen, I., & Fung, I. (1994). Modeling of mineral dust in the atmosphere: Sources, transport, and optical thickness. *Journal of Geophysical Research*, *99*(D11), 22,897-22,914. <https://doi.org/10.1029/94JD01928>
- Tomasi, C., Kokhanovsky, A. A., Lupi, A., Ritter, C., Smirnov, A., O'Neill, N. T., et al. (2015). Aerosol remote sensing in polar regions. *Earth-Science Reviews*, *140*, 108–157. <https://doi.org/10.1016/j.earscirev.2014.11.001>
- Trivitayanurak, W., Adams, P. J., Spracklen, D. V., & Carslaw, K. S. (2008). Tropospheric aerosol microphysics simulation with assimilated meteorology: model description and intermodel comparison. *Atmospheric Chemistry and Physics Discussions*, *7*(5), 14369–14411. <https://doi.org/10.5194/acpd-7-14369-2007>
- Udisti, R., Traversi, R., Becagli, S., Tomasi, C., Mazzola, M., Lupi, A., & Quinn, P. K. (2020). Arctic Aerosols. In A. Kokhanovsky & C. Tomasi (Eds.), *Physics and Chemistry of the Arctic Atmosphere* (pp. 209–329). Springer Polar Sciences. Springer, Cham. https://doi.org/10.1007/978-3-030-33566-3_4
- Xie, Y., Li, Z., Li, L., Wagener, R., Abboud, I., Li, K., et al. (2018). Aerosol optical, microphysical, chemical and radiative properties of high aerosol load cases over the Arctic based on AERONET measurements. *Scientific Reports*, *8*(1), 1–9. <https://doi.org/10.1038/s41598-018-27744-z>
- Zhang, X., Huang, Y., Rao, R., & Wang, Z. (2013). Retrieval of effective complex refractive index from intensive measurements of characteristics of ambient aerosols in the boundary layer. *Optics Express*, *21*(15), 17849–62. <https://doi.org/10.1364/OE.21.017849>
- Zielinski, T., Bolzacchini, E., Cataldi, M., Ferrero, L., Graßl, S., Hansen, G., et al. (2020). Study of

chemical and optical properties of biomass burning aerosols during long-range transport events toward the arctic in summer 2017. *Atmosphere*, 11(1).
<https://doi.org/10.3390/ATMOS11010084>

3. Paper 2: Seasonal comparisons of GEOS-Chem TOMAS simulations with AERONET-inversion products over the Arctic

Submitted to Atmospheric Environment, September 2021

Supplementary material can be found [here](#).

Seasonal comparisons of GEOS-Chem-TOMAS (GCT) simulations with AERONET-inversion retrievals over sites in the North American and European Arctic

Y. AboEl-Fetouh¹, N. O'Neill¹, J.K. Kodros², J.R. Pierce², H. Lu³, K. Ranjbar¹, and P. Xian⁴

1 CARTEL, Université de Sherbrooke, Sherbrooke, Québec, Canada

2 Colorado State University, Fort Collins, Colorado, USA

3 Compute Canada/Quebec, Université de Sherbrooke, Québec, Canada

4 Marine Meteorology Division, Naval Research Laboratory, Monterey, CA, USA

Key Points

- 1) Fine mode effective radius was systematically underestimated by GCT. This was likely due to underestimated smoke particle size.
- 2) GCT captured the springtime coarse mode particle size distribution peak of the climatology as well as a weak but systematic fall increase.
- 3) GCT captured most fine and coarse mode seasonal aerosol trends previously observed in a climatology of Arctic AERONET sites.

Abstract

GEOS-Chem TOMAS (GCT) simulations of AERONET-inversion products during 2015 were compared with AERONET-inversion products from the multi-year climatology of Aboel-Fetouh et al. (2020) (AeF) and for year 2015 acquired over 5 stations in the North American and European Arctic. The GCT simulations of particle size distributions (PSD) did not capture a spring to summer radius increase of the fine mode (FM) peak observed by AeF but did capture AeF's springtime coarse mode (CM) peak (small-sized CM peak with a radius $\sim 1.3 \mu\text{m}$) and a weak late summer / fall increase in the amplitude of that peak. The lack of a spring to summer FM radius increase was likely due to the large GCT cell size ($4^\circ \times 5^\circ$) and associated difficulties in the modelling of coagulation-induced smoke particle size. Conversely, the GCT simulation of the small-sized CM peak indicated a successful capture of the springtime influx of Asian dust. The fall increase of that GCT peak was associated with an increase of a larger ($4 - 7 \mu\text{m}$) PSD mode that AeF suggested was due to local dust. GCT captured the seasonal (climatological-scale) FM AOD trend, the decreasing CM AOD trend, and the increasing trend of the FM fraction. The GCT CM AOD also showed a fall

increase that was coherent with the increase of the simulated small-sized CM peak and with a lesser rate of decrease of the AeF CM AOD. Large GCT deviations from the AERONET retrievals were attributed to an extreme July 2015 forest fire event.

1. Introduction

The importance of studying the impacts of aerosol radiation (direct effect) and aerosol cloud interaction (indirect effect) on climate change is well established (see Boucher et al., 2013). The climate forcing of aerosols over the Arctic is of particular importance due, notably, to climate feedback effects that result in Arctic amplification. Arctic aerosols are of local and remote (long-range transport) origins (see, for example, Hirdman et al., 2010). Their direct and indirect climate forcing role depends on their quantity independent (intensive) properties of chemistry, size and shape and quantity dependent (extensive) properties such as number, volume, or mass concentration: these properties are intrinsically related to the nature of the emission sources and the transport pathways into the Arctic.

Chemical transport models (CTMs) coupled with aerosol microphysics / chemistry packages are essential tools for understanding the dynamics of Arctic aerosols. However, modellers are faced with various challenges: for example, in the goal of rendering these models computationally fast there is a tendency to oversimplify their physical and chemical schemes. Table 1 of Schmale et al. (2021) presents a concise list of model deficiencies (as well as major measurement deficiencies) in simulating Arctic processes for aerosols of both local and long-range origin. The modelling deficiencies include the microphysics and chemistry of marine aerosols, the modelling of wet and dry deposition of aerosols during their transport, inadequate parameterizations of aerosols acting as INPs (ice nucleating parcels) and cloud / fog processing of aerosols. An important consideration in that paper was that (spatial/temporal) model resolutions were generally too coarse to capture particle formation mechanisms, the physical and chemical processing of aerosols and aerosol cloud interaction in general. The required model resolution and its degree of sophistication in simulating optical and microphysical aerosol dynamics is a trade-off that depends on the resolution of a given process as well as the type and resolution of the aerosol measurement being simulated.

The process of increasing the accuracy of the aerosol schemes employed in CTMs will augment the understanding of aerosol processes (including sources and composition) and forecasting abilities. The most comprehensive approach to improving model accuracy is to compare CTM simulations with columnar products of robust, 1st order, vertically integrated or vertically averaged aerosol parameters: parameters that models must satisfy before one can aspire to assess their simulation performance with respect to more 2nd order products at, for example, a single altitude. The Aerosol Robotic Network (AERONET) is a global network of ground-based sunphotometer/sky radiometer instruments that provide long-term retrievals of columnar aerosol products (over periods that range up to 20 years for the AERONET sites in the Arctic). The availability of these retrieval products enables the generation of robust climatological-scale databases that can form the basis of comparisons with CTM simulations.

AERONET “ground-truth” retrievals have been widely used in comparisons with satellite retrievals and model simulations. Hesaraki et al. (2017) provided a summary of model comparisons with Arctic

AOD and Angstrom parameter retrievals: the performance of the models could be generally characterized as good to marginal with respect to the simulation of both parameters. Breider et al. (2014) found reasonable agreement between Goddard Earth Observing System chemical-transport model (GEOS-Chem) simulations of climatological-scale AERONET/AEROCAN¹ AODs. Hesaraki et al. (2017) showed that springtime CM (coarse mode) AOD peaking due to Asian and/or Saharan dust and FM (fine mode) AOD peaking due to Arctic haze were approximately captured by GEOS-Chem. They also observed that FM AOD and CM AOD log-space histograms were better representations than linear-space histograms of the measured and modelled retrievals² (with attendant implications, for example, on the correlation coefficients of the simulations versus the retrievals).

The standard GEOS-Chem aerosol scheme (bulk model) is based on prescribed particle size distributions (PSDs) of speciated, externally mixed (independent), aerosol populations (with the exceptions of sea spray and dust, with 2 and 4 size bins, respectively). Bulk models do not incorporate aerosol microphysical processes that depend on the form of the PSD (nucleation and coagulation are examples of such processes). In contrast, the “Two Moment Aerosol Sectional” (TOMAS) microphysical package (Adams & Seinfeld, 2002) simulates a 40-bin (sectional) PSD with two moments (aerosol mass and number). The integration of TOMAS into GEOS-Chem is known as GEOS-Chem-TOMAS (hereafter referred to as GCT).

GCT has been used to gain insight into a variety of aerosol processes in the Arctic. These studies include (1) the drivers of new particle formation (Croft et al., 2016a) (2) the season cycle of Arctic PSDs (Croft et al., 2016b), (3) the role of marine organic species in shaping the Arctic PSDs (Croft et al., 2019), (4) Arctic black carbon mixing state (Kodros et al., 2018), and (5) the vertical profile of Arctic aerosol absorption and scattering (Leitch et al., 2020). While GCT was evaluated using in situ measurements in each of these Arctic-focused studies, it has not been evaluated with the comprehensive suite of columnar optical and microphysical properties that can be derived from the ground-based remote sensing of spectral AOD and almucantar radiance measurements: specifically the AERONET optical and microphysical inversions (Dubovik & King, 2000, Sinyuk et al., 2020).

In this paper, we compare GCT simulations with ground-based AERONET sunphotometer/almucantar radiometer inversions acquired over five Arctic stations (AboEl-Fetouh et al., 2020; hereafter AeF). We specifically compare seasonal (climatological scale) variations of a number of key parameters: PSDs and the radius position of certain seasonal and species dependent aerosol features along with key optical and microphysical parameters. These latter parameters include fine and coarse mode (FM and CM) AOD, FM and CM effective radii, and FM fraction (FMF) (defined in AeF). The seasonal AERONET parameters are compared with a single year of GCT simulations (2015). In doing so we evaluate GCT by comparing its single-year predictions within the envelope of a multi-year AERONET climatology as well as with AERONET retrieval parameters acquired specifically in the simulation year of 2015. This process enables a better understanding of the robustness of seasonal variations derived from the AERONET retrievals and how well GCT

¹ AEROCAN is the federated Canadian subnetwork of AERONET. From this point on we will, for the sake of simplicity, just refer to AERONET

² A finding that was validated for total AOD on a global scale (for AERONET and satellite retrievals) by Sayer & Knobelspiesse (2019).

simulations can be employed to predict these (climatological scale) variations across the Arctic. In addition, an analysis of the departures from seasonal variations by both the AERONET retrievals and GCT simulations informs our understanding of the optical and microphysical dynamics of those departure events.

2. AERONET retrievals and models

2.1 AERONET inversions

AeF employed climatological scale (monthly binned), Version 3, Level 1.5 AERONET inversions from six AERONET sites in the North American and European Arctic. Microphysical and optical parameters of an extensive-parameter nature were reported in terms of geometrical means and standard deviations while intensive-parameter properties such as effective radius, and semi-intensive parameters, such as the FMF, were reported in terms of arithmetic means and standard deviations. The AERONET optical parameters were interpolated to 550 nm to match the typical wavelength of the aerosol modelling community. Further details on the choice of statistical measures, the choice of AERONET product level, the interpretation of the seasonal trends and multi-year histograms can be found in AeF.

The five AERONET stations employed in this study are: 1) Barrow, Alaska, USA, 2) Resolute Bay, Nunavut, Canada, 3) PEARL-Eureka, Nunavut, Canada, 4) Thule, Greenland, Denmark, and 5) Hornsund, Spitsbergen, Norway. Details on the latitude, longitude and elevation of each station are given in Table 1 of AeF along with their MYSP (the multi-year sampling period over which their aerosol climatologies were derived). Details on the reasons for the selections of these stations are also outlined in AeF.

2.2 Modelling considerations

The TOMAS aerosol microphysics scheme was originally described in Adams & Seinfeld (2002). Its coupling to GEOS-Chem is originally described in Trivitayanurak et al. (2008), and the specific model setup and emissions used here are described in Kodros and Pierce (2017). In this work, we use GEOS-Chem version 10.01 (further details can be found here: <https://geos-chem.seas.harvard.edu/>). The model is driven by MERRA-2 (second Modern-Era Retrospective analysis for Research and Applications) assimilated meteorology (Gelaro et al., 2017). The latitude/longitude grid size is $4^\circ \times 5^\circ$ with 47 vertical levels up to 0.01 hPa: for the purposes of our columnar analysis, we focussed on the lower 30 layers, up to ~ 250 hPa (around 10 km). Aerosol mass and number concentrations were recorded every 6 simulation hours.

The TOMAS module in GCT is a comprehensive aerosol microphysics model that explicitly simulates PSD evolution by condensation, coagulation, nucleation, size-dependent emissions, and size-dependent deposition. In contrast, simpler bulk aerosol schemes tend to make PSD and aerosol mixing simplifications for reasons that are often related to operational considerations (see, for example, the sectional vs bulk PSD analysis of cloud-condensation-nuclei impact carried out by Kodros & Pierce (2017) for a comparison of the impacts of the two types of models). GCT tracks total particle number and speciated particle mass (i.e., the output of the model at any given time, grid cell and vertical layer is total particle number and speciated mass) across 40 size bins with dry bin radii ranging from approximately $0.0005 \mu\text{m}$ to $5 \mu\text{m}$. Within each size bin, all species except black

carbon are assumed to be internally mixed (multi-species particles) while black carbon is externally mixed.

Mie (spherical-particle) optical theory (see, for e.g., Bohren & Huffman, 2004) was employed to calculate 550 nm AODs offline (“offline” in the sense that the speciated mass of any given radius bin at any given grid cell was transformed, post GCT simulation, into radius and refractive index inputs required by the Mie program). The real and the imaginary parts of the refractive indices (n and k) and the densities of the pure GCT aerosol types are listed in Table 1. The assumed n and k values for each species must be weighted by the species volume-fractions to obtain composite n and k value for the mixture in any given GCT grid cell at any given simulation time (see Lesins et al. (2002) and Curci et al. (2015) for a general optical discussion on mixed aerosol components).

Aerosol Type	n	k	Density (kg/m³)	Reference for density
Water (H ₂ O)	1.33	1.96E-9	1000	-
Sulphate (SO ₄)	1.43	1.00E-8	1780	Tang (1996)
Sea-salt (SS)	1.50	1.00E-8	2165	Tang (1996)
Black Carbon (BC)	1.95	0.79	1800	Bond & Bergstrom (2006)
Organic Carbon (OC)	1.53	6.00E-3	1400	Dick et al. (2000)
Dust	1.53	5.50E-3	2650	Tegen & Fung (1994)

Table 1 Nominal values of the mass density as well as the 550 nm values of the real and imaginary parts of the refractive index employed to characterize GCT aerosol types.

The coarse TOMAS spatial resolution of 4° x 5° that we employed in the context of this paper is limited in its capacity for monitoring high frequency aerosol events in the spatial and temporal domain. It is better suited to climatological scale comparisons with AeF’s detailed, multi-parameter seasonal climatology. The GCT ingestion of smoke emission information from satellite hot-spot retrievals is dynamic but of relatively low frequency (daily temporal resolution). As a means of better understanding significant event-level departures of GCT from AeF’s seasonal climatology (specifically for a 2015 case of high frequency smoke intrusions into the Arctic), the Navy Aerosol Analysis and Prediction system (NAAPS) model was employed to simulate speciated 550 nm AODs at a relatively high spatial resolution (1° x 1°). NAAPS is a global aerosol transport model which simulates four externally mixed species of aerosols (FM smoke, FM anthropogenic and biogenic aerosols, CM dust and CM sea salt). It uses bulk microphysics in order to achieve fast (operational) computational times. The NAAPS reanalysis version that we employed in this study (the NAAPS-RA model described by Lynch et al., 2016) assimilates quality controlled (550 nm) MODIS-retrieved AODs. At sub-Arctic latitudes, NAAPS-RA benefits from a rapid sampling of biomass burning (MODIS hot-spot) emission sources (hourly database) coupled with assimilated MODIS AODs that are significantly more spatially comprehensive than those acquired over the Arctic. The underlying meteorology that drives NAAPS also incorporates meteorological observations through data assimilation at its analysis time. More information on NAAPS-RA can be found in the supplementary material.

3. Methodology

3.1 On the general nature of our GCT vs AERONET comparisons

AERONET does not provide speciated aerosol products. However, as pointed out by AeF, the algorithmic division into FM and CM aerosols is a form of speciation since the formation and transportation mechanisms governing aerosol dynamics is very much bimodal in nature. This bimodality feature provides a basis for investigating the extensive and intensive parameters of interest from both the ground-based retrievals and model simulations (AeF) .

The approach taken in this comparison analysis was to contextualize the 2015 GCT simulations (and the 2015 AERONET retrievals) in terms of the MYSP climatological-scale findings of AeF: namely the seasonal, monthly-binned trends of the fundamental FM and CM retrieval parameters of the AERONET inversion. We then analysed the similarities-to or departures-from the climatological-scale seasonal MYSP results. In the case of significant departures, we performed more detailed investigations of the 2015 retrievals and simulations in order to better understand the reasons for those departures. The underlying rationale for this approach is that GCT, even GCT constrained to a single year, can largely simulate the seasonal (climatological-scale, month to month) variations of a variety of optical and microphysical, extensive, and intensive parameters acquired by the AERONET extinction/sky radiance retrievals.

It must be emphasized that the number of per-month AERONET retrievals are typically small³ (notably in the case of one single year of retrievals). A threshold of 10 retrievals per month was (somewhat) arbitrarily set for admissible monthly averages (thus, for example, only Thule had a sufficient number of retrievals to pass the 10-retrieval threshold for the month of April 2015). That threshold aside, the small-N (small sample number) AERONET statistics of 2015 (see the AERONET-inversion retrieval numbers for 2015 in the legends of Figure 1) are generally expected to be at the margins of significance (Barrow, for example, shows no month with higher than 23 retrievals).

The AERONET Level 1.5 inversion products are cloud screened. GCT simulations can be processed through a crudely analogous filtering process wherein simulation points of a certain relative humidity (RH) threshold are excluded from the monthly averaged statistics. As a check on the statistical impact of this GCT “cloud screening” process we compared monthly “cloud screened” FM and CM AOD GCT averages with the standard monthly averages that were free of any RH filtering (the results, discussed below, employed a RH threshold of 95%). The temporal irregularity of AERONET retrievals can have an effect on comparisons between the GCT and AERONET averages of 2015. We tested this potential source of sampling bias below by limiting GCT FM and CM AODs admissible to the monthly averaging to times that were synchronized to AERONET retrieval times (where “synchronized” refers to AERONET retrievals being within ± 3 hours of the nominal GCT times).

Finally, we note that while AERONET bins have fixed radii, the exact GCT bin radii are dynamic: bin radii depend on mass to radius conversion factors (including the contribution of RH-driven

³ within a context of the retrieval histogram of a given month being representative of its large-N probability distribution.

aerosol water uptake) in each grid cell of the simulation domain. Practically, this means variations in radius bin centers of $<\sim 1\%$ at the smallest radii to $<\sim 5\%$ at the largest radii (from computations of the coefficients of variation computed for all stations and all months of the 2015 simulation).

3.2 Aerosol parameters and their comparison protocols

The AERONET-derived, monthly-binned parameters that we employed were the arithmetically averaged PSD, the 550 nm geometric means and geometric standard deviations of the FM and CM optical depths ($\tau_{f,g}$, $\tau_{f,g} \times \mu_f^{\pm 1}$ and $\tau_{c,g}$, $\tau_{c,g} \times \mu_c^{\pm 1}$) the arithmetic means and standard deviations of the FM and CM effective radii ($\langle r_{eff,f} \rangle \pm \sigma(r_{eff,f})$ and $\langle r_{eff,c} \rangle \pm \sigma(r_{eff,c})$) as well as the 550 nm FMF (details on the climatological-scale MYSP statistical approach for deriving monthly-binned averages can be found in AeF). Implicit in this choice of parameters is the question of the opto-physical significance of any given retrieval parameter: this is intrinsically related to the trade-off between a finer (high order) choice of parameters (i.e., “order” in the sense of a Taylor series function of the dependent parameters of wavelength and almucantar angle) and the level of significance that one can aspire to from the AERONET retrievals given the typical errors in spectral AOD and almucantar radiance. The FM / CM characterization is, for typical AOD and almucantar radiance accuracies, essentially a low order type of retrieval (see, for example Table 1 of O’Neill et al. 2003). We, nonetheless, also considered details of the full-fledged PSD retrieval product in order to investigate the possibility of higher order sensitivities.

We derived off-line GCT parameters analogous to all the AERONET retrieval parameters and then computed monthly binned analogues to the monthly binned AERONET retrievals defined in the previous paragraph. As part of the comparison protocol, we defined a FM versus CM cut-off radius that simulated as nearly as (practically) possible the cut-off radius of the AERONET processing stream. That cut-off radius was taken as the minimum of the retrieved particle-volume size distribution retrieval where the minimum is limited to four prescribed bin-center choices (approximately 0.439, 0.576, 0.756 and 0.992 μm). We chose the average AERONET-derived, station-dependent cut-off radius for each month.

AERONET PSDs are retrieved over 22 equally spaced logarithmic bins (Dubovik et al., 2002) while the GCT bin radii, as noted above, vary by a small percentage. A more substantive element in the PSD comparisons is that the AERONET radius bin-center range extends up to 15 μm whereas the center of the largest GCT bin is only $\sim 4.5 \mu\text{m}$. At the lower end of the radius scale, GCT extends an order of magnitude below the AERONET PSD retrieval range. When deriving bin constraints analogous to AERONET, we simply cut off the GCT range at the AERONET minimum (lowest bin edge of 0.04 μm radius as per Table S1.2 in the supplementary material). At the upper radius range, we excluded AERONET bins of bin-centre radius greater than 4 μm when calculating $r_{eff,c}$ from the AERONET PSD retrievals.

The fixed temporal sampling resolution of the GCT simulations produces 4 points per day or 120 points per 30-day month. In contrast, the AERONET sampling rate is nominally higher (once per hour) but, because of cloud obscuration, light-season limitations and other sampling constraints, it is very irregular (to the extreme limit of the polar night for the high Arctic stations when there are no retrievals from late September to late March).

4.Results

4.1 PSD comparisons

Figure 1 shows AERONET PSDs (left column) vs GCT simulations (right column) for 2015 (the MYSP PSDs of AeF were excluded, for the sake of simplicity, in this one case). The AERONET admissibility threshold of 10 retrievals can significantly curtail the seasonal extent of the 2015 results (to the point, for example, that only Thule statistics were admissible for the month of April).

AeF reported a systematic spring to summer increase in the radius of the FM peak over the MYSP of all stations (except Resolute Bay). They attributed this increase to the seasonal transformation from a dominance of smaller FM Arctic haze aerosols in the spring to a dominance of larger FM smoke aerosols in the summer. The retrieved 2015 AERONET PSDs of Figure 1 generally show a similar spring to summer FM increase (see, respectively, the grey and dark-grey dashed vertical lines superimposed on the May and July peaks) as that reported by AeF⁴. The singular month of August at Resolute Bay, PEARL and Thule did not follow this Figure 1 trend (while the trend at Hornsund could not be evaluated given only two months of admissible retrievals). GCT shows no significant spring to summer increase in the radius of the FM peak: a null result that was, at least, in part due to GCT underestimating smoke particle size (see Sections 4.2.1 and 4.3.1 below). The AERONET retrievals and the GCT simulations both show the general maximum amplitude of the FM peak in July⁵ (the results of an extreme July smoke event as we discuss below).

All AERONET stations capture the April/May component of the springtime CM peak at 1.3 μm (peak that AeF attributed to Asian dust) while also capturing a June peak whose radius position is more variable than the (largely 1.3 μm) “weaker amplitude peak in June” reported by AeF. The capture of peak springtime bin-center values from 1.2 to 1.5 μm by GCT is roughly in agreement with the Asian dust peak of the AERONET retrievals.

A second set of 2015 AERONET peaks from ~ 3 to 7 μm in July and/or August for all stations is roughly coherent with the ~ 4 to 7 μm ⁶ late summer and early fall CM peaks reported by AeF⁷. They argued that an increase in the amplitude of the 4 to 7 μm CM peaks might be attributable to an increasing influence of wind-induced sea-salt and / or local dust aerosols. They also noted that local dust might represent the key influence since sea-salt particle sizes (estimated to be in the 2 – 4 μm volume-mean-radius range) were at the lower margin of the 4 to 7 μm peak. Ongoing, local-dust investigations of AERONET PSDs, supported by microphysical PSDs and lidar at the OPAL Eureka

⁴ who reported increases from .04 to 0.08 μm from a springtime value close to 0.15 μm .

⁵ The word “amplitude” is used frequently below. With respect to the PSD of Figure 1, we mean the magnitude of some $dV/d\log r$ feature (notably associated with some modal peak)

⁶ There is an incoherence in AeF wherein the peak range is sometimes referred to as “5–7 μm ” and sometimes “4 to 7 μm ”. We retained the more general 4 to 7 μm AeF range for use in the current paper.

⁷ the increase (noted by AeF) in the amplitude of that feature from July to August for Barrow, Resolute Bay and Hornsund is inconclusive for the 2015 retrievals with only Resolute Bay having a (marginally) significant number of retrievals

site suggest that a (very flat) local dust peak occurs at a radius $\sim 3 - 6 \mu\text{m}$ during July and August (co-author K. Ranjbar).

The lack of such a 4 to 7 μm peak in the GCT PSDs as well as their tendency (unlike the 3 to 7 μm AERONET peaks) to rapidly decrease in amplitude as the season progresses merits further comment. The spring to summer amplitude decrease of the GCT CM peaks is coherent with the amplitude decrease of the 1.3 μm (Asian dust) AERONET peaks of AeF and with the AERONET retrievals of 2015 for certain stations (namely Barrow, PEARL, and Thule; the decrease is of marginal significance for Hornsund and does not exist for Resolute Bay). The decreasing-amplitude trend of the GCT peaks goes through a noteworthy reversal with an amplitude increase at all stations in September (as well as an apparently modest increase in the radius position of the GCT peak at Barrow and Hornsund in August). These fall (late summer) increases in the amplitude or position of the GCT peaks suggest a GCT sensitivity to the increasing amplitude of winds (and thus wind-generated sea-salt and/or local dust) in the fall (late summer)⁸ with a limitation to small-sized CM particles (the CM peak of 1.2 to 1.5 μm radius noted above coupled with the modal extent of that feature). We will return to a discussion of those moderate increases in the sections on the seasonal variation of the CM AOD and effective radius below.

⁸ see, for example, the iconic high- and low-wind soil plot (Figure 11) of Sirois & Barrie, 1999 and AeF's GEOS-chem-generated seasonal plot (Figure 1b) of salt and dust (CM) AOD.

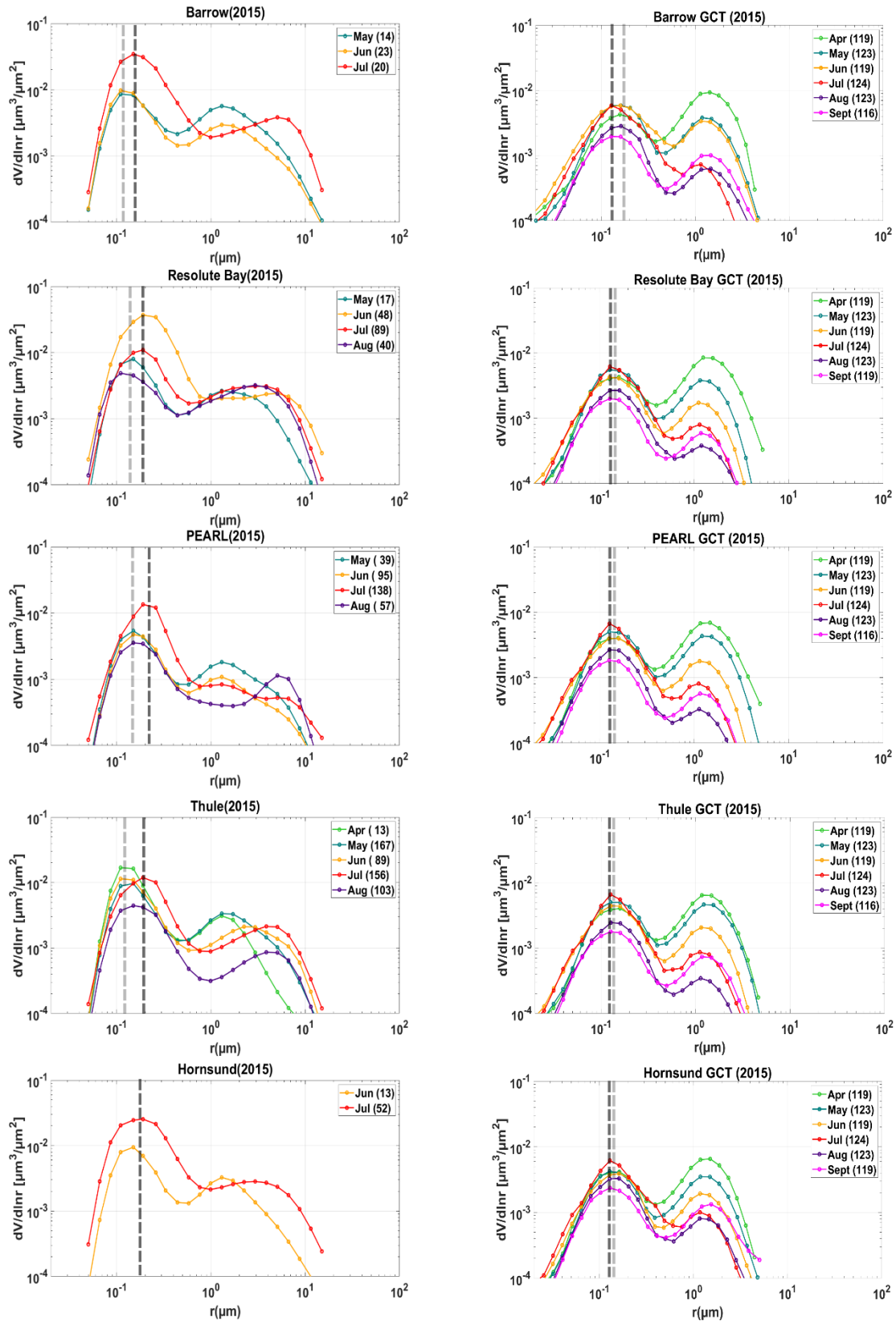


Figure 1 Monthly averaged volume PSDs of the five Arctic stations for 2015 AERONET retrievals (left column PSDs) and the GCT simulations (right column PSDs). The reader is referred to Table S1.1 and Table S1.2 of the supplementary material for specific bin center and bid edge values. The color of the curves corresponds to specific months where blue/green represents the spring months, orange/red the summer, and purple/bright pink the fall months. The total number

of retrievals/points are shown in parentheses for each month. The vertical dashed grey and dark-grey lines indicate the spring and summer peaks respectively. In order to not burden Figure 1 with an excess of PSD details we purposely omitted the MYSP climatology PSDs of AeF. The reader is accordingly referred to that paper in order to make comparisons between the 2015 GCT and AERONET PSDs above with AeF's AERONET climatology.

4.2 AOD comparisons

4.2.1 FM AOD

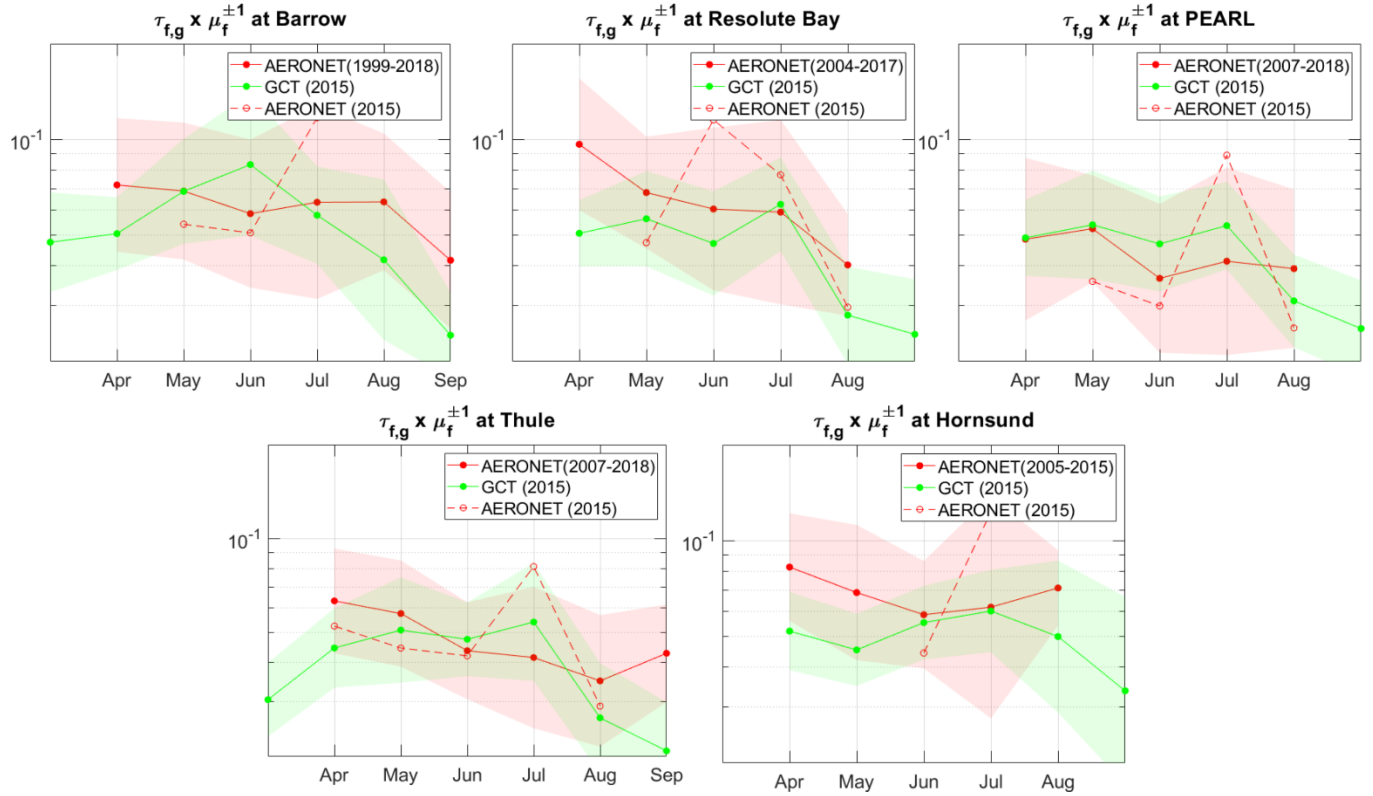


Figure 2 Month to month variation of the geometric means ($\tau_{f,g}$ represented by circular symbols) and their geometric standard deviation ($\tau_{f,g} \times \mu_f^{\pm 1}$ represented by color-matched shading) for all 5 Arctic stations. The solid red circles represent AERONET climatological-scale retrievals reported by AeF. The red open circles (with no associated shading) represent the 2015 AERONET retrievals while the solid green circles represent 2015 TOMAS simulations.

Figure 2 shows AeF's seasonal FM AOD climatology: the red solid-line shows the geometric means ($\tau_{f,g}$) while the pink envelope indicates the geometric standard deviation limits ($\tau_{f,g} \times \mu_f^{\pm 1}$). The analogous statistical parameters for the 2015 GCT simulations are shown, respectively, as a green solid line surrounded by a green envelope. The cloud screening test (the impact of excluding GCT points for which the RH > 95%) showed that cloud screening had no significant effect. The impact of restricting GCT $\tau_{f,g}$ computations to times that were synchronous with AERONET retrieval times yielded differences of $< \sim 0.006$ (33%) for large-N months ($N \geq 20$) and significantly larger differences of small-N months. In other words, GCT inevitably suffers from the same small-N statistical precariousness expected for the AERONET retrievals. It is worth noting that, non surprisingly, small N GCT values were generally associated with small-N AERONET retrievals.

The 2015 GCT results of Figure 2 are, with the exception of specific cases which we will explore below, RH reasonably close to the seasonal AeF variations ($\tau_{f,g}$ values that are generally well within

each other’s standard deviation). Large-amplitude negative biases relative to the AeF climatology are most evident in the month of April for the GCT estimates at Barrow, Resolute Bay, Thule and Hornsund. The GCT seasonal simulations of Croft et al. (2016) underscored the (pan-Arctic, tropospheric) competition between accumulation (fine) mode (Arctic haze) increase in number density (largely due to northward transport of pollutants and Aitken mode condensation) and the decrease in accumulation mode lifetime due to wet deposition during the April-May spring transition (their Figure 8). The level of agreement between the GCT version chosen for their Figure 8 results (NEWSCAV+COAG) and surface measurements at Alert suggest that a modification of one or more of the three critical Figure 8 processes (with a focus on higher altitude impacts) would achieve a better match with the April $\tau_{f,g}$ results of AeF⁹. Large negative biases between GCT and the AeF climatology also occur at Barrow and Thule in September (the only sites for which there was a threshold value of 10 or more retrievals during that month). The GCT decrease is generally consistent with the (Figure 5, “NEWSCAV+COAG”) August to September decrease of (“N20” and “N80”) accumulation mode surface number density reported by Croft et al. (2016). AeF, on the other hand, noted the small-N precariousness of FM AOD statistics in the AERONET climatology during that month.

The July 2015 AERONET $\tau_{f,g}$ retrievals (dashed red lines in Figure 2) are near the limits of or extend above the pink AeF envelope for all stations except Resolute Bay (which displays a $\tau_{f,g}$ peak in June¹⁰). Except for Barrow, the 2015 GCT $\tau_{f,g}$ values increase in July as well: the increases are inevitably sensitive at the event level to the dynamic (satellite-derived) GCT hot-spot emissions database but are considerably muted relative to the AERONET retrievals. Sioris et al. (2017) and Ranjbar et al. (2019) noted that the ($\tau_f \sim 1$) peak during the 7-14 July 2015 period was an extreme smoke event at the PEARL site (with a confidence of $\sim 99.6\%$ if we employ the extreme-event statistics of the latter citation). Movie S1 shows site by site τ_f temporal variations alongside animations of daily-averaged τ_f maps generated by GCT and NAAPS: the τ_f time series at all 5 sites show that GCT does not capture the higher frequency AERONET τ_f variations while NAAPS smoke AODs produce variations that respond in a similar higher frequency fashion to AERONET variations. The spatial animations and the synchronized temporal profiles support an argument that the difference in results is largely due to the AOD-driven features of NAAPS-RA coupled with differences in the spatial resolution of the two models. We note that the objective of the GCT simulations is to successfully model climatological-scale seasonal variations: the low frequency filtering of extremely high frequency events like the July 2015 smoke event is what we seek at the climatological scale.

In Section 4.3.1 below, we show that the GCT FM effective radii ($\langle r_{\text{eff},f} \rangle$) were significantly and systematically smaller than those of the AeF climatology and the 2015 AERONET retrievals (for all stations). The generally large-amplitude negative bias of GCT $\tau_{f,g}$ estimates relative to the AERONET July 2015 retrievals are magnified in Figure S1 (solid-green curve) for all five stations.

⁹ although one would need to be wary of the precarious small-N results for Resolute Bay

¹⁰ τ_f variations from the much higher temporal resolution AERONET-SDA product show a precipitous drop exactly from June 30 to July 1. This is an example of the precariousness of the assignment of $\tau_{f,g}$ values to a specific monthly bin in the presence of an extreme or near-extreme smoke event near the bin border between two months

An approximate Mie transformation applied to the OC component of the GCT $\tau_{f,g}$ values (assuming a change in $r_{\text{eff},f}$ from the GCT to the 2015 AERONET $\langle r_{\text{eff},f} \rangle$ values of Figure 6) yielded the dashed green (“enhanced”) curve of Figure S1. The agreement of the enhanced curve relative to the 2015 AERONET values is significantly better (with greater differences for the small-N, large geometric standard deviation values of Barrow and Hornsund (c.f. the N values of Figure 1)). This approximate argument supports the hypothesis of Section 4.3.1 that the GCT $\langle r_{\text{eff},f} \rangle$ underestimates of Figure 6 are largely attributable to shortcomings in estimating smoke (OC) particle size.

4.2.2 CM AOD

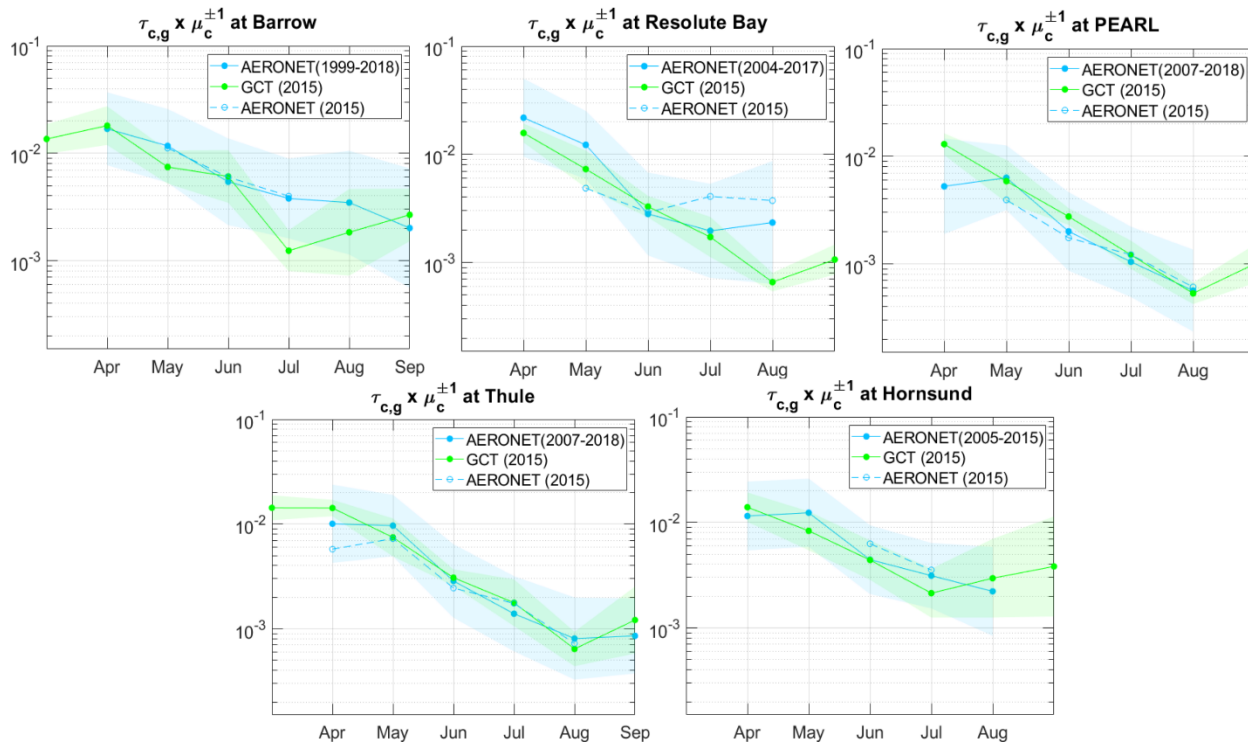


Figure 3 Seasonal $\tau_{c,g}$ variation for all five Arctic stations. Same caption as in Figure 2 (with subscript “c” replacing subscript “f” and the colour red being replaced by the colour blue).

Figure 3 shows the 2015 GCT $\tau_{c,g}$ simulations and the 2015 AERONET retrievals superimposed on AeF’s original climatology. The $\tau_{c,g}$ cloud screening impact was identical to the $\tau_{f,g}$ tests (negligible). The impact of restricting GCT $\tau_{c,g}$ computations to AERONET-synchronous retrieval times yielded similar results to the fine mode analysis: differences of $< \sim 0.0004$ (9%) for months with $N \geq 20$.

The AeF and 2015 AERONET retrievals show a seasonal tendency that is similar to the GCT simulations: a general spring to summer decrease that AeF ascribed to the diminishing influence of Asian dust. The 2015 AERONET and GCT curves are usually well within the blue-coloured geometric standard deviation envelope of the AeF climatology: the notable differences relative to the 2015 retrievals occur for July at Barrow and August at Resolute Bay. The July Barrow results are likely influenced by small-N statistics (that actually impact all 2015 Barrow retrievals).

The GCT $\tau_{c,g}$ values show a significant fall (August or September) increase for all stations. This behavior is coherent with the increasing amplitude of the small-sized (1.2 to 1.5 μm radius peak) GCT modal feature described above (which we suggested was linked to the appearance of wind-induced sea-salt and/or dust particles). The optical influence of this modal feature extends to radii significantly above those peak radii (extends well into radius regions where the modal feature has fallen well off from the peak) because of the associated increase in particle size: the (per particle) extinction cross section (effective optical extinction area) increases rapidly with increasing radius. The 2015 AERONET $\tau_{c,g}$ retrievals are largely insensitive to what is likely a real upturn in CM AOD while AeF noted a less rapid decrease of $\tau_{c,g}$ at Barrow, Resolute Bay and Hornsund. We note that the effective limit of August for (sufficiently high-N) AERONET inversions (even at the climatological scale) unfortunately inhibits our analysis of this GCT feature precisely when fall winds become stronger and more influential in generating substantial sea-salt and / or local dust events: the exploitation of moonphotometry (which already exists at several AERONET Arctic sites) and/or starphotometry¹¹ would help to better characterize the fall transition period.

4.2.3 FMF

The seasonal 2015 AERONET FMF results (Figure 4) largely follow the AeF climatology trend with the largest differences occurring in the early spring and late summer / fall when the weak number of retrievals has some impact (in spite of large $\tau_{f,g}$ differences in July, the FMF difference is minimal because $\tau_{f,g}$ is dominant over $\tau_{c,g}$ and the FMF is, accordingly, a rather insensitive near-unity value). Similarly, the GCT 2015 FMF largely agrees with the FMF from the AeF climatology (the differences in Figure 5 are somewhat magnified by the relatively small extent of the FMF scale). The rough FMF similarity of all the curves is coherent with the reasoning reported in AeF: that the generally increasing FMF seasonal behaviour is driven by the generally decreasing seasonal amplitude of $\tau_{c,g}$.

¹¹ currently located at Eureka and at Ny Alesund (some 240 km northwest of Hornsund)

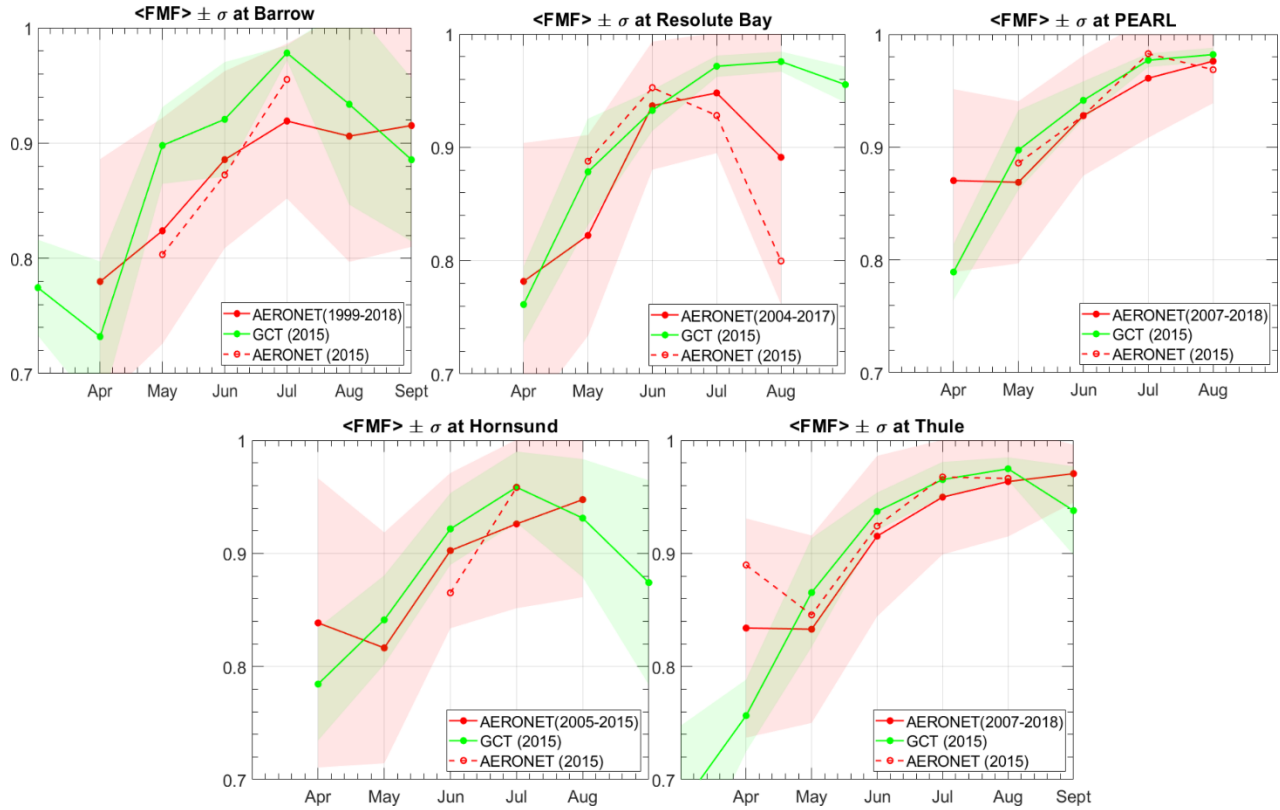


Figure 4 Seasonal FMF variation for all five Arctic stations. Same caption as Figure 2 (with appropriate changes to reflect that the statistics are represented by the arithmetic means and standard deviations of FMF).

4.3 Effective radius

Effective radius, being an intensive parameter in the context of FM or CM aerosols, is largely insensitive to the high (spatial and temporal) variations that characterize extensive parameters such as AOD. This robustness, as we will see in the following subsections, can provide clues to the nature of certain aerosol mechanisms or aerosol characteristics.

4.3.1 FM effective radius

Figure 5 shows the seasonal variation of monthly (arithmetically) averaged FM effective radii ($\langle r_{eff,f} \rangle$). AeF pointed out that the $> \sim 0.02 \mu\text{m}$ seasonal increase in $\langle r_{eff,f} \rangle$ from spring to summer was likely due to the influence of large-particle FM smoke and the waning influence of FM Arctic haze. We supplied event-level evidence above on the extreme nature of the July 2015 smoke event. The GCT $\langle r_{eff,f} \rangle$ values of Figure 5 are biased negatively with respect to the AERONET retrievals¹². This is a bias that is significant relative to AeF and its pink envelope (except for Hornsund, the GCT mean is separated from the AeF mean by at least one AeF geometric standard deviation).

¹² biased negatively with respect to both AeF retrievals and the 2015 retrievals: in fact, the AeF climatology and 2015 retrievals are generally quite close. This is in keeping with the robustness of intensive parameters such as the FM effective radius

The key influence on GCT underestimation relative to the AERONET July 2015 retrieval averages during the heavy smoke month of July 2015 is likely related to GCT underestimation of smoke particle size¹³. Ramnarine et al. (2019) showed that the coarseness of a GCT spatial resolution of $4^\circ \times 5^\circ$ (the same as ours) resulted in a substantial underestimate of smoke particle size due to inadequate simulation of coagulation mechanisms (for a simulation corresponding to 24 hours of particle trajectory time). The diameter (and radius) of the number density PSD was $\sim 60\%$ larger with subgrid coagulation compared with a run without subgrid coagulation. The surface and volume PSDs and thus the effective radii likely go through a similar relative increase (see the log translatable PSD discussion of O'Neill et al., 2005), at least during smoke-impacted retrievals. In comparison, the increase from the GCT to AERONET $\langle r_{eff,f} \rangle$ values of Figure 6 were $\ll 60\%$. In terms of the remote sensing relevance of AERONET $r_{eff,f}$ retrievals in actual smoke conditions, O'Neill et al., (2005) multi-station AERONET analysis amounted to an indirect validation of such retrievals: they showed a systematic $r_{eff,f}$ increase of $0.034 \mu\text{m}$ per day of particle trajectory time for mid-latitude U.S. and Canadian AERONET stations during an extreme smoke event induced by intense fires near Hudson's Bay.

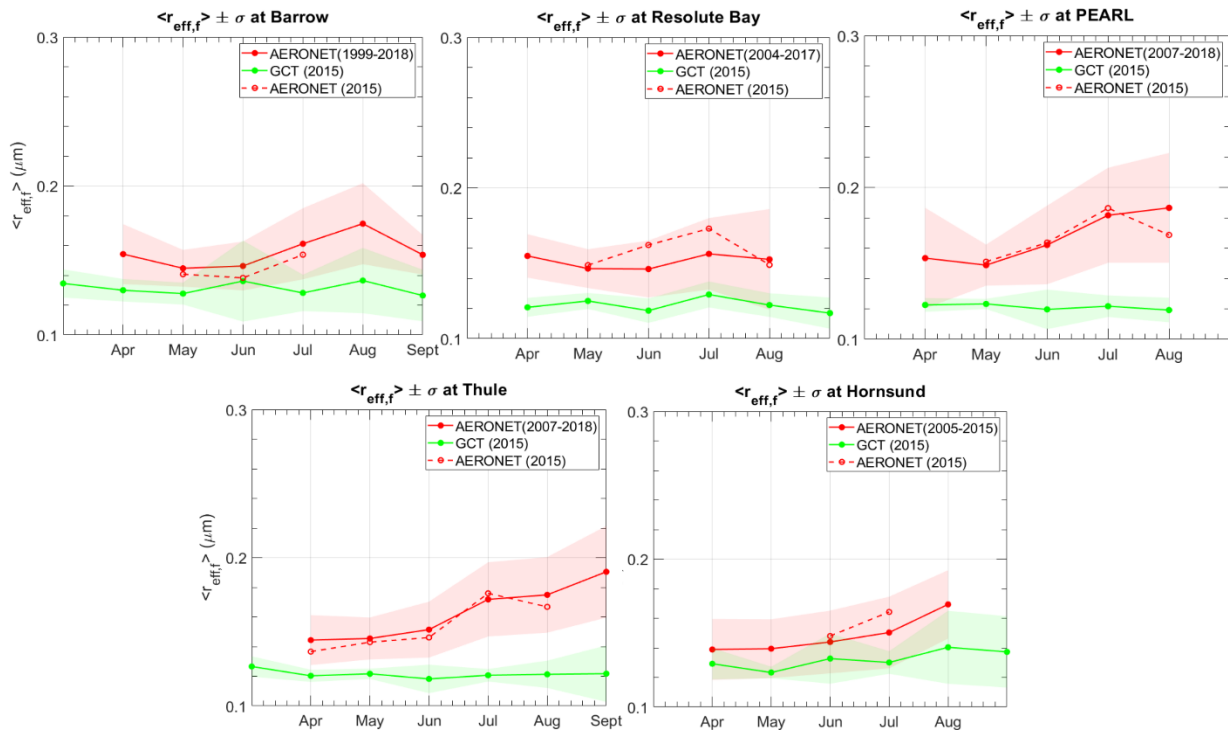


Figure 5 Seasonal $\langle r_{eff,f} \rangle$ variation for all five Arctic stations. Same caption as Figure 2 (with appropriate changes made for the arithmetic means and standard deviations of $r_{eff,f}$).

¹³ We note that GCT also underestimates the springtime $\langle r_{eff,f} \rangle$ values by $\ll 0.03 \mu\text{m}$. While we did not investigate the springtime difference in detail it is known that springtime smoke can be a factor of consequence that is even dominant in certain years (see the 2008 emissions and (PEARL) $\langle \tau_f \rangle$ variations shown in Figure 3 of Ranjbar et al.(2019).

4.3.2 CM effective radius

The arithmetic means of the CM effective radii ($\langle r_{eff,c} \rangle$) are plotted in Figure 6. The 2015 AERONET values are moderately close to the climatology curve (well within or near the edges of one AeF standard deviation). AeF attributed the spring to summer $\langle r_{eff,c} \rangle$ increase to the decreasing influence of the 1.3 μm (Asian dust) CM peak and the attendant increasing influence of the larger-radius 4 to 7 μm peak. GCT, as indicated above in the discussion of the 2015 PSDs (section 4.1), can not, given its bin-center upper limit of 4.5 μm , capture this second CM peak. However, we also noted that GCT did capture an amplitude increase and (not always) a moderate radius-position increase in the small-radius (1.2 to 1.5 μm) CM peak in August or September (with an attendant increase or lesser rate of seasonal decrease in $\tau_{c,g}$). However, Figure 6 also shows a slow, seasonal GCT increase which is not confined to the months of August and September: while that seasonal increase is certainly influenced by the increase in amplitude and radius position of the small-radius GCT peak observed in Figure 1, it is complicated by the nature of the effective radius calculation: the minimum of the general CM GCT PSD (Figure 1) as well as the AERONET driven cut-off between the FM and CM regions are variable (see Section 3.2).

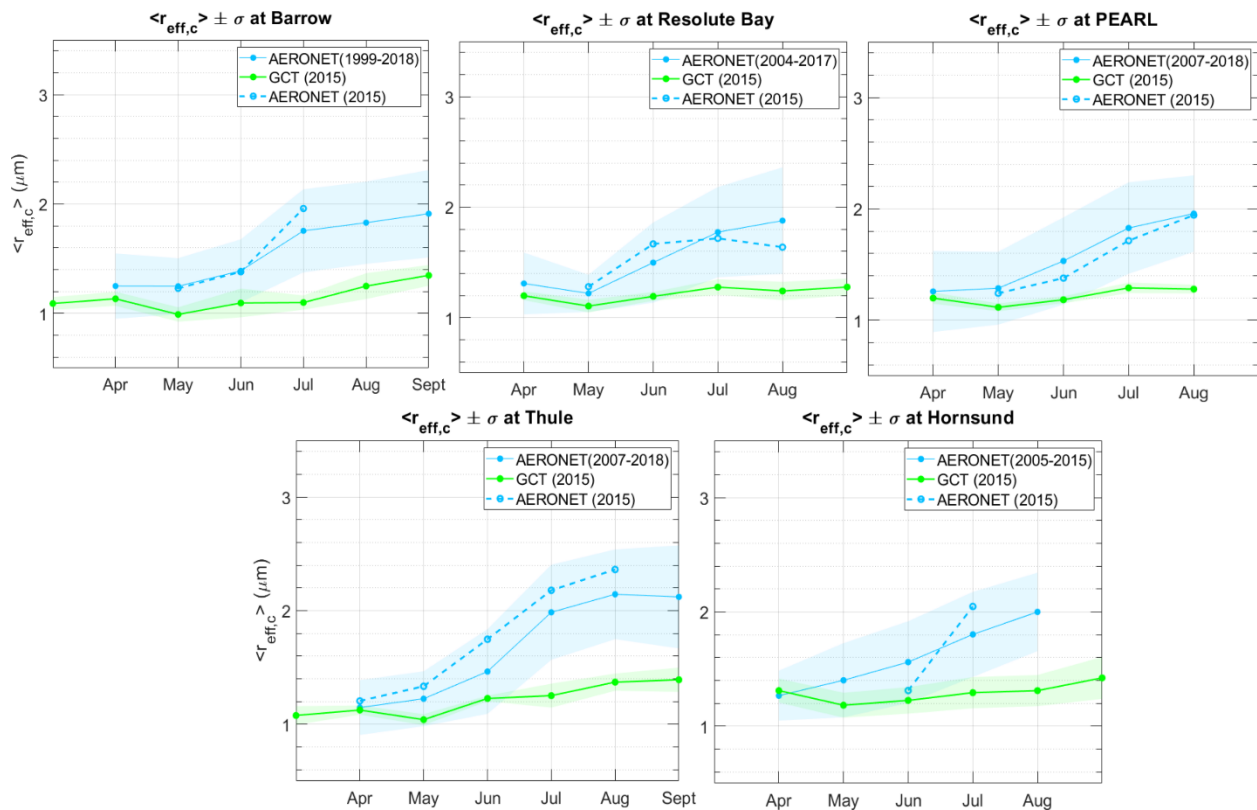


Figure 6 Seasonal $\langle r_{eff,c} \rangle$ variation for all five Arctic stations. Same caption as Figure 5 (with a color change of red to blue for the AERONET retrievals).

5. Conclusions

GCT simulations of AERONET-inversion products during 2015 were compared with the AERONET-inversions products from the multi-year climatology of AeF and event-level (2015)

AERONET products acquired over 5 stations in the North American and European Arctic. Monthly averaged (seasonal) analyses were carried out in the context of the spring to summer transition, the relatively stable summer period and the summer to early fall transition. A single year of GCT simulations was evaluated within the context of the geometrical/arithmetic means and geometrical/arithmetic standard deviations of AeF's climatology as well as the 2015 AERONET retrieval parameters. This process enabled a better understanding of the robustness of seasonal variations derived from the AERONET retrievals and how well single-year GCT simulations could be employed to predict (climatological-scale) variations across the Arctic. When the 2015 AERONET retrievals departed excessively from the AeF climatology we sought to better understand the nature of these departures and how a single year of GCT simulations could (i) help us understand the physical and optical dynamics of the AERONET (columnar) retrieval parameters at the event and climatological scale and (ii) understand any shortcomings of GCT in simulating those retrieval parameters.

GCT showed no significant spring to summer increase in the radius of the FM peak: an insensitivity that was likely due to a general GCT underestimation of smoke particle size. The small-sized (springtime) GCT CM peak feature (1.1 to 1.5 μm radius peak) is roughly coherent with the 1.3 μm (Asian dust) peak reported by AeF. The GCT PSDs did not appear to capture any element of the larger-sized (4 to 7 μm CM peaking) reported by AeF (who suggested that this was more likely to be due to local dust). The small-sized GCT CM peak feature tended to rapidly decrease in amplitude as the season progressed (a tendency that was coherent with the amplitude decrease of AeF's 1.3 μm peak). However, this decreasing-amplitude trend went through a reversal with amplitude increases at all stations in August and/or September. Those increases might have physical links to AeF's larger-sized (4 to 7 μm) CM peak feature in the fall months: i.e., similar types of CM particles where the GCT variations are restricted to lower radius sizes by the constraints of the PSD source functions (see Gong, 2003 and Zhang et al., 2013) for sea-salt and dust respectively) combined with the upper-bin limitation of 4.5 μm .

The 2015 GCT $\tau_{f,g}$ estimates were generally close to the seasonal AeF variations. GCT springtime biases of large amplitude (relative to the April AeF climatology) were thought to be linked to the simulated nature of the competition between accumulation FM increase in number density (Arctic haze) and its decrease in lifetime due to wet deposition. The July 2015 AERONET $\tau_{f,g}$ retrievals were, in general, significantly larger than the AeF climatology (as were the GCT simulations but considerably muted relative to the 2015 retrievals). GCT did not capture the higher frequency AERONET τ_f variations while the smoke AODs predicted by the NAAPS model were similar to the high frequency AERONET variations. This was likely attributable to the higher temporal resolution of NAAPS biomass burning emissions, the employment of assimilated AODs (and their general higher spatial resolution).

The GCT simulations and the 2015 AERONET $\tau_{c,g}$ retrievals showed a spring to summer decrease that was similar to the tendency that AeF ascribed to the diminishing influence of Asian dust. GCT showed a systematic late summer / fall (August or September) increase at all stations. This behavior was coherent with the increasing amplitude and/or radius position of the small-sized CM GCT peaks observed in the PSD analysis. The GCT FMF simulations largely followed AeF's seasonal trend of increasing FMF (a trend that was driven in both cases by the decreasing seasonal amplitude of $\tau_{c,g}$).

GCT $\langle r_{eff,f} \rangle$ values were underestimated relative to both AeF and the 2015 AERONET retrievals. It was argued that inadequate simulation of sub-grid coagulation smoke particles was a plausible reason for the underestimation and that an $\langle r_{eff,f} \rangle$ increase from the GCT to AERONET values for the heavy smoke month of July 2015 (for all stations) increased the GCT $\tau_{f,g}$ values to levels which were close to the AERONET $\tau_{f,g}$ retrievals. The 2015 AERONET $\langle r_{eff,c} \rangle$ values were generally close to the AeF climatology curve (a variation ascribed to the decreasing influence of the Asian dust CM peak and the increasing influence of the larger-radius 4 to 7 μm peak). Because GCT only captured the lesser amplitude increase in the small-sized CM peak in August / September, its seasonal increase corresponded to a significantly lesser rate than the AERONET retrievals.

The seasonal GCT (PSD, FM and CM) results reported in this paper are generally robust and sufficiently accurate to have a significant accuracy influence on aerosol, aerosol-cloud-interaction and radiative forcing models over the Arctic. A knowledge of the seasonal variation of smoke and dust optical depths will have important consequences on the simulations of the deposition impacts of absorbing aerosols on snow reflectance. The prediction of both extensive and intensive CM and FM parameters, as well as key features of the PSD, represent an advancement over the use of classical extensive and semi-extensive columnar parameters of AOD and (regression) Angstrom exponent that tend to be the source of evaluation of the opto-physical packages of current aerosol-cloud models.

Acknowledgments

We would like to express our gratitude to NSERC (National Sciences and Engineering Research Council) of Canada for CCAR funding via the NETCARE and PAHA projects and the DG funding of O'Neill as well as the CSA (Canadian Space Agency) for the SACIA (Signatures of Aerosol-Cloud Interaction over the Arctic) project funding (ESS-DA program). The support of AEROCAN (Environment Change and Climate Change Canada), AERONET (NASA/GSFC), and the operation staff at the five sites whose retrievals we employed are gratefully acknowledged. The resource support of Compute Canada/Calcul Quebec was also greatly appreciated. We thank the site-PIs for their effort in establishing and maintaining the AERONET/AEROCAN sites: Brent Holben for Thule and Hornsund, Grzegorz Karasinski and Piotr Glowacki for Hornsund, and Rick Wagener, Laurie Gregory, and Lynn Ma for Barrow, and Vitali Fioletov for Resolute Bay, Eureka., Data used in this study is available at the AERONET website.

Symbols and Acronym Glossary

AeF	Aboelfetouh et al. (2020)
AEROCAN	Federated Canadian subnetwork of AERONET run by Environment and Climate Change Canada (ECCC)
AERONET	Aerosol Robotic Network: World-wide NASA network of combined sunphotometer / sky-scanning radiometers manufactured by CIMEL Électronique. See http://aeronet.gsfc.nasa.gov/ for documentation and data downloads
AOD	Aerosol optical depth: The community uses "AOD" to represent anything from nominal aerosol optical depth which hasn't been cloud-screened to the conceptual (theoretical) interpretation of aerosol optical depth. In this paper we use it in the latter sense and apply adjectives as required.
BC	Black Carbon
CM	coarse mode (supermicron particle radius)
CTM	Chemistry Transport Model
FM	fine mode (submicron particle radius)
FMF	fine mode fraction
GC	GEOS(Goddard Earth Observing System)-Chem
m_p	Complex refractive index (where $p=r$ for the real part & $p=i$ for the imaginary).
MERRA-2	Modern-Era Retrospective analysis for Research and Application, Version 2
MYSP	Multi-year sampling Period (different for each station) for which we acquired AERONET/Dubovik retrieval products.
NAAPS	Navy Aerosol Analysis and Prediction system
NAAPS-RA	NAAPS Reanalysis
NETCARE	Network on Climate and Aerosols: Addressing key uncertainties in Remote Canadian Environments
NSERC	Natural Sciences and Engineering Research Council of Canada
OC	Organic carbon

PEARL	Polar Environmental Atmospheric Research Laboratory
PSD	particle size distribution (precisely, the volume particle size distribution)
RH	Relative humidity
SS	Sea-salt
GCT	GEOS-Chem-TOMAS (Two Moment Aerosol Sectional)
x	x = f or c (fine mode or coarse mode)
$\langle r_{eff,x} \rangle$	Arithmetic mean of the effective radii for monthly averaging bins
$\sigma(\tau_x)$	Arithmetic standard deviation for monthly averaging bins for AODs
$\sigma(r_{eff,x})$	Arithmetic standard deviation for monthly averaging bins for effective radii
$\tau_{x,g}$	Geometric mean for monthly averaging bins. $\tau_{x,g} = 10^{\langle \log \tau_x \rangle}$ (see Table 1 of O'Neill et al., 2000).
μ_x	Geometric standard deviation for monthly averaging bins. $\mu_x = 10^{\sigma(\log \tau_x)}$ (see Table 1 of O'Neill et al., 2000).

References

- Abbatt, J. P. D., Leaitch, W. R., Aliabadi, A. A., Bertram, A. K., Boivin-rioux, A., Bozem, H., et al. (2018). New insights into aerosol and climate in the Arctic, (October), 1–60.
- AboEl-Fetouh, Y., O'Neill, N. T., Ranjbar, K., Hesarak, S., Abboud, I., & Sobolewski, P. S. (2020). Climatological-Scale Analysis of Intensive and Semi-intensive Aerosol Parameters Derived From AERONET Retrievals Over the Arctic. *Journal of Geophysical Research: Atmospheres*, *125*(10), 1–19. <https://doi.org/10.1029/2019JD031569>
- Adams, P. J., & Seinfeld, J. H. (2002). Predicting global aerosol size distributions in general circulation models. *Journal of Geophysical Research Atmospheres*, *107*(19), 1–23. <https://doi.org/10.1029/2001JD001010>
- AMAP. (2017). *Snow, Water, Ice and Permafrost. Summary for Policy-makers. Arctic Monitoring and Assessment Programme (AMAP)*. Oslo, Norway. <https://doi.org/10.1029/2002WR001512>
- AMAP. (2021). Arctic Climate Change Update 2021: Key Trends and Impacts. Summary for Policy-makers. *Arctic Monitoring and Assessment Programme (AMAP)*. Tromsø, Norway: Arctic Monitoring and Assessment Programme (AMAP).
- Anderson, T. L., Wu, Y., Chu, D. A., Schmid, B., Redemann, J., & Dubovik, O. (2005). Testing the MODIS satellite retrieval of aerosol fine-mode fraction. *J. Geophys. Res.*, *110*(March), D18204. <https://doi.org/10.1029/2005JD005978>
- Bergstrom, R. W., Pilewskie, P., Russell, P. B., Redemann, J., Bond, T. C., Quinn, P. K., & Sierau, B. (2007). Spectral absorption properties of atmospheric aerosols. *Atmospheric Chemistry and Physics*, *7*, 5937–5943. <https://doi.org/https://doi.org/10.5194/acp-7-5937-2007>
- Bey, I., Jacob, D. J., Yantosca, R. M., Logan, J. A., Field, B. D., Fiore, A. M., et al. (2001). Global modeling of tropospheric chemistry with assimilated meteorology: Model description and evaluation. *Journal of Geophysical Research Atmospheres*, *106*(D19), 23073–23095. <https://doi.org/10.1029/2001JD000807>
- Bohren, C. F., & Huffman, D. R. (2004). *Absorption and Scattering of Light by Small Particles* (First publ). Weinheim: WILEY-VCH Verlag GmbH & Co. KGaA. <https://doi.org/10.1002/9783527618156>
- Bond, T. C., & Bergstrom, R. W. (2006). Aerosol Science and Technology Light Absorption by Carbonaceous Particles: An Investigative Review Light Absorption by Carbonaceous Particles: An Investigative Review. *Aerosol Science and Technology*, *40*(1), 27–67. <https://doi.org/10.1080/02786820500421521>
- Boucher, O., Randall, D., Artaxo, P., Bretherton, C., Feingold, G., Forster, P., et al. (2013a). *Clouds and Aerosols. In: Climate Change 2013: The Physical Science Basis. Contribution of Working Group I to the Fifth Assessment Report of the Intergovernmental Panel on Climate Change [Stocker, T.F., D. Qin, G.-K. Plattner, M. Tignor, S.K. Allen, J. Bos. Cambridge University Press, Cambridge, United Kingdom and New York, NY, USA. Retrieved from https://www.ipcc.ch/pdf/assessment-report/ar5/wg1/WG1AR5_Chapter07_FINAL.pdf*
- Boucher, O., Randall, D., Artaxo, P., Bretherton, C., Feingold, G., Forster, P., et al. (2013b). Clouds and aerosols. In T. F. Stocker, D. Qin, G.-K. Plattner, M. Tignor, S. K. Allen, J. Boschung, et al. (Eds.), *Climate Change 2013 the Physical Science Basis: Working Group I*

Contribution to the Fifth Assessment Report of the Intergovernmental Panel on Climate Change (Vol. 9781107057, pp. 571–658). Cambridge, United Kingdom and New York, NY, USA: Cambridge University Press. <https://doi.org/10.1017/CBO9781107415324.016>

- Boucher, Olivier. (2015). *Atmospheric Aerosols: Properties and Climate Impacts*. Springer Netherlands. <https://doi.org/10.1007/978-94-017-9649-1>
- Breider, T. J., Mickley, L. J., Jacob, D. J., Wang, Q., Fisher, J. a., Chang, R. Y.-W., & Alexander, B. (2014). Annual distributions and sources of Arctic aerosol components, aerosol optical depth, and aerosol absorption. *Journal of Geophysical Research: Atmospheres*, *119*(7), 4107–4124. <https://doi.org/10.1002/2013JD020996>
- Bullard, J. E., Matthew, B., Tom, B., John, C., Eleanor, D., Diego, G., et al. (2016). High latitude dust in the Earth system. *Reviews of Geophysics*, *54*, 447–485. <https://doi.org/10.1002/2016RG000518>. Received
- Chin, M., Diehl, T., Tan, Q., Prospero, J. M., Kahn, R. A., Remer, L. A., et al. (2019). Multi-decadal aerosol variations from 1980 to 2009 : a perspective from observations and a global model, 3657–3690. <https://doi.org/10.5194/acp-14-3657-2014>
- Croft, B., Wentworth, G. R., Martin, R. V., Leaitch, W. R., Murphy, J. G., Murphy, B. N., et al. (2016). Contribution of Arctic seabird-colony ammonia to atmospheric particles and cloud-albedo radiative effect. *Nature Communications*, *7*, 1–10. <https://doi.org/10.1038/ncomms13444>
- Croft, Betty, Martin, R. V, Leaitch, W. R., Tunved, P., Breider, T. J., D'andrea, S. D., & Pierce, J. R. (2016). Processes controlling the annual cycle of Arctic aerosol number and size distributions. *Atmos. Chem. Phys*, *16*, 3665–3682. <https://doi.org/10.5194/acp-16-3665-2016>
- Croft, Betty, Martin, R. V., Richard Leaitch, W., Burkart, J., Chang, R. Y. W., Collins, D. B., et al. (2019). Arctic marine secondary organic aerosol contributes significantly to summertime particle size distributions in the Canadian Arctic Archipelago. *Atmospheric Chemistry and Physics*, *19*(5), 2787–2812. <https://doi.org/10.5194/acp-19-2787-2019>
- Curci, G., Hogrefe, C., Bianconi, R., Im, U., Balzarini, A., Baró, R., et al. (2015). Uncertainties of simulated aerosol optical properties induced by assumptions on aerosol physical and chemical properties: An AQMEII-2 perspective. *Atmospheric Environment*, *115*, 541–552. <https://doi.org/10.1016/j.atmosenv.2014.09.009>
- Dick, W. D., Saxena, P., & McMurry, P. H. (2000). Estimation of water uptake by organic compounds in submicron aerosols measured during the Southeastern Aerosol and Visibility Study. *Journal of Geophysical Research*, *105*(D1), 1471–1479. <https://doi.org/10.1029/1999JD901001>
- Dubovik, O., & King, M. D. (2000). A flexible inversion algorithm for retrieval of aerosol optical properties from Sun and sky radiance measurements. *Journal of Geophysical Research: Atmospheres*, *105*(D16), 20673–20696. <https://doi.org/10.1029/2000JD900282>
- Dubovik, O., Holben, B., Eck, T. F., Smirnov, A., Kaufman, Y. J., King, M. D., et al. (2002). Variability of Absorption and Optical Properties of Key Aerosol Types Observed in Worldwide Locations. *Journal of the Atmospheric Sciences*, *59*(3), 590–608. [https://doi.org/10.1175/1520-0469\(2002\)059<0590:VOAAOP>2.0.CO;2](https://doi.org/10.1175/1520-0469(2002)059<0590:VOAAOP>2.0.CO;2)

- Eck, T. F., Holben, B. N., Reid, J. S., Sinyuk, a., Hyer, E. J., O'Neill, N. T., et al. (2009). Optical properties of boreal region biomass burning aerosols in central Alaska and seasonal variation of aerosol optical depth at an Arctic coastal site. *Journal of Geophysical Research: Atmospheres*, 114(11), 1–14. <https://doi.org/10.1029/2008JD010870>
- Gelaro, R., McCarty, W., Suárez, M. J., Todling, R., Molod, A., Takacs, L., et al. (2017). The modern-era retrospective analysis for research and applications, version 2 (MERRA-2). *Journal of Climate*, 30(14), 5419–5454. <https://doi.org/10.1175/JCLI-D-16-0758.1>
- Gong, S. L. (2003). A parameterization of sea-salt aerosol source function for sub- and super-micron particles, 17(4), 1–7. <https://doi.org/10.1029/2003GB002079>
- Groot Zwaaftink, C. D., Grythe, H., Skov, H., & Stohl, A. (2016). Substantial contribution of northern high-latitude sources to mineral dust in the Arctic. *Journal of Geophysical Research*, 121(22), 13,678–13,697. <https://doi.org/10.1002/2016JD025482>
- Hansen, James E. and Travis, L. D. (1974). Light Scattering in Planetary Atmospheres. *Space Science Reviews*, 16, 527–610. <https://doi.org/10.1007/BF00168069>
- Hesarakı, S., Neill, N. T. O., Lesins, G., Saha, A., Randall, V., Fioletov, V. E., et al. (2017). Comparisons of a Chemical Transport Model with a Four-Year (April to September) Analysis of Fine- and Coarse-Mode Aerosol Optical Depth Retrievals Over the Canadian Arctic. *Atmosphere-Ocean*, 55(4–5), 213–229. <https://doi.org/10.1080/07055900.2017.1356263>
- Hesarakı, S., O'Neill, N. T., Lesins, G., Saha, A., Randall, M., Fioletov, V. E., et al. (2017). Polar summer comparisons of a chemical transport model with a 4-year analysis of fine and coarse mode aerosol optical depth retrievals over the Canadian Arctic, (In press).
- Hinds, W. C. (1999). *Aerosol Technology: Properties, Behavior, and Measurement of Airborne Particles* (2nd Editio). John Wiley & Sons, Inc.
- Hirdman, D., Burkhardt, J. F., Sodemann, H., Eckhardt, S., Jefferson, A., Quinn, P. K., et al. (2010). Long-term trends of black carbon and sulphate aerosol in the Arctic: Changes in atmospheric transport and source region emissions. *Atmospheric Chemistry and Physics*, 10(19), 9351–9368. <https://doi.org/10.5194/acp-10-9351-2010>
- Holben, B. N., Eck, T. F., Slutsker, I., Tanré, D., Buis, J. P., Setzer, a., et al. (1998). AERONET - A federated instrument network and data archive for aerosol characterization. *Remote Sensing of Environment*, 66(1), 1–16. [https://doi.org/10.1016/S0034-4257\(98\)00031-5](https://doi.org/10.1016/S0034-4257(98)00031-5)
- Huang, J., & Jaeglé, L. (2017). Wintertime enhancements of sea salt aerosol in polar regions consistent with a sea ice source from blowing snow. *Atmospheric Chemistry and Physics*, 17(5), 3699–3712. <https://doi.org/10.5194/acp-17-3699-2017>
- IPCC. (2021). Summary for Policymakers. In: Climate Change 2021: The Physical Science Basis. Contribution of Working Group I to the Sixth Assessment Report of the Intergovernmental Panel on Climate Change. In V. Masson-Delmotte, P. Zhai, A. Pirani, S. L. Connors, C. Pean, S. Berger, et al. (Eds.). Cambridge University Press. In Press. <https://doi.org/10.1080/03736245.2010.480842>
- Kodros, J. K., & Pierce, J. R. (2017). Important global and regional differences in aerosol cloud-albedo effect estimates between simulations with and without prognostic aerosol

- microphysics. *Journal of Geophysical Research: Atmospheres*, 122(7), 4003–4018. <https://doi.org/10.1002/2016JD025886>
- Kodros, J. K., Hanna, S. J., Bertram, A. K., Leaitch, W. R., Schulz, H., Herber, A. B., et al. (2018). Size-resolved mixing state of black carbon in the Canadian high Arctic and implications for simulated direct radiative effect. *Atmospheric Chemistry and Physics*, 18(15), 11345–11361. <https://doi.org/10.5194/acp-18-11345-2018>
- Law, K. S., & Stohl, a. (2007). Arctic Air Pollution: Origins and Impacts. *Science*, 315(5818), 1537–1540. <https://doi.org/10.1126/science.1137695>
- Leaitch, R. R., Kodros, J. K., Willis, M. D., Hanna, S., Schulz, H., Andrews, E., et al. (2020). Vertical profiles of light absorption and scattering associated with black carbon particle fractions in the springtime Arctic above 79°N. *Atmospheric Chemistry and Physics*, 20(17), 10545–10563. <https://doi.org/10.5194/acp-20-10545-2020>
- Lesins, G., Chylek, P., & Lohmann, U. (2002). A study of internal and external mixing scenarios and its effect on aerosol optical properties and direct radiative forcing, 107.
- Najafi, M. R., Zwiers, F. W., & Gillett, N. P. (2015). Attribution of Arctic temperature change to greenhouse-gas and aerosol influences. *Nature Climate Change*, 5(3), 246–249. <https://doi.org/10.1038/nclimate2524>
- O’Neill, N. T., Eck, T.F., Smirnov, A, Holben, B.N., and Thulasiraman, S. (2003). Spectral discrimination of coarse and fine mode optical depth. *Journal of Geophysical Research*, 108(D17), 1–15. <https://doi.org/10.1029/2002JD002975>
- O’Neill, N. T., Ignatov, A., Holben, B. N., & Eck, T. F. (2000). The lognormal distribution as a reference for reporting aerosol optical depth statistics; Empirical tests using multi-year, multi-site AERONET Sunphotometer data. *Geophysical Research Letters*, 27(20), 3333–3336. <https://doi.org/10.1029/2000gl011581>
- O’Neill, N. T., Eck, T. F., Holben, B. N., Smirnov, A., Dubovik, O., & Royer, A. (2001). Bimodal size distribution influences on the variation of Angstrom derivatives in spectral and optical depth space. *Journal of Geophysical Research: Atmospheres*, 106(D9), 9787–9806. <https://doi.org/10.1029/2000JD900245>
- O’Neill, N T, Eck, T. F., Holben, B. N., Smirnov, A., & Dubovik, O. (2001). Bimodal size distribution influences on the variation of Angstrom derivatives in spectral and optical depth space. *Journal of Geophysical Research*, 106(D9), 9787–9806. <https://doi.org/10.1029/2000JD900245>
- O’Neill, Norm T., Thulasiraman, S., Eck, T. F., & Reid, J. S. (2005). Robust optical features of fine mode size distributions: Application to the Qu??bec smoke event of 2002. *Journal of Geophysical Research D: Atmospheres*, 110(11), 1–16. <https://doi.org/10.1029/2004JD005157>
- O’Neill, Norm T., Pancrati, O., Baibakov, K., Eloranta, E., Batchelor, R. L., Freemantle, J., et al. (2008). Occurrence of weak, sub-micron, tropospheric aerosol events at high Arctic latitudes. *Geophysical Research Letters*, 35(14). <https://doi.org/10.1029/2008GL033733>
- Ramnarine, E., Kodros, J. K., Hodshire, A. L., Lonsdale, C. R., Alvarado, M. J., & Pierce, J. R. (2019). Effects of near-source coagulation of biomass burning aerosols on global predictions of aerosol size distributions and implications for aerosol radiative effects. *Atmospheric*

- Chemistry and Physics*, 19(9), 6561–6577. <https://doi.org/10.5194/acp-19-6561-2019>
- Ranjbar, K., O'Neill, N. T., AboEl-fetouh, Y., Lutsch, E., Lesins, G., McCullough, E., et al. (2019). Extreme smoke event over the high Arctic. *Submitted to Atmospheric Environment*.
- Saha, A., O'Neill, N. T., Eloranta, E., Stone, R. S., Eck, T. F., Zidane, S., et al. (2010). Pan-Arctic sunphotometry during the ARCTAS-A campaign of April 2008. *Geophysical Research Letters*, 37(5), 1–7. <https://doi.org/10.1029/2009GL041375>
- Sayer, A. M., & Knobelspiesse, K. D. (2019). How should we aggregate data ? Methods accounting for the numerical distributions , with an assessment of aerosol optical depth. *Atmospheric Chemistry and Physics, Discussions*, (July), 1–36.
- Schmale, J., Zieger, P., & Ekman, A. M. L. (2021). Aerosols in current and future Arctic climate. *Nature Climate Change*, 11(February). <https://doi.org/10.1038/s41558-020-00969-5>
- Seinfeld, J. H., & Pandis, S. N. (2006). *Atmospheric Chemistry and Physics: From Air Pollution to Climate Change* (2nd editio). John Wiley & Sons, Inc.
- Sinyuk, A., Holben, B. N., Eck, T. F., Giles, D. M., Slutsker, I., Korkin, S., et al. (2020). The AERONET Version 3 aerosol retrieval algorithm, associated uncertainties and comparisons to Version 2. *Atmos. Meas. Tech*, 13, 3375–3411. <https://doi.org/10.5194/amt-13-3375-2020>
- Sioris, C. E., Abboud, I., Fioletov, V. E., & McLinden, C. A. (2017). AEROCAN, the Canadian sub-network of AERONET: Aerosol monitoring and air quality applications. *Atmospheric Environment*, 167, 444–457. <https://doi.org/10.1016/j.atmosenv.2017.08.044>
- Sirois, A., & Barrie, L. A. (1999). Arctic lower tropospheric aerosol trends and composition at Alert , Canada : 1980-1995. *Journal of Geophysical Research*, 104(D9), 11599–11618. <https://doi.org/https://doi.org/10.1029/1999JD900077>
- Slater, T., Hogg, A. E., & Mottram, R. (2020). Ice-sheet losses track high-end sea-level rise projections. *Nature Climate Change*, 10(10), 879–881. <https://doi.org/10.1038/s41558-020-0893-y>
- Stone, R. S., Anderson, G. P., Andrews, E., Dutton, E. G., Shettle, E. P., & Berk, A. (2007). Incursions and radiative impact of Asian dust in northern Alaska, 34(March), 1–5. <https://doi.org/10.1029/2007GL029878>
- Stone, R. S., Sharma, S., Herber, A., Eleftheriadis, K., & Nelson, D. W. (2014). A characterization of Arctic aerosols on the basis of aerosol optical depth and black carbon measurements. *Elementa: Science of the Anthropocene*, 2, 1–22. <https://doi.org/10.12952/journal.elementa.000027>
- Tang, I. N. (1996). Chemical and size effects of hygroscopic aerosols on light scattering coefficients. *Journal of Geophysical Research*, 101(D14), 19245. <https://doi.org/10.1029/96JD03003>
- Tegen, I., & Fung, I. (1994). Modeling of mineral dust in the atmosphere: Sources, transport, and optical thickness. *Journal of Geophysical Research*, 99(D11), 22,897-22,914. <https://doi.org/10.1029/94JD01928>
- Tomasi, C., Kokhanovsky, A. A., Lupi, A., Ritter, C., Smirnov, A., O'Neill, N. T., et al. (2015). Aerosol remote sensing in polar regions. *Earth-Science Reviews*, 140, 108–157.

<https://doi.org/10.1016/j.earscirev.2014.11.001>

- Trivitayanurak, W., Adams, P. J., Spracklen, D. V., & Carslaw, K. S. (2008). Tropospheric aerosol microphysics simulation with assimilated meteorology: model description and intermodel comparison. *Atmospheric Chemistry and Physics Discussions*, 7(5), 14369–14411. <https://doi.org/10.5194/acpd-7-14369-2007>
- Udisti, R., Traversi, R., Becagli, S., Tomasi, C., Mazzola, M., Lupi, A., & Quinn, P. K. (2020). Arctic Aerosols. In A. Kokhanovsky & C. Tomasi (Eds.), *Physics and Chemistry of the Arctic Atmosphere* (pp. 209–329). Springer Polar Sciences. Springer, Cham. https://doi.org/10.1007/978-3-030-33566-3_4
- Xie, Y., Li, Z., Li, L., Wagener, R., Abboud, I., Li, K., et al. (2018). Aerosol optical, microphysical, chemical and radiative properties of high aerosol load cases over the Arctic based on AERONET measurements. *Scientific Reports*, 8(1), 1–9. <https://doi.org/10.1038/s41598-018-27744-z>
- Zhang, X., Huang, Y., Rao, R., & Wang, Z. (2013). Retrieval of effective complex refractive index from intensive measurements of characteristics of ambient aerosols in the boundary layer. *Optics Express*, 21(15), 17849–62. <https://doi.org/10.1364/OE.21.017849>
- Zielinski, T., Bolzacchini, E., Cataldi, M., Ferrero, L., Graßl, S., Hansen, G., et al. (2020). Study of chemical and optical properties of biomass burning aerosols during long-range transport events toward the arctic in summer 2017. *Atmosphere*, 11(1). <https://doi.org/10.3390/ATMOS11010084>

4. Conclusions

We reported a number of significant seasonal (climatological-scale) findings in terms of the microphysical and optical AERONET-retrieved properties of Arctic aerosols and their simulation with GCT. This work has contributed to a deeper understanding of the seasonal (spring to fall) trends and features of these properties. It also shed light on deficiencies present in the GCT simulations utilized in this study. Finally, we note that this process has played a role in model development through the collaboration, discussions, and information exchanged between our remote sensing group and the GCT modellers.

4.1 Challenges and limitations

One of the most obvious limitations in this study is the lack of availability of winter retrievals suitable for a climatological-scale study of a full polar year. The current CIMEL (“triplet”) photometers of the AERONET network incorporate a moon photometer feature alongside the standard sunphotometer / sky radiance capability. The network is currently providing year-round measurements across a subset AERONET stations (in what amounts to a test mode because the moon photometers do have their own set of unique start-up problems: not the least of which are problems related to their limited nighttime sampling time). In the long run, this should enable year-long, Arctic climatology investigations. A second limitation is the occasional lack of consistency of AERONET retrievals relative to issues such as cloud screening shortcomings (false positive and false negative clouds for example), statistical processing sensitivities (arithmetic vs geometric statistics for example) and low sample numbers (in the face of excessively overcast conditions or early spring and late fall low-sun conditions in the Arctic for example).

The coarse $4^\circ \times 5^\circ$ spatial resolution of GCT prevented the model from capturing processes occurring at a subgrid dimensions such as the coagulation of smoke particles, the drainage flow of small-size dust-generating basins in the Arctic and the accurate capture of forest fire smoke emissions (Paper 2). The GCT upper-limit radius of $\sim 4.5 \mu\text{m}$ limits the study of larger CM particles (particles, such as local dust, that can play an important role in the Arctic aerosol budget).

4.2 Recommendations and future work

This work has inspired further ideas towards exploring other research venues. A full year of microphysical and optical properties from AERONET retrievals was studied using a mix of both moon/star photometers and sunphotometers (study carried out in parallel with our climatological-scale study). An analysis of this data will be beneficial in terms of understanding the FM & CM continuity (for both extensive and intensive parameters) of Arctic aerosols over a full polar year. We hope to leverage our current findings in order to pursue such a study.

Another interesting model-comparison investigation involves simulations of optical and microphysical vertical profiles. Profiles of GCT-generated speciated extinction coefficient and effective radius compared with ground- and satellite-based lidar profiles as well as photometric retrievals during the whole polar year will undoubtedly add insight to our understanding of the polar dome dynamics of Arctic aerosols. Other potential investigations include a comparison between GCT-derived and AERONET-retrieved PSDs contextualized by GEOS-Chem wind vectors during the spring and fall sea-salt season. Other potential studies include comparisons of GCT-derived dust PSDs, surface-level PSDs and PSDs from AERONET retrievals.

Appendix A: Some theoretical foundations of aerosol physics and optics

A.1 Basic Aerosol Physics

In this section, parameters describing the optical and microphysical properties of aerosols will be briefly explained.

1. Aerosol Microphysics

1.1 Particle Size Distribution

Particle size is a critical extensive parameter which, short of the refractive index and particle shape indicators, characterizes all important contributions to aerosol optics (see section 2). The **particle size distribution** (PSD) can be expressed in terms of a number of related equations. For the purposes of this research project, we will be using the following expression:

$$\frac{dV(r)}{d\ln r} = \frac{4}{3}\pi r^3 \frac{dN(r)}{d\ln r} \quad (\text{A.1})$$

where r is the particle radius and $\frac{dV(r)}{d\ln r}$ describes the particle-volume distribution (volume of all particles of radius r in an incremental bin of extent $d\ln r$ per unit volume of air per unit increment in $\ln r$) and $\frac{dN(r)}{d\ln r}$ is the particle-number of all particles of radius r in an incremental bin of extent $d\ln r$ per unit volume of air per unit increment in $\ln r$. Figure 1 shows the number and volume PSDs (as a function of \log_{10} (diameter) rather than $\ln r$).

In the upper panel of Figure (1), the y-axis shows the particle-number distribution while the lower graph shows the particle-volume distribution for different naturally occurring aerosol modes (the nucleation and Aitken mode in the upper graph and the accumulation and coarse mode in the lower graph). The figure vividly demonstrates that the smaller and larger radius modal features appear lognormal (normal distribution on a log diameter axis) as particle-number and particle-volume distributions, respectively. Aerosol optics in the visible and near-IR spectral regions tend to be more closely aligned with the particle-volume distribution: it is a better representation of the strength of scattering and absorption contributions across all particle sizes (see Hansen & Travis, 1974, for a discussion of the relations between fundamental optical parameters and the size distribution). Optical parameters in the visible and near-IR spectral regions are thus largely dominated by the accumulation and coarse mode particle-volume distributions. It is important to note that typical fine mode peaks

are roughly between 0.1 and 0.2 μm : this is not the case in Figure 1 (the “droplet Submode” chosen by the authors was representative of high humidity, “cloud or fog conditions”).

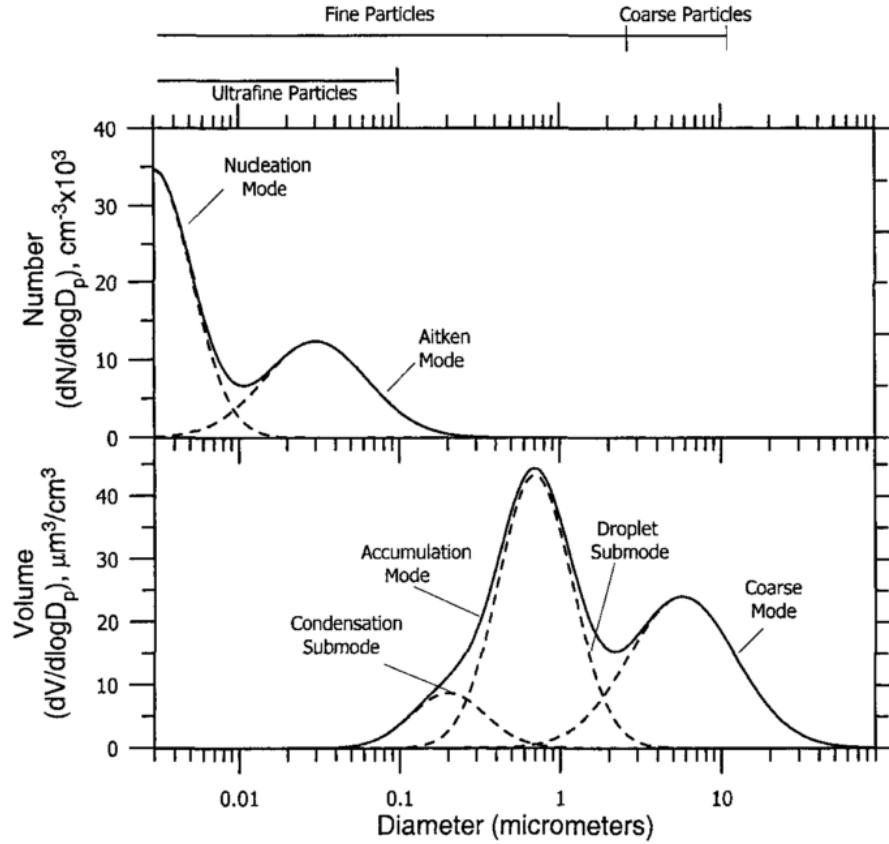


Figure 1 Particle-number and particle-volume distributions of the four different naturally occurring modes. Source: (Seinfeld et Pandis, 2006)

1.2 Effective Radius

The **effective radius**, r_{eff} , can be defined as (Boucher, 2015)

$$r_{\text{eff}} = \frac{\int \pi r^3 N(r) dl nr}{\int \pi r^2 N(r) dl nr} \quad (\text{A.2})$$

where $dN/dl nr$ is defined after equation (A.1). This commonly used parameter is actually an approximation to an optically weighted PSD average (compare equations (2.52) and (2.53) of Hansen & Travis, 1974).

2. Aerosol Optics

2.1 Refractive Index

The **refractive index, RI**, is a fundamental optical parameter that, along with the size and shape of a given particle determines all optical properties of that particle. The optical properties of a PSD in a small (differential) volume or a column of the atmosphere are dependent on the ensemble refractive indices of all the particles in the small volume or column. It is a complex number whose value is dependent on the nature (chemical composition and structure) of the particle (or particles in a PSD). Its imaginary part determines the degree of absorption whereas the real part determines the degree of scattering (Boucher, 2015). The complex refractive index is often written as $\hat{m} = m_r - m_i i$ where $i = \sqrt{-1}$ and m_r and m_i are real and imaginary parts.

2.2 Extinction Coefficient

Extensive parameters, varying as they do with the quantity (number) of particles are often highly variable in space and time. The most fundamental extensive parameters are the point (small volume) dependent volume scattering, absorption and extinction coefficients (see Hansen & Travis, 1974 for example). They account for, respectively, the fraction of light per unit length that is scattered out of (out scattered), absorbed, and removed by both processes from a beam incident at any point in the atmosphere. The extinction coefficient, k_{ext} is accordingly expressed as the sum:

$$k_{ext} = k_{scatt} + k_{abs} \quad (\text{A.3})$$

with typical units of km^{-1} . The scattering, absorption, and extinction coefficients can be broken down into their aerosol and molecular (Rayleigh) components (ibid). The latter coefficients are reasonably well known in terms of molecular scattering given the weak (and predictable) variability of the major molecular components of the earth's atmosphere (largely N_2 and O_2). The aerosol analogue of the extinction coefficient equation can be written as:

$$k_{ext,a} = k_{scatt,a} + k_{abs,a} \quad (\text{A.4})$$

The extinction coefficient is given by equation (2.48) of Hansen & Travis (1974) adapted for our “ln” based definition of the PSD;

$$k_{ext} = \int_{r_1}^{r_2} \sigma_{ext}(r, \hat{m}) \frac{dN(r)}{dlnr} dlnr = \int_{r_1}^{r_2} \pi r^2 Q_{ext}(r) \frac{dN(r)}{dlnr} dlnr \quad (\text{A.5})$$

where $\sigma_{ext}(r, \hat{m})$ is the (intensive parameter) scattering cross section (units of area) and r_1 and r_2 represent the radius limits of the PSD. $Q_{ext}(r, \hat{m})$ is the extinction efficiency given by $\sigma_{ext}(r, \hat{m})/\pi r^2$.

2.3 Optical Depth and Aerosol Optical Depth

Optical depth represents the integrated contributions of the extinction coefficient in the vertical direction:

$$\tau = \int_0^{\infty} k_{ext}(z) dz \quad (\text{A.6})$$

where z is the altitude, the upper limit of ∞ corresponds to the altitude at which all significant molecular and particulate (scattering and absorption) contributions are accounted for (approximately above the stratospheric ozone layer) and “0” is the altitude of above ground level (AGL) at the location of the τ -measuring instrument. In effect $k_{ext}(z)dz$ represents the fraction of energy lost, from a beam of radiance L , to scattering and absorption across an altitude interval of dz ($dL/L = dT = -k_{ext}(z)dz = -d\tau$) so that the transmission from a source outside the atmosphere to the surface¹ is $T = e^{-\tau}$. Note that the 3D to 1D reduction in dimensionality in the spatial dependency of $k_{ext}(z)$ means that we are assuming horizontal homogeneity in the local atmosphere.

As per the total extinction coefficient the AOD can be written as;

$$\tau_a = \int_0^{\infty} k_{ext,a}(z) dz \quad (\text{A.7})$$

$$\tau_a = \int_0^{\infty} \int \sigma_{ext,a}(r) \frac{dN(z)}{d \ln r} d \ln r dz \quad (\text{A.8})$$

where we have inserted equation (A.5) into equation (A.7). The AOD is a spectrally varying parameter whose amplitude is largely controlled by the integrated (columnar) number density of aerosols and whose spectral shape is controlled by the size and nature (refractive index) of the aerosols in a given vertical column.

The right-hand side of this equation can be reduced to columnar PSD form by averaging the extinction cross section over radius and altitude;

$$\tau_a = \overline{\overline{\sigma_{ext,a}}} A \quad (\text{A.9})$$

¹ Letting dz be positive for this particular integration which is opposite the direction of increasing altitude (but, rather than getting bogged down with signs, the point to retain is that there must be an energy loss from absorption and out-scattering).

where the radius averaged extinction cross section is given by,

$$\overline{\sigma_{ext,a}(z)} = \frac{\int \sigma_{ext,a}(r) \frac{dN(z)}{d \ln r} d \ln r}{N(z)} \quad (\text{A.10})$$

so that

$$\begin{aligned} \tau_a &= \int_0^\infty \overline{\sigma_{ext,a}(z)} N(z) dz \\ &= \overline{\overline{\sigma_{ext,a}}} \int_0^\infty N(z) dz \\ &= \overline{\overline{\sigma_{ext,a}}} A \end{aligned} \quad (\text{A.11})$$

where A , the abundance² (integrated number density);

$$A = \int_0^\infty N(z) dz \quad (\text{A.12})$$

and the doubly averaged extinction cross section is given by;

$$\overline{\overline{\sigma_{ext,a}}} = \frac{\int_0^\infty \overline{\sigma_{ext,a}(z)} N(z) dz}{A} \quad (\text{A.13})$$

2.4 AOD Components

The aerosol volume PSD, in terms of optical impact, can be divided into fine and coarse (sub and super-micron) size distributions that are typically associated with different aerosol types and origins (O'Neill et al., 2001). If one accepts the premise that aerosols are essentially bi-modal (at least as far as their visible and near-IR optical effects are concerned) then the total AOD at a reference wavelength can be written (ibid);

$$\tau_a = \tau_f + \tau_c \quad (\text{A.14})$$

where τ_f and τ_c represent the (extensive parameter) fine and coarse mode optical depths. A common and useful parameter employed in the literature is the fine mode fraction (FMF) given by, $FMF = \frac{\tau_f}{\tau_a}$.

If one assumes a continuous analytical spectral form for τ_a (typically a higher order polynomial of $\ln \tau_a$ vs $\ln \lambda$) then this optical bi-modality leads to a bi-modality of (intensive parameter) spectral derivatives (α_f and α_c) and their spectral derivatives (α_f' and α_c'), etc. at a single reference wavelength (O'Neill et al., 2001). Those spectral parameters lead to estimates of fine and coarse mode effective radii (O'Neill et al., 2008a and O'Neill et al., 2008b). The total spectral derivative employed in this formulation is, from equation (14) :

² with units of number of particles per unit area

$$\alpha(\lambda) = - \frac{d \ln \tau_a(\lambda)}{d \ln \lambda} = \alpha_f + \alpha_c \quad (\text{A.15})$$

With this formulation, there are no regression approximations across multiple bands as per the classical Angstrom exponent (see section 2.5): in effect the classical Angstrom exponent is a 1st order approximation of the exact spectral derivatives across the wavelength range of the former.

2.5 The Classical Ångström Exponent

The Ångström exponent (\mathring{a}) is the classical first order expression of the variation of τ_a as a function of wavelength. For a minimalist spectrum of two optical depths, \mathring{a} can be expressed as;

$$\mathring{a} = - \frac{\ln(\tau_1/\tau_2)}{\ln(\lambda_1/\lambda_2)} \quad (\text{A.16})$$

The standard regression expression replaces this equation for more than two optical depths. As suggested by the previous section, \mathring{a} is a first order indicator of particle size (the higher its value the smaller the particle).

The form of the Angstrom relation, given the presumption of first order spectral dependency in log-log space, is:

$$\tau_a(\lambda) = \beta \lambda^{-\mathring{a}} \quad (\text{A.17})$$

A.2 GCT equations – Technical Memo

Extractions from a technical document prepared by Norm O'Neill (O'Neill, N. T., Basic physics of TOMAS computations, Département de Géomatique Appliquée Technical memo, Université de Sherbrooke, 2021). Expressions in [] in any affirmation is not attributed to the referenced citation and is solely the author's opinion.

These notes were written to give some theoretical background to the TOMAS code whose comprehensive scientific documentation seems to be lacking and to the web sites that seem to specialize in giving “formulae” with little apparent context (see [this example](#) on the GEOS-Chem wiki, for example). In order to keep the equations simple there is no explicit subscript to indicate aerosol species until such a subscript is absolutely necessary (whenever mass density or abundance is converted to volume / projected-area density or abundance). Those equations without an aerosol species index apply to individual aerosol species as well as to the total aerosol. The subscript “a” for aerosol was also, again for simplicities sake, suppressed.

1. TOMAS

Adams and Seinfeld (2002) were the original formulators of TOMAS¹ (Two –Moment Aerosol Sectional). They made clear what the two “moments” referred to (aerosol number and mass)²

2. Mass density, mass abundance and specific gas constant

If m is the mass density (kg-m⁻³) and mmr is the mass mixing ratio of a given aerosol species then;

$$m = mmr \rho_{air} \quad (1)$$

Using the ideal gas law ($PV = n RT$ where n is the number of moles of air molecules in the volume V and R is the universal, per mole, gas constant³) it is easy to show that $\rho_{air} = PW_{air} / RT$) and so;

$$m = mmr \frac{P W_{air}}{RT} \quad (2)$$

where W_{air} is the molecular weight (mass of one mole) of humid air at altitude z^4 . The column mass density or mass abundance (kg-m⁻²) is;

¹ Kodros & Pierce (2017), for example, refer to that paper

² See their equations (1) and (2) that are employed to define those two moments

³ the familiar value of 8.314 J-mole⁻¹-K⁻¹ (see, for example, Tsonis, 2002 ... with the warning that he uses R^* rather than the more familiar R for the universal gas constant)

⁴ $W_{air,d}$ would represent the molecular weight of a mole of dry air (0.02897 kg/mole is the Wikipedia entry).

$$A_m = \int m dz = \int mmr \rho_{air} dz \quad (3)$$

where the integral is from the surface to the top of the aerosol atmosphere. Assuming the hydrostatic approximation⁵ ($dP = -\rho_{air}g dz$) we can reformulate equation (3) as;

$$A_m = \int mmr \frac{-dP}{g} \quad (4)$$

and thus, the mmr integration can be accomplished over pressure levels.

TOMAS employs a specific, gas dependent variant of R. Dividing R by W_{air} equation (2), we can write

$$m = mmr \frac{P}{R_{specific}T} \quad (5)$$

where;

$$R_{specific} = \frac{R}{W_{air}} \quad (6)$$

so that $R_{specific}$ varies as $\frac{1}{W_{air}}$ or hence with the specific molecular constituents of air, including water vapour (some authors, notably, Tsonis, 2002, use R^* for the universal gas constant and R for the specific gas constant!). Tsonis (2002) gives an explicit expression (his equation (7.10)) for the specific gas constant;

$$R_{specific} = (1 + 0.61 q) R_{specific,d} \quad (7a)$$

where $R_{specific,d}$ is the specific gas constants for dry air. Letting the subscript "wv" indicate water vapour (gas of H₂O molecules) Tsonis defines;

$$q = \frac{m_{wv}}{m_{wv} + m_d} \quad (7b)$$

⁵ See Tsonis (2002)

The number 0.61 is actually $= 1/\epsilon - 1$ (ibid) where;

$$\epsilon = \frac{R_{specific,d}}{R_{specific,v}} \quad (7c)$$

3. On the GCT use of *mmr*

What GCT actually uses as “mass” is the mass mixing ratio ($mmr = m / \rho_{air}$ as defined above) with “units” of $([\text{kg of aerosol} / \text{m}^3 \text{ of air}] / [\text{kg of air} / \text{m}^3 \text{ of air}]) \rightarrow \text{kg of aerosol} / \text{kg of air}$ ⁶. The analogue volume mixing ratio can be defined as

$$vmr = v / \rho_{air} = (m / \rho) / \rho_{air} = mmr / \rho \quad (8a)$$

with consistent units of $\text{m}^3 \text{ of aerosol} / \text{kg of air}$ ⁷. If n is the traditional number density (# of aerosols / $\text{m}^3 \text{ of air}$), it follows that the analogue number density in terms of kg of air units is

$$nmr = n / \rho_{air} \quad (8b)$$

with units of $\# \text{ of aerosols} / \text{m}^3 \text{ of air}] / [\text{kg of air} / \text{m}^3 \text{ of air}] \rightarrow \# \text{ of aerosols} / \text{kg of air}$.

The quantity of average volume per aerosol particle for a number density of n is then;

$$\langle v \rangle_p = v / n = v / \rho_{air} / (n / \rho_{air}) = vmr / nmr = \frac{mmr / nmr}{\rho} \quad (8c)$$

The GCT *xmr* standard and the more common mks standard of x density are easily interconverted using the transformation of $xmr = x / \rho_{air}$ for any parameter “ x ”.

4. Optical computations⁸

The starting point for the case of internally mixed GCT aerosols is the fundamental (spherical particle) optical equation for the extinction coefficient⁹ expressed in terms of the optical and

⁶ Kudros (2017) for an explicit statement in terms of units and confirmed from a units analysis of the GCT AOD code (i.e., a units analysis that yielded meters for $\langle r \rangle_p$ of equation (9d))

⁷ Taking the first expression for the units we have $[\text{m}^3 \text{ of aerosol} / \text{m}^3 \text{ of air}] / [\text{m}^3 \text{ of air} / \text{m}^3 \text{ of air}]$

⁸ This section was updated when the optical calculation details of the GCT code (notably “`bystation_AOD_GCT.py`”) were explored in detail (and the previous, more general theoretical section was exiled to the “Differential details of equation (12)” section of the Appendix).

⁹ The reader is referred to a fundamental aerosol reference such as Hansen & Travis (1976) for the basic optical definitions.

microphysical values in a given GCT grid cell (given height layer, given log radius bin, given lat. / long. at a given time);

$$\begin{aligned} \frac{d\tau_{int}}{dz} &= Q_{int}(\langle\eta\rangle_v, \langle r\rangle_p, \lambda) \pi\langle r\rangle_p^2 \frac{dn}{d\log r}(\langle r\rangle_p, z_L) \Delta\log r \quad (9a) \\ &= Q_{int} \pi\langle r\rangle_p^2 \Delta n \end{aligned}$$

where $\langle\eta\rangle_v$ is the complex refractive index weighted by the volume concentrations of all internally mixed aerosols, $\langle r\rangle_p$ is the arithmetically averaged per-particle radius across all aerosol species, z_L is the layer height, Q_{int} is the unitless extinction efficiency, $\sigma_{int} = Q_{int}\pi\langle r\rangle_p^2$ is the extinction cross section, $\Delta\log r$ refers to a *log r* change in a given GCT bin and Δn refers to the number density associated with that bin¹⁰ (“num_inc” in the key GCT code of `bystation_AOD_GCT.py`). Because there is plethora of differentials involved in the multi-dimensional GCT computations (and to maintain a closer correspondence with the GCT code nomenclature) we jettison the differential portion of the Δn nomenclature (we replace Δn by n) and simply write the above equation as;

$$\frac{d\tau_{int}}{dz} = Q_{int} \pi\langle r\rangle_p^2 n = Q_{int} \pi\langle r\rangle_p^2 \rho_{air} nmr \quad (9b)^{11}$$

where we have employed equation (8b) and where $n = \sum n_j$ (and $nmr = \sum nmr_j$) in the context of an ensemble of aerosol species (j) composing internally mixed particles. The critical intensive parameters for computing Q_{int} are the refractive index $\langle\eta\rangle_v$ and $\langle r\rangle_p$. For a volume weighted refractive index and a collection of spherical particles, we can, using equation (8c) above, to respectively write;

$$\langle\eta\rangle_v = \frac{\sum v_j \eta_j}{\sum v_j} = \frac{\sum vmr_j \eta_j}{\sum vmr_j} = \frac{\sum mmr_j / \rho_j \eta_j}{\sum mmr_j / \rho_j} \quad (9c)$$

$$\langle r\rangle_p = \left(\frac{3}{4} \frac{1}{\pi} \langle v\rangle_p \right)^{\frac{1}{3}} = \left(\frac{3}{4} \frac{1}{\pi} \frac{\sum vmr_j}{nmr} \right)^{\frac{1}{3}}$$

¹⁰ For the sake of simplicity, we limit the use of the internally mixed subscript (“int”) and, in equation (9b), minimize the dependent variable arguments.

¹¹ With units of [m² or aerosol radius] [# of aerosols / m³ of air] or hence the usual mks units of extinction coefficient (m⁻¹)

$$= \left(\frac{3}{4} \frac{1}{\pi} \frac{\sum m m r_j / \rho_j}{n m r} \right)^{1/3} \quad (9d)$$

Variants of these internally mixed calculations¹² follow the same general procedure.

4.1 Normalized extinction coefficient of the GCT AOD code

All equations above are as in the GCT AOD code (available in Appendix B) except the extinction coefficient of equation (9a) which is taken explicitly as equation (9b) without the ρ_{air} factor, viz;

$$\frac{d\tau_{int}}{dz} \frac{1}{\rho_{air}} \quad (9e)$$

Using the hydrostatic equation ($dP = -\rho_{air} g dz$), this normalized extinction coefficient is readily converted to optical depth increment;

$$d\tau_{int} = \left(\frac{d\tau_{int}}{dz} \frac{1}{\rho_{air}} \right) \rho_{air} dz \quad (9f)$$

$$= \left(\frac{d\tau_{int}}{dz} \frac{1}{\rho_{air}} \right) \frac{dP}{g} \quad (9g)$$

which is exactly what is done in the “tau” calculation in the `bystation_AOD_GCT.py` code (where the coefficients “b” [variables starting with “babs” and “bsca”] are the equivalent of $\left(\frac{d\tau_{int}}{dz} \frac{1}{\rho_{air}} \right)$ and all the multiplicative terms represent $\frac{dP}{g}$)¹³.

4.2 Aerosol water

We note that the list of aerosol “species” includes “aerosol water” : the GCT estimation of water mass that has condensed on all hydrophilic aerosols. This means, for example, that the species summation of equations (9c) and (9d) can be expressed in a more explicit form as respectively;

¹² Such as the distinct cases of extensive (ext) aerosols, the combination of int and ext aerosols, fine mode aerosols, coarse mode aerosols, etc.

¹³ For e.g., `'bsca_int = reff_int ** 2 * np.pi * num_int * qsca_int'` is, of course, a scattering coefficient with the nuance that `num_int` is actually `nmr` (ρ_{air} -normalization) and `"np.pi"` is a python representation of π . “Multiplicative terms” refers to all the TOMAS-layer OD products of the associated expression (`"tau_sca_int = bsca_int * pressure[t, l] / grav * 100. * np.log(prese[l] / prese[l + 1])"`). `"prese"` is a constant matrix of pressures employed for those (sigma) unitless pressures.

$$\sum vmr_{j,wet} \eta_j = vmr_w \eta_w + \sum_{not\ w} vmr_j \eta_j$$

$$\sum vmr_{j,wet} = vmr_w + \sum_{not\ w} vmr_j$$

where $vmr_w = mnr_w/\rho_w$ and $vmr_j = mnr_j/\rho_j$. The summation terms on the RHS of both equations represent the dry aerosol contributions of each species.

4.3 Optical contributions of each aerosol species

4.3.1 Extinction coefficient profiles

If we seek to estimate the optical contribution of a single species, we cannot employ equation (9d) for each aerosol species (one value of j) since the very definition of internally mixed particles precludes a definition of n_j . A credible compromise is to assume that their (internally mixed equivalent) wet volume varies approximately as their dry volume fraction and that their optically equivalent contributions vary as their wet volume fraction. The first assumption translates to the expression;

$$vmr_{w,j} \sim \frac{vmr_j}{\sum vmr_j} vmr_w \quad (10a)$$

where $vmr_{w,j}$ represents an estimate of the water associated with each species. The radius (or size parameter) dependency of the optical efficiency (Q_j) varies relatively strongly in the fine mode (FM) region and very little in the coarse mode (CM) region¹⁴. In the case of FM particles¹⁵, it is better to integrate over the FM region to reduce the radius-bin to radius-bin dispersion between the optical and microphysical sides of equation (9b). We start by rewriting equation (10a) in terms of an analogous expression whose components have been integrated over the FM size range;

$$vmr_{f,w,j} \sim \frac{vmr_{f,j}}{\sum vmr_{f,j}} vmr_{f,w} \quad (10b)$$

The second assumption on the proportionality between the optical contribution and the wet volume fraction is explicitly expressed as;

¹⁴ where its value is ~ 2 (see Hansen & Travis, 1976 for example).

¹⁵ See the [footnote](#) concerning the applicability of the “int” equations to other types of aerosols (like FM aerosols)

$$\frac{d\tau_{f,j}}{dz} \sim \frac{d\tau_f}{dz} \gamma_{f,j} \quad (10c)$$

$$\text{where the fraction } \gamma_{f,j} = \frac{vmr_{f,j} + vmr_{f,w,j}}{\Sigma(vmr_{f,j} + vmr_{f,w,j})} = \frac{vmr_{f,j} + vmr_{f,w,j}}{\Sigma vmr_{f,j} + vmr_{f,w}} \quad (10d)$$

The change in the denominator comes from equation (10b) and, as required, $\gamma_{f,j}$ is conserved ($\Sigma \gamma_{f,j} = 1$ so that $\Sigma \frac{d\tau_{f,j}}{dz} = \frac{d\tau_f}{dz}$). A similar expression can be written for CM particles. Equation (10c) can be expressed in a more universal (TOMAS coherent) fashion by employing equation (9g);

$$d\tau_{f,j} \sim \left(\frac{d\tau_{f,j}}{dz} \frac{1}{\rho_{air}} \right) \frac{dP}{g} = \left(\frac{d\tau_f}{dz} \frac{1}{\rho_{air}} \right) \frac{dP}{g} \gamma_{f,j} \quad (10e)$$

4.3.2 Columnar optical depths

We have from equation (10e);

$$\tau_{f,j} \sim \int \left(\frac{d\tau_{f,j}}{dz} \frac{1}{\rho_{air}} \right) \gamma_{f,j} \frac{dP}{g} = \int \gamma_{f,j} d\tau_f \quad (10f)$$

which is coherent with equation (10c). Equations (10d) and (10f) represent explicit equations that would appear in the code. For purposes of better understanding what equation (10f) represents, it can be recast as the optically weighted mean of $\gamma_{f,j}$

$$= \tau_f \frac{\int \gamma_{f,j} d\tau_f}{\tau_f} \tau_f = \frac{\int \gamma_{f,j} d\tau_f}{\int d\tau_f} = \tau_f \langle \gamma_{f,j} \rangle \quad (10g)$$

To summarize, $\gamma_{f,j}$ comes from equation (10d) for each TOMAS layer, $d\tau_f$ comes from the “tau” variables¹⁶ of each TOMAS layer and τ_f is the readily available TOMAS FM AOD.

5. Effective radius

The effective radius is defined by Hansen & Travis (1974);

¹⁶ Such as “tau_sca_int = etc.” of the bystation_AOD_GCT.py code

$$r_{eff} = \frac{\int r^3 \frac{dN}{dr} dr}{\int r^2 \frac{dN}{dr} dr} \quad (11a)$$

$$= \frac{3}{4} \frac{\int \frac{4}{3} \pi r^3 \frac{dN}{dr} dr}{\int \pi r^2 \frac{dN}{dr} dr} = \frac{3}{4} \frac{\int \frac{dV}{dr} dr}{\int \frac{dS}{dr} dr} = \frac{3}{4} \frac{V}{S} \quad (11b)$$

where dV and dS are, respectively, the total differential particle volume / unit volume and the total differential particle projected area / unit volume in dr at a given altitude z . Equation (11b) assumes spherical particles¹⁷. An optically weighted altitude mean would logically be the altitude integral of the r_{eff} of equation (11) where the integral is weighted by the aerosol extinction coefficient;

$$\bar{r}_{eff} = \frac{\int r_{eff} k_{ext} dz}{\tau} = \frac{3}{4} \frac{\int \frac{V}{S} k_{ext} dz}{\tau}$$

However, in the spirit of the original Hansen & Travis definition (an optically free definition of effective radius) and coherent with how the AERONET effective radii are calculated (from retrieved values of volume abundance PSD $\frac{dA_v}{d \log r}$ and the projected-surface abundance PSD $\frac{dA_s}{d \log r}$), the purely mechanical, altitude-weighted effective radius would, more appropriately, be defined as;

$$\bar{r}_{eff} = \frac{3}{4} \frac{\int V dz}{\int S dz} = \frac{3}{4} \frac{A_v}{A_s} \quad (12)$$

where the total volume and projected-area abundances are (with j representing a given aerosol species);

$$A_v = \int \frac{dA_v}{dr} dr = \int \frac{\sum dA_{m,j}/\rho_j}{dr} dr \quad (13b)$$

$$A_s = \int \frac{dA_s}{dr} dr = \frac{3}{4} \int \frac{1}{r} \frac{\sum dA_{m,j}/\rho_j}{dr} dr \quad (13c)$$

¹⁷ or casts equation (11a) in terms of effective spherical particles in the case of non spherical particles

where the units of A_v and A_s are respectively $\text{m}^3\text{-m}^{-2}$ and $\text{m}^2\text{-m}^{-2}$. One can then express the analogous trio of TOMAS-like bin expressions as;

$$A_v = \sum_i \sum_j \Delta A_{m,j,i} / \rho_j \quad (14a)$$

$$A_s = \frac{3}{4} \sum_i \frac{1}{r_i} \sum_j \Delta A_{m,j,i} / \rho_j \quad (14b)$$

where $\Delta A_{m,j,i}$ is the mass abundance of the j th aerosol component in the i th (log) radius bin.

6. A note on bulk versus TOMAS (PSD or sectional) models

Kodros & Pierce (2017) gave a very good example on the advantage of a TOMAS PSD model versus a GEOS-Chem type bulk. They noted that : “ ... *although both the prescribed and prognostic methods compare similarly well with present-day size-distribution observations, there are substantial differences in the relative CDNC and CAE [Cloud Albedo Effect] due to anthropogenic emissions. When using the prognostic size-distribution method, anthropogenic emissions yield a 25–75% larger increase in CDNC over most land masses but a 50–75% smaller increase in some remote-marine regions than in the prescribed size-distribution methods*¹⁸.” In fact they used the TOMAS model to simulate the bulk model¹⁹ (which makes sense as opposed to a more “PSD-divorced” approach which would maintain prescribed lognormal PSDs).

¹⁸ CDNC = Cloud Droplet Number Concentration. Stated otherwise, they found that different parts of the PSD had different degrees of influence on cloud droplet formation

¹⁹ “*The second size-distribution method used in this study is a prescribed mapping of bulk species mass to lognormal distributions (referred to as “LOGNORMAL,” see Table 1). The purpose of the LOGNORMAL method is to represent the method of estimating aerosol number concentrations used in several mass-only (i.e., bulk aerosol schemes. Here the total particle mass for each species is converted to a size distribution off-line assuming lognormal distributions with one mode (sulfate, OA, and BC), two modes (sea salt), or three modes (dust).*”

Appendix B: GCT AOD Code

Both MATLAB and Python were employed in this work (in addition to a Fortran subroutine). Because of the large datasets of the model simulations, we used Compute Canada's/Calcul Quebec's clusters.

In this section, we display the main code utilized for the AOD calculations from TOMAS. The Mie code used was Bohren and Hoffmen (a Fortran subroutine).

Original authors and general support:

Jeffrey R. Pierce, Associate Professor, Colorado State University, Boulder, Colorado, USA

Jack Kodros, Postdoc, Colorado State University, Boulder, Colorado, USA

Adjustments and Editing: *Yasmin AboEl-Fetouh and Huizhong Lu with Jack Kodros*

Technical help & Optimized code for parallel computing:

Huizhong Lu, , Calcul Quebec/Compute Canada, Université de Sherbrooke, Sherbrooke, Quebec, Canada

General supervision and revision: *Norm O'Neill*

The following are the software versions used to run the code:

Python version: 3.7.0

Scipy-stack version: 2019a

module load intel/2018.3

netcdf version: 4.6.1

```
# GCTAOD calculation for conversations with Norm and Yasmin
# Written by J. Kodros 3/28 and J. Pierce. Based on the DRE code we use for RF calculations

# adjusted by Y. Aboel-Fetouh, adapted for parallel and sequential computing by H. Lu (run on
Mammoth - Calcul Quebec/Compute Canada clusters)
# debugged by H.Lu and Y.Aboelfetouh with J.Kodros
# Version finalized on 24th December, 2019

# added lines to specify the latitude and longitude (to get tau for the individual stations)
# 20 Feb,2019: adjusted filtering for zero (and small) values of nK and BC (Jack and Yasmin)

# Import modules
import numpy as np
import numpy.ma as ma
from netCDF4 import Dataset, num2date, date2num
from bhmie import bhmie
import sys
import pandas as pd
import scipy
import pdb
```

```

##### -----#####
##### Define some sub-routines
##### -----#####
# Below are functions that return the average middle pressure and edge pressure in GEOS-Chem
# a list of these can be found on the GEOS-Chem User's Guide

# Average pressure in the middle of vertical box
def get_presm():
    etam = np.array([0.000028, 0.000127, 0.000400, 0.001113, 0.002825, 0.006609, \
        0.014389, 0.023832, 0.033923, 0.047794, 0.066773, 0.084584, \
        0.099510, 0.117070, 0.137729, 0.162033, 0.190668, 0.224471, \
        0.264374, 0.310730, 0.354300, 0.391937, 0.429595, 0.467274, \
        0.504968, 0.542673, 0.580389, 0.618113, 0.655841, 0.687287, \
        0.712447, 0.737606, 0.762768, 0.787933, 0.810582, 0.828198, \
        0.843298, 0.858399, 0.873500, 0.888601, 0.903703, 0.918805, \
        0.933908, 0.949010, 0.964113, 0.979217, 0.994283]) # box middle

    ptop = 0.01 # mb
    psurf = 1000 # mb
    nlevs = 47
    presm = []
    for ll in range(0, nlevs):
        l = nlevs - ll - 1
        presm.append(ptop + etam[l] * (psurf - ptop))
    presm = np.array(presm)
    return presm

# Average pressure at edges
def get_prese():
    etae = np.array([0.000000, 0.000055, 0.000199, 0.000601, 0.001625, 0.004026, \
        0.009191, 0.019586, 0.028077, 0.039768, 0.055820, 0.077726, \
        0.091442, 0.107578, 0.126563, 0.148896, 0.175170, 0.206167, \
        0.242774, 0.285974, 0.335486, 0.373114, 0.410759, 0.448431, \
        0.486118, 0.523819, 0.561527, 0.599251, 0.636974, 0.674708, \
        0.699867, 0.725026, 0.750186, 0.775350, 0.800515, 0.820648, \
        0.835748, 0.850848, 0.865949, 0.881051, 0.896152, 0.911253, \
        0.926356, 0.941459, 0.956562, 0.971665, 0.986769, 1.001796]) # box edge sigma
coordinates

    ptop = 0.01 # mb
    psurf = 1000 # mb
    nlevs = 47
    prese = []
    for ll in range(0, nlevs + 1):
        l = (nlevs + 1) - ll - 1
        prese.append(ptop + etae[l] * (psurf - ptop))
    prese = np.array(prese)
    return prese

def cal_TAU_avg( data_shape, aeroNum, SO4, SS, OAIL, OAOB, BCIL, BCOB, DUST, AW, pressure,
prese, file_name_index ):
    """ all arrays (except prese) are sub-section of corresponding global array with specific value of
longi/lati """
    critic const = 1E-10

```

```

TAU = np.zeros( data_shape )

print(' data_shape[2:-1:-1] = ', data_shape[2:-1:-1])
nb_large_reff_ext = 0
for l in range(data_shape[2]):
    for b in range(data_shape[1]):
        for ti in range(data_shape[0]):

            nk = aeroNum[ti,b,l]

            mso4 = SO4[ti, b, l]
            mnh4 = mso4 * 0.1875
            mnacl = SS[ti, b, l]
            moc = OAIL[ti, b, l] + OAOB[ti, b, l]
            mecil = BCIL[ti, b, l]
            mecob = BCOB[ti, b, l]
            mdust = DUST[ti, b, l]
            mh2o = AW[ti, b, l]

            mtot = mso4 + mnh4 + mnacl + moc + mecil + mecob + mdust + mh2o

            if( nk ==0 or mtot==0 ):
                continue
            if ( nk < critic_const and mtot<critic_const ):
                continue

            mp = mtot / nk

            # Calculate volume assuming spherical particles
            vol_so4 = (mso4 + mnh4) / rho_so4 # [m3]
            vol_h2o = mh2o / rho_h2o
            vol_oc = moc / rho_oc
            vol_dust = mdust / rho_dust
            vol_nacl = mnacl / rho_nacl

            if (mecil ==0 and mecob ==0):
                num_ext=0
                vol_ext=0
            else:
                num_ext = (mecil+mecob)/mp # same as mecil/mp + mecob/mp
                if (mecil !=0 ):
                    vol_ecil = mecil / rho_bc
                else:
                    vol_ecil=0

                if (mecob != 0):
                    vol_ecob = mecob / rho_bc
                else:
                    vol_ecob=0

            # Volume of external (BC) mixture
            vol_ext = vol_ecob + vol_ecil # "ecob" is hydrophobic BC "ecil" is hydrophilic BC

```

```

num_int = nk - num_ext

# Calculate the refractive index. This depends on the mixing-state assumption
# We usually assume the scattering particles are mixed (and the RF a volume-weighted avg)
# Black carbon can be a separate particle, a core with a scattering shell around it
# or mixed homogeneously like the other scattering particles
# Here let's assume an external mixture for simplicity.

# Volume of internal (scattering species) mixture
vol_int = vol_so4 + vol_oc + vol_dust + vol_nacl

#
if( vol_int > 0):
    # Real refractive index (scattering population)
    refre = (vol_so4 * n_so4 + vol_h2o * n_h2o + vol_nacl * n_nacl + vol_oc * n_oc \
            + vol_dust * n_dust) / (vol_int + vol_h2o)
    # Imaginary refractive index (scattering population)
    refim = (vol_so4 * k_so4 + vol_h2o * k_h2o + vol_nacl * k_nacl + vol_oc * k_oc \
            + vol_dust * k_dust) / (vol_int + vol_h2o)
    rfint = refre + refim * 1j
    rfext = complex(n_bc, k_bc) # this popuation is just BC
else:
    rfint=0.
    rfext = complex(n_bc, k_bc) # this popuation is just BC

# For the internal population
if( num_int > 0. ):
    vol_intp = (vol_so4 + vol_h2o + vol_oc + vol_dust + vol_nacl) / num_int
    reff_int = (3. / 4. * vol_intp / np.pi) ** (1. / 3.)
    # Calculate the size parameter for the populations
    sizep_int = 2 * np.pi * reff_int / (wl * 1e-9)
    if( sizep_int > 1.e7 ):
        print(' vol_so4=',vol_so4,', vol_h2o=',vol_h2o,', vol_oc=',vol_oc)
        print(' vol_dust=',vol_dust,', vol_nacl = ',vol_nacl,',num_int=',num_int)
        print(' vol_intp = ',vol_intp)
        print(' reff_int = ',reff_int,', wl=',wl)
    else:
        sizep_int = 0
if( sizep_int > 2.e7 ):
    print(' sizep_int = too large , sizep_int=',sizep_int)
    quit()

# The remaining particles are in the scattering mixture

# Calculate the radii of the two populations
# For the external (BC) popuation
sizep_ext = 0
if( num_ext > critic_const ):
    vol_extp = (vol_ecil + vol_ecob) / num_ext
    reff_ext = (3. / 4. * vol_extp / np.pi) ** (1. / 3.)
    if( reff_ext < 1.e-2 ):
        sizep_ext = 2 * np.pi * reff_ext / (wl * 1e-9)

```

```

else:
    nb_large_reff_ext += 1

##
# Bohren&Hoffman Mie code is used here
# The output of Mie code is the extinction and scattering ratios
# qext -- extinction ratio
# qsca -- scattering ratio
# gsca -- asymmetry parameter

if ( sizep_int>0 and abs(rfint)>0 ):
    Qint = bhmie(sizep_int, rfint, 2)
    qext_int = Qint[0]
    qsca_int = Qint[1]
    gsca_int = Qint[3]
    qabs_int = qext_int - qsca_int

    babs_int = reff_int ** 2 * np.pi * num_int * qabs_int
    bsca_int = reff_int ** 2 * np.pi * num_int * qsca_int

    tau_abs_int = babs_int * pressure[ti, l] / grav * 100. * np.log(prese[l] / prese[l + 1]) #
replaced presm with pressure
    tau_sca_int = bsca_int * pressure[ti, l] / grav * 100. * np.log(prese[l] / prese[l + 1]) #
replaced presm with pressure
    tau_int = tau_abs_int + tau_sca_int
    press_ct = pressure[ti, l] / grav * 100. * np.log(prese[l] / prese[l + 1])
    ssa_int = tau_sca_int / (tau_int)

if tau_int < 0.0:
    print ('NEGATIVE TAU INT')
    sys.exit()

if (np.isnan(tau_int)):
    print('Error with NAN: tau_int=', tau_int)
    quit()

TAU[ti, b, l] += tau_int

if ( sizep_ext>0 and abs(rfext)>0 ):
    Qext = bhmie(sizep_ext, rfext, 2)
    qext_ext = Qext[0]
    qsca_ext = Qext[1]
    gsca_ext = Qext[3]
    qabs_ext = qext_ext - qsca_ext

    # abs/scat coefficients [m-1]
    babs_ext = reff_ext ** 2 * np.pi * num_ext * qabs_ext
    bsca_ext = reff_ext ** 2 * np.pi * num_ext * qsca_ext

    # abs/scat optical depth
    tau_abs_ext = babs_ext * pressure[ti, l] / grav * 100. * np.log(
        prese[l] / prese[l + 1]) # replaced presm[l] with pressure[ti,l]
    tau_sca_ext = bsca_ext * pressure[ti, l] / grav * 100. * np.log(
        prese[l] / prese[l + 1]) # replaced presm with pressure
    tau_ext = tau_abs_ext + tau_sca_ext

```

```

        if( np.isnan(tau_ext) ):
            print('Error NANA, ssa_ext = ', ssa_ext)
            quit()
        TAU[ti, b, l] += tau_ext

errors = np.where(TAU < 0)
print('errors aod less than zero = ', errors)

#TAU_no_lev = TAU.sum(axis=2)
tau_avgmnth = TAU.mean(axis=0)
#print(TAU_no_lev)

return TAU

##### -----#####
##### READ IN MODEL OUTPUT
##### -----#####
# Define file name and path
# (you may want to change this into a list and loop over the files
# file_directory = 'C:/Users/.../Desktop/GCT/'
filename = 'GC_TOMAS_Output_20150101.nc'

# Open netCDF file
nc_fid = Dataset(filename)#file_directory +
lat = nc_fid.variables['latitude'][:]
lon = nc_fid.variables['longitude'][:]
t = nc_fid.variables['time'][:]

# # Enter station details
la = abs(lat - 80.054).argmin()
lo = abs(lon - -86.417).argmin()
# stn = 'pearl'

# Units are in nc meta-data
# aeroNum in num kg-1 air
# mass is in kg kg-1 air

# initial-C_CONTIGUOUS: [time, bin, level, lat, lon], ==np.asfortranarray=> Fortran order
aeroNum = np.asfortranarray( nc_fid.variables['aeroNum'][:, :, :, :] )
SO4= np.asfortranarray( nc_fid.variables['SO4' ][:, :, :, :] )
SS= np.asfortranarray( nc_fid.variables['SS' ][:, :, :, :] )
BCIL= np.asfortranarray( nc_fid.variables['BCIL' ][:, :, :, :] )
BCOB= np.asfortranarray( nc_fid.variables['BCOB' ][:, :, :, :] )
OAIL= np.asfortranarray( nc_fid.variables['OAIL' ][:, :, :, :] )
OAOB= np.asfortranarray( nc_fid.variables['OAOB' ][:, :, :, :] )
DUST = np.asfortranarray( nc_fid.variables['DUST' ][:, :, :, :] )
AW = np.asfortranarray( nc_fid.variables['AW' ][:, :, :, :] )

##### HZ: get size by nc file
data_shape = SO4.shape
# Define number of vertical levels
ltop = data_shape[2] # 30
# Define number of size bins
nbins = data_shape[1] # 40

```

```

if( data_shape[0] != len(t) or \
    data_shape[1] != nbins or \
    data_shape[2] != ltop or \
    data_shape[3] != len(lat) or \
    data_shape[4] != len(lon) ):
    print( ' data_shape from nc file is not coherent ! ' )
    quit()

temperature = np.asfortranarray( nc_fid.variables['temperature'][:, :, :, :] ) # [time, level, lat, lon]
pressure     = np.asfortranarray( nc_fid.variables['pressure' ][:, :, :, :] )

time = num2date(t, units='days since 0001-01-01 00:00:00.0', calendar='gregorian')
Dp   = nc_fid.variables['Dp'][:] # this is an average bin diameter (assuming some density)
Dpk  = nc_fid.variables['Dpk'][:]
nc_fid.close()

##### -----#####
##### READ IN non-GCTpieces of interest
##### -----#####
### Set radiative parameters
# Here we will define a wavelength (or usually multiple wavelengths) of interest
# Also want the real and imaginary index of refraction.

w1 = 550.

# Assign refractive indices

n_so4 = 1.43
n_nacl = 1.50
n_bc  = 1.95 #updated by Jack in Dec 2019 according to email 16 Dec, 2019 (Steir et al. 2007)
n_oc  = 1.53
n_dust = 1.53
n_h2o = 1.33

k_so4 = 1.00E-8
k_nacl = 1.00E-8 #3.6E-8
k_bc  = 0.79 #updated by Jack in Dec 2019 according to email 16 Dec, 2019 (Steir et al. 2007)
k_oc  = 6.00E-3 #5.74E-3
k_dust = 5.50E-3 #6.21E-3
k_h2o = 1.96E-9

# Assume particle densities
rho_so4 = 1.78e3 # I.N. Tang (1996) [kg/m3] (Ammonium bisulfate = 1780kg/m3)
rho_h2o = 1.e3
rho_oc  = 1.4e3 # Dick et al. (2000) - consistent with water uptake reference
rho_bc  = 1.8e3 # Bond and Bergstrom (2006)
rho_dust = 2.65e3 # Tegen and Fung (1994)
rho_nacl = 2.165e3 # I.N. Tang (1996)

# Get average pressures
presm = get_presm() # hPa
prese = get_prese()

```

```

# Gravity
grav = 9.8 # kg m-2 s-1

##### -----#####
#### Start main calculation
##### -----#####
TAU = np.zeros( data_shape )
TAU_INT_JKK = np.zeros( data_shape )
TAU_EXT_JKK = np.zeros( data_shape )

listTAU = []
spatial_values=np.zeros((8,72))

TAU_avg_objs = [ [None for lati in range (data_shape[3])] for longi in range (data_shape[4]) ]
TAU_avg = np.zeros( data_shape[3:] )
TAU_test=np.zeros(data_shape[0:1])
t_all = np.zeros(data_shape [0:3])

#PARALLEL
import multiprocessing as mp
pool = mp.Pool(mp.cpu_count())
#HZ#for longi in range(data_shape[4]):
#HZ#  for lati in range (data_shape[3]):
for longi in [lo]:
    for lati in [la]:
        #print(' lati = ',lati,', longi = ',longi)
        TAU_avg_objs[longi][lati] = pool.apply_async( cal_TAU_avg, \
            ( data_shape[:3], aeroNum[:, :, :, lati, longi], \
              SO4[:, :, :, lati, longi], SS[:, :, :, lati, longi], \
              OAIL[:, :, :, lati, longi], OAOB[:, :, :, lati, longi], \
              BCIL[:, :, :, lati, longi], BCOB[:, :, :, lati, longi], \
              DUST[:, :, :, lati, longi], AW[:, :, :, lati, longi], pressure[:, :, :, lati, longi], prese, \
              'LO'+str(longi)+'_LA'+str(lati) ) )
pool.close()
pool.join()

##printing output of the TAU[time,bin,level]
tt= num2date(t, units='days since 0001-01-01 00:00:00.0', calendar='gregorian')
writer = pd.ExcelWriter('resbay_12_3dtau.xlsx', engine='xlsxwriter')
Time = pd.DataFrame(tt)
for i in range(0, 40):
    aod = pd.DataFrame(t_all[:, i, :])
    Time.to_excel(writer, index=False, header=['DateTime'], sheet_name='bin%d' % i)
    aod.to_excel(writer, index=False, header=[1, 2, 3, 4, 5, 6, 7, 8, 9, 10, 11, 12, 13, 14, 15, 16, 17, 18, 19,
20, 21, 22, 23, 24, 25, 26,27, 28, 29, 30], sheet_name='bin%d' % i, startcol=1)

writer.save()

print('done')

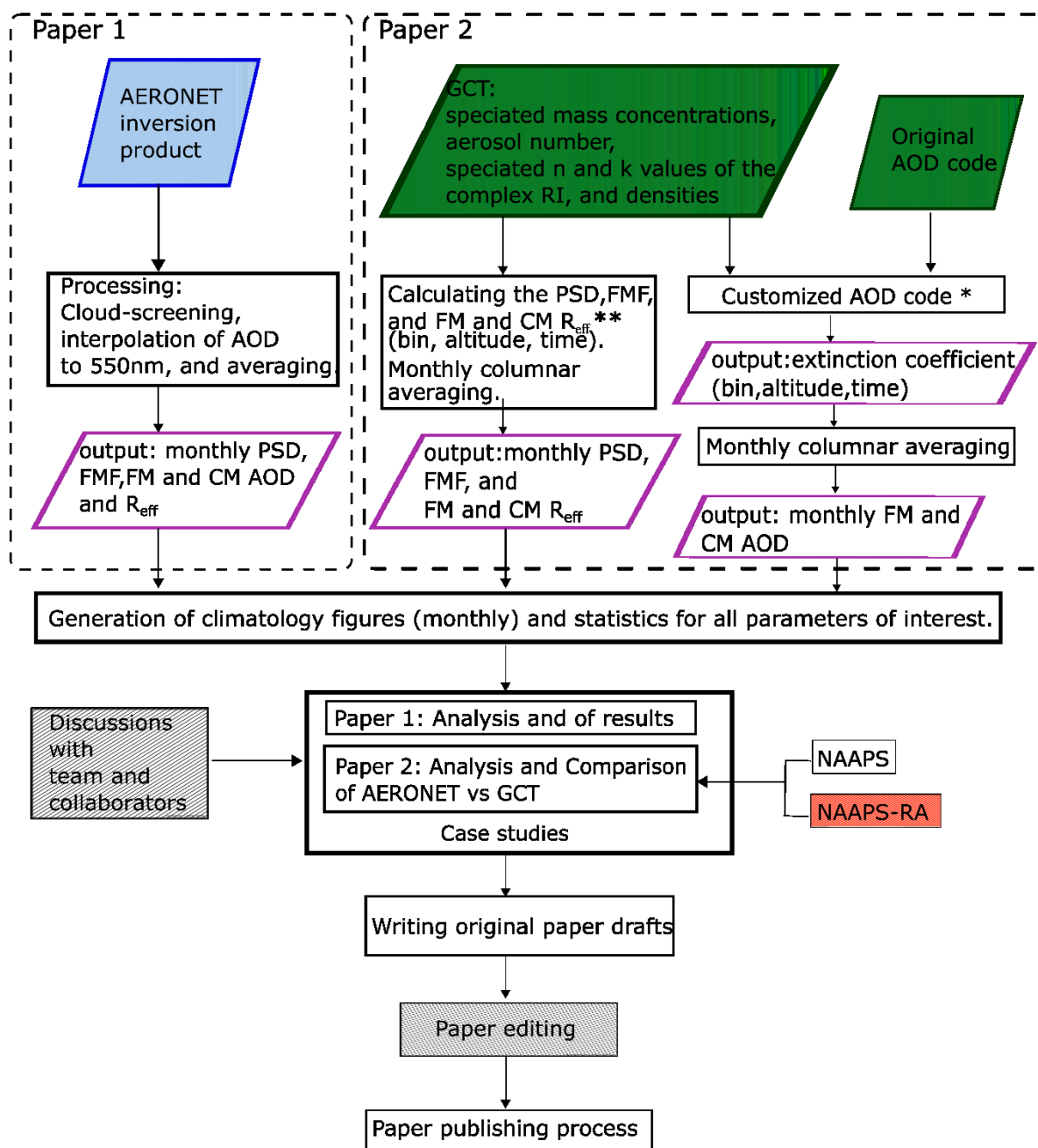
```


Appendix C: Flowchart of thesis project

The flow chart below was added to better contextualize the scientific strategy of the thesis and to indicate my contributions (white coloured flow chart elements) in relation to those of the co-authors of Papers 1 and 2 as well as the thesis in general (other colours).

Legend

- Y.AboElFetouh contribution
- Provided by Colorado State University team
- From AERONET website
- Mainly with Norm O'Neill and includes input from all co-authors
- Provided by Peng Xian



* Refer to Appendix B for details.

** Made use of Norm O'Neill's technical memo. Refer to Appendix A for details

References

The references listed below are those sited in the Introduction section and the Appendices only.

- Abbatt, J. P. D., Richard Leaitch, W., Aliabadi, A. A., Bertram, A. K., Blanchet, J. P., Boivin-Rioux, A., et al. (2019). Overview paper: New insights into aerosol and climate in the Arctic. *Atmospheric Chemistry and Physics*, 19(4), 2527–2560. <https://doi.org/10.5194/acp-19-2527-2019>
- Adams, P. J., & Seinfeld, J. H. (2002). Predicting global aerosol size distributions in general circulation models. *Journal of Geophysical Research Atmospheres*, 107(19), 1–23. <https://doi.org/10.1029/2001JD001010>
- AMAP. (2021). Arctic Climate Change Update 2021: Key Trends and Impacts. Summary for Policy-makers. *Arctic Monitoring and Assessment Programme (AMAP)*. Tromsø, Norway: Arctic Monitoring and Assessment Programme (AMAP).
- Bey, I., Jacob, D. J., Yantosca, R. M., Logan, J. A., Field, B. D., Fiore, A. M., et al. (2001). Global modeling of tropospheric chemistry with assimilated meteorology: Model description and evaluation. *Journal of Geophysical Research Atmospheres*, 106(D19), 23073–23095. <https://doi.org/10.1029/2001JD000807>
- Bond, T. C., & Bergstrom, R. W. (2006). Aerosol Science and Technology Light Absorption by Carbonaceous Particles: An Investigative Review. *Aerosol Science and Technology*, 40(1), 27–67. <https://doi.org/10.1080/02786820500421521>
- Boucher, O., Randall, D., Artaxo, P., Bretherton, C., Feingold, G., Forster, P., et al. (2013). *Clouds and Aerosols*. In: *Climate Change 2013: The Physical Science Basis. Contribution of Working Group I to the Fifth Assessment Report of the Intergovernmental Panel on Climate Change [Stocker, T.F., D. Qin, G.-K. Plattner, M. Tignor, S.K. Allen, J. Bos. Cambridge University Press, Cambridge, United Kingdom and New York, NY, USA. Retrieved from https://www.ipcc.ch/pdf/assessment-report/ar5/wg1/WG1AR5_Chapter07_FINAL.pdf*
- Boucher, Olivier. (2015). *Atmospheric Aerosols: Properties and Climate Impacts*. Springer Netherlands. <https://doi.org/10.1007/978-94-017-9649-1>
- Breider, T. J., Mickley, L. J., Jacob, D. J., Wang, Q., Fisher, J. a., Chang, R. Y.-W., & Alexander, B. (2014). Annual distributions and sources of Arctic aerosol components, aerosol optical depth, and aerosol absorption. *Journal of Geophysical Research: Atmospheres*, 119(7), 4107–4124. <https://doi.org/10.1002/2013JD020996>
- Bullard, J. E., Matthew, B., Tom, B., John, C., Eleanor, D., Diego, G., et al. (2016). High latitude dust in the Earth system. *Reviews of Geophysics*, 54, 447–485. <https://doi.org/10.1002/2016RG000518>.Received
- Chin, M., Diehl, T., Tan, Q., Prospero, J. M., Kahn, R. A., Remer, L. A., et al. (2019). Multi-decadal aerosol variations from 1980 to 2009 : a perspective from observations and a global model, 3657–3690. <https://doi.org/10.5194/acp-14-3657-2014>
- Dick, W. D., Saxena, P., & McMurry, P. H. (2000). Estimation of water uptake by organic compounds in submicron aerosols measured during the Southeastern Aerosol and Visibility Study. *Journal of Geophysical Research*, 105(D1), 1471–1479. <https://doi.org/10.1029/1999JD901001>
- Eck, T. F., Holben, B. N., Reid, J. S., Sinyuk, a., Hyer, E. J., O'Neill, N. T., et al. (2009). Optical properties of boreal region biomass burning aerosols in central Alaska and seasonal variation of aerosol optical depth at an Arctic coastal site. *Journal of Geophysical Research: Atmospheres*, 114(11), 1–

14. <https://doi.org/10.1029/2008JD010870>

Groot Zwaaftink, C. D., Grythe, H., Skov, H., & Stohl, A. (2016). Substantial contribution of northern high-latitude sources to mineral dust in the Arctic. *Journal of Geophysical Research*, *121*(22), 13,678–13,697. <https://doi.org/10.1002/2016JD025482>

Hansen, J. E. & Travis, L. D. (1974). Light scattering in planetary atmospheres, *Space Sci. Rev*, *16*(4), 527–610.

Hinds, W. C. (1999). *Aerosol Technology: Properties, Behavior, and Measurement of Airborne Particles* (2nd Editio). John Wiley & Sons, Inc.

Huang, J., & Jaeglé, L. (2017). Wintertime enhancements of sea salt aerosol in polar regions consistent with a sea ice source from blowing snow. *Atmospheric Chemistry and Physics*, *17*(5), 3699–3712. <https://doi.org/10.5194/acp-17-3699-2017>

IPCC. (2021). Summary for Policymakers. In: *Climate Change 2021: The Physical Science Basis. Contribution of Working Group I to the Sixth Assessment Report of the Intergovernmental Panel on Climate Change*. In V. Masson-Delmotte, P. Zhai, A. Pirani, S. L. Connors, C. Pean, S. Berger, et al. (Eds.). Cambridge University Press. In Press. <https://doi.org/10.1080/03736245.2010.480842>

Kodros, J.K. & Pierce, J.R. (2017). Important global and regional differences in aerosol cloud-albedo effect estimates between simulations with and without prognostic aerosol microphysics. *JGR: Atmospheres*; *122*(7):4003–18.

Law, K. S., & Stohl, a. (2007). Arctic Air Pollution: Origins and Impacts. *Science*, *315*(5818), 1537–1540. <https://doi.org/10.1126/science.1137695>

O'Neill, N. T., Eck, T. F., Holben, B. N., Smirnov, A., & Dubovik, O. (2001). Bimodal size distribution influences on the variation of Angstrom derivatives in spectral and optical depth space. *Journal of Geophysical Research*, *106*(D9), 9787–9806. <https://doi.org/10.1029/2000JD900245>

O'Neill, N. T., S. Thulasiraman, T. F. Eck, J. S. Reid (2008a). Correction to the effective radius expression in O'Neill et al. (2005), *Journal of Geophysical Research*, *113*, D24203, <https://doi.org/10.1029/2008JD011334>

O'Neill, N. T., T.F. Eck, Reid, J. S, Smirnov, A., O. Pancrati (2008b). Coarse mode optical information retrievable using ultraviolet to shortwave infrared sunphotometry; application to UAE2, *Journal of Geophysical Research*, *113*, D05212, <https://doi.org/10.1029/2007JD009052>

Power, H. C. (2003). The geography and climatology of aerosols. *Progress in Physical Geography*, *27*(4), 502–547. <https://doi.org/10.1191/0309133303pp393ra>

Ramnarine, E., Kodros, J. K., Hodshire, A. L., Lonsdale, C. R., Alvarado, M. J., & Pierce, J. R. (2019). Effects of near-source coagulation of biomass burning aerosols on global predictions of aerosol size distributions and implications for aerosol radiative effects. *Atmospheric Chemistry and Physics*, *19*(9), 6561–6577. <https://doi.org/10.5194/acp-19-6561-2019>

Schmale, J., Zieger, P., & Ekman, A. M. L. (2021). Aerosols in current and future Arctic climate. *Nature Climate Change*, *11*(February). <https://doi.org/10.1038/s41558-020-00969-5>

Seinfeld, J. H., & Pandis, S. N. (2006). *Atmospheric Chemistry and Physics: From Air Pollution to Climate Change* (2nd edition). John Wiley & Sons, Inc.

Slater, T., Hogg, A. E., & Mottram, R. (2020). Ice-sheet losses track high-end sea-level rise projections. *Nature Climate Change*, *10*(10), 879–881. <https://doi.org/10.1038/s41558-020-0893-y>

Stier, P., Seinfeld, J. H., Kinne, S., and Boucher, O.: Aerosol absorption and radiative forcing, *Atmospheric Chemistry and Physics*, *7*, 5237–5261, <https://doi.org/10.5194/acp-7-5237-2007>,

2007

- Tang, Ignatius N. (1996). Chemical and size effects of hygroscopic aerosols on light scattering coefficients. *Journal of Geophysical Research: Atmospheres*, 101.D14, 19245-19250. <https://doi.org/10.1029/96JD03003>
- Tegen, I., & Fung, I. (1994). Modeling of mineral dust in the atmosphere: Sources, transport, and optical thickness. *Journal of Geophysical Research*, 99(D11), 22,897-22,914. <https://doi.org/10.1029/94JD0192>
- Tsonis, A. (2002). *An introduction to atmospheric thermodynamics*, Cambridge University Press, Cambridge, UK.
- Udisti, R., Traversi, R., Becagli, S., Tomasi, C., Mazzola, M., Lupi, A., & Quinn, P. K. (2020). Arctic Aerosols. In A. Kokhanovsky & C. Tomasi (Eds.), *Physics and Chemistry of the Arctic Atmosphere*, pp. 209–329). Springer Polar Sciences. Springer, Cham. https://doi.org/10.1007/978-3-030-33566-3_4